Gas Chromatographic Microsystems: Design and Implementation of Improved Devices for Sample Capture and Detection

by

Changhua Zhan

A dissertation submitted in partial fulfillment
of the requirements for the degree of
Doctor of Philosophy
(Environmental Health Sciences)
in The University of Michigan
2020

Doctoral Committee:

Professor Edward T. Zellers, Chair
Assistant Professor Andrew Ault
Professor Xudong Fan
Research Assistant Professor Joe Potkay

Changhua Zhan

henryzch@umich.edu

ORCID iD: 0000-0001-8735-8977

DEDICATION

To my parents, wife, grandmother, teachers, and friends.

ACKNOWLEDGMENTS

I would first like to thank my advisor, Professor Edward T. Zellers, for his five years of support, patient guidance and mentorship. Without his insightful advice, countless emails and numerous discussions, this dissertation would not have been possible. I would also like to thank my dissertation committee members, Dr. Andrew Ault, Dr. Xudong Fan, and Dr. Joe Potkay for their commentaries and insights through my graduate training.

I would like to acknowledge current and former members of the Zellers Group and other collaborators who made vital contributions to this research: Kee Scholten for µOFRR training, Zhijin Lin for MPN film screening testing, Muhammad Akbar for insight in µPP testing, Nicolas Nuñovero for electronic software and hardware, Lexuan Zhong for early help with GC calibrations, Fernando Almazán Román for early TGA testing, Junqi Wang for training and problem solving; Jon Bryant-Genevier for training on PCF operation; Sanketh Buggaveeti, Rob Nidetz, and Katsuo Kurabayashi for designing the µPCF heater and fabricating µPCF device; Chengyi Zhang and Will Collin for GC training; Brendan Casey for wire-bonding; Robert Hower and Tom Daunais for µPP fabrication; and Bjoern Brixius for performing some GC calibrations.

I would like to sincerely thank my family who have for your love, encouragement and support while I implemented this dissertation. I would like to give special thanks to my wife, Ruochen Xu, who always listened to me and helped share happiness and burden over the past

several years. Thank you Hongbo Zhu for your friendship and intellectually stimulating discussions.

Finally, I would like to thank the funding sources that supported this work: Contract # 2017-17012600004 from the Office of the Director of National Intelligence (ODNI), Intelligence Advanced Research Projects Activity (IARPA), Grant # T42 OH008455 from the Centers for Disease Control and Prevention (CDCP), and University of Michigan Office of Research Grant #25248 (UM OVPR, EHS, UM/SJTU Collaboration).

TABLE OF CONTENTS

DEDICATION ii
ACKNOWLEDGMENTS iii
LIST OF FIGURES ix
LIST OF TABLES xiii
ABSTRACT xiv
Chapter 1 1
Introduction, Background, and Significance 1
1.1 Dissertation Overview 1
1.2 Volatile and Semi-Volatile Organic Compounds 2
1.2.1 Health Effects of VOCs 3
1.3 Traditional Methods of VOC Sampling and Analysis 4
1.4 Adsorption Theory 8
1.5 Portable Analytical Instruments for VOCs 10
1.6 Microfabricated GC 13
1.6.1 Microfabricated Preconcentrators 15
1.6.1.1 Active Preconcentrators and Microfabricated Preconcentrators 15
1.6.1.2 Theory of Passive Sampling 19
1.6.1.3 Passive Sampling Devices 21
1.6.1.4 Passive Microfabricated Preconcentrators 23
1.6.2 Microfabricated Columns 25
1.6.3 Microfabricated Sensors 29
1.6.3.1 Microsensors for VOC Detection 29
1.6.3.2 Single Transducer (ST) Arrays 32
1.6.3.3 Multi-Transducer (MT) and Multi-Variable (MV) Arrays 33

1.6.3.4 LSPR 34
1.6.3.5 Chemometrics 35
1.6.3.6 Microfabricated Optofluidic Ring Resonator (μOFRR) 36
1.7 Significance of This Research 38
1.8 References 40
Chapter 2 55
A Nanomaterial-coated Micro-optofluidic Ring Resonator for Vapor Detection 55
2.1 Introduction 55
2.2 Experimental Methods 60
2.2.1 Materials 60
2.2.2 Testing 60
2.3 Results and Discussion 67
2.3.1 Film Morphology/Uniformity 67
2.3.2 Screening of Response Diversity 69
2.3.3 PDMS-Coated μOFRR 74
2.3.4 TEG-MPN coated μOFRR 75
2.3.5 CTAB-NR tests 76
2.4 Conclusions 77
2.5 References 78
Chapter 3 81
Microfabricated Passive Preconcentrator for μGC 81
3.1 Introduction 81
3.2 Background 84
3.3 Experimental 87
3.3.1 Materials 87
3.3.2 μPP description and fabrication summary 88
3.3.3 μPCF 89
3.3.4 Device filling, sealing, mounting 90
3.3.5 Test system and exposure chamber 91

3.3.6 Testing procedures 92
3.3.7 Thermogravimetric analysis (TGA) 94
3.3.8 Heater control, parameter adjustment, data acquisition, data analysis 94
3.4 Results and Discussion 95
3.4.1 Design and operation 95
3.4.2 TGA Mass Uptake, Offgassing, and Desorption Efficiency 100
3.4.3 µPP desorption/transfer conditions 102
3.4.4 Sampling rate stability: concentration 103
3.4.5 Sampling rate stability: duration 104
3.4.6 Modeling of S_e 106
3.4.7 Sampling rates for other compounds 109
3.4.8 Mixtures 111
3.5 Conclusions and Outlook 113
3.6 References 117
Chapter 4 121
Conclusions and Future Work 121
4.1 Summary 121
4.2 A Nanomaterial-Coated Micro-Optofluidic Ring Resonator for Vapor Detection 121
4.3 Microfabricated Passive Preconcentrator for µGC 123
Appendix 127
Supporting Information for Chapter 3 127
A1. µPP fabrication 127
A2. Test system and exposure chamber 130
A3. TGA set-up and procedure 132
A4. Temperature profiles 133
A5. TGA data and W_e values 134
A6. Desorption (transfer) profiles and efficiencies 137
A7. Modeling changes in S_e values as a function of time and concentration 139
A8. Calculations of Fickian diffusion coefficients (D) 147
A9. Tests with vapor mixtures 149

A10. References 151

LIST OF FIGURES

Figure 1.1 Cartoons of (a) a single-bed granular adsorbent tube; (b) a multi-bed granular adsorbent tube.[34] 6

Figure 1.2 Cartoon depicting a bench-top GC system.[40] 7

Figure 1.3 Five types of adsorption isotherm[42] 8

Figure 1.4 Photographs of (a) MiniRAE 3000 PID ref. 59; (b) PEN3 Portable Electronic Nose ref. 61; (c) Gasmet DX4040 FTIR analyzer ref. 71; (d) Model 4200 zNose GC ref. 65; (e) MX908 MS ref. 66; (f) HAPSITE ER GC-MS ref. 68. 13

Figure 1.5 μGC prototypes from (a) Wang et. al. in ref. 72; (b) Zhou et. al. in ref. 73; (c) Qin et. al. in ref. 74; (d) Garg et. al. in ref. 75 13

Figure 1.6 Cartoon showing the layout of a μGC system, with accompanying photographs of individual MEMS components.[92] 14

Figure 1.7 Cartoon depicting (a) and (b) trapping of VOC(s); (c) thermal desorption and injection of VOC(s) 15

Figure 1.8 Photograph of a tube preconcentrator. The o.d., i.d., and length of the stainless-steel tube are 0.64 cm, 0.54 cm, and 6 cm, respectively.[97] 16

Figure 1.9 μPCF works from (a) Bryant-Genevier et. al. in ref. 96; (b) Tian et. al. in ref. 106; (c) Camara et. al. in ref. 104; (d) Sukaew et. al. in ref. 93; (e) Pijolat et. al. in ref. 105. 19

Figure 1.10 Cartoon depicting operation of passive sampler 19

Figure 1.11 Schematic diagrams of four passive sampler configurations: (a) tube sampler; (b) permeation sampler; (c) radial sampler; (d) badge sampler.[109-113] 22

Figure 1.12 (a) dimensional diagram of μPPI (left-hand) and SEM image of μPPI grid structure (right-hand); (b) photographs of μPPI bottom layer (left-hand) and SEM image of μPPI bottom layer near one filling port (right-hand); (c) μPPI in the exposure chamber (left- hand) and μPPI mounted on the carrier PCB (right-hand).[114] 24

Figure 1.13 Typical Golay curves for three commonly used carrier gases (N_2, He, and H_2).[117] .. 28

Figure 1.14 (a) SEM image of a μcolumn on basis of anisotropic etching in ref. 129; (b) (c) SEM images of a μcolumn on basis of isotropic etching in ref. 124. 29

Figure 1.15 Schematic diagram of a VOC μsensor 30

Figure 1.16 Schematic diagram depicting the basic designs and operations of multiple sensors.[140] 30

Figure 1.17 Schematic diagram illustrating the mechanism of LSPR.[177] 34

Figure 1.18 A PCA analysis implemented with data generated by an array of 4 μCR sensors in a μGC system[188]..... 36

Figure 1.19 The schematic diagram depicting the operation mechanism of OFRR sensing[189].... 37

Figure 2.1 (a) Fluidic layout of PEMM analytical subsystem and photos of (b) segmented μcolumn, (c) microfabricated preconcentrator-focuser (μPCF), (d) μCR array. The PEMM is 7×3.7×2.3"and (f) light enough to (e) wear on the belt…….56

Figure 2.2 (a) Basic operation of the OFRR; (b) SEM image of the μOFRR (250 μm i.d.); (c) cartoon depicting the μOFRR with capillary and optical fiber connections (inset: photo of a fully packaged 2×2 cm μOFRR device on a US penny); (d) diagram of the 3-D printed jig onto which the μOFRR was mounted and fitted with optical/fluidic interconnections for facile interfacing with a GC or μGC……..58

Figure 2.3 Structures of the thiols used to make the MPNs tested as optical MV sensing films for VOCs. Acronyms are used through the report to designate the different MPNs……...59

Figure 2.4 Structure of grafting reagents used to modify the surface of diced glass.……62

Figure 2.5 Morphology of C8-MPN films cast on: (a) Piranha-washed glass; (b) HMDS-treated glass; (c) OTS-treated glass; (d) MPTS-treated glass……68

Figure 2.6 Visible transmission measurements of three plasmonic C8-MPN films casted on the glass with different solvents and their response to ~50% Csat octane vapor. A: C8-MPNs in toluene/ethanol (v: v = 1: 1) and C8-MPN film morphology under microscope; B: C8-MPNs in hexane and C8-MPN film morphology under microscope; C: C8-MPNs in hexane/ethanol (v: v = 1: 1) and C8-MPN film morphology under microscope; (Black spectrum is absorption of C8-MPNs film, red spectrum is the absorption of C8-MPNs film exposed to ~50% Csat octane vapor)…….70

Figure 2.7 Response patterns from optical transmission measurements of three plasmonic MPN films exposed to each of six vapors at 50% C_{sat}. Each 3-wavelength pattern is normalized to the largest response for (a) C8; (b) EOE (c) TEG. Wavelengths: from left to right: blue = 405 nm; green = 532 nm; red = 630 nm. Acronyms refer toVOCs: perchloroethylene (PCE), toluene (TOL), n-octane (OCT), butyl acetate (BAC), methyl ethyl ketone (MEK), isopropanol (IPA)..71

Figure 2.8 Principal components (PCA) score plot for individual vapor responses from the C8-MPN film measured by optical transmission – from Figure 2.7.(a)……..72

Figure 2.9 Response patterns of C8 MPN films to (a) PCE for different glass substrates or regions within a given substrate and (b) OCT for different glass substrates or regions within the same substrate. From left to right: blue = 405 nm; green = 532 nm; red = 630 nm. Concentrations of vapors were ~50% Csat…….73

Figure 2.10 (a) SEM image of one of our new μOFRR device structures with embedded optical fiber alignment channel; (b) PDMS-coated μOFRR mounted on a 3-D printed fixture; (c) the apparatus used to position and align the optical fiber in the top-side channel running alongside the μOFRR cavity……..73

Figure 2.11 WGM resonance shift from PDMS-coated μOFRR sensor during exposure to a high (unknown) concentration of toluene vapor……74

Figure 2.12 Responses to the test vapor 3-heptanone from the TEG-MPN coated μOFRR sensor as a GC detector. Helium at 1.2 mL/min was used as carrier gas. The 100-μL gas tight syringe injection split ratio was 80:1. Masses injected were determined on the basis of headspace concentrations assuming a vapor pressure of 0.56 kPa for 3-heptanone……...75

Figure 3.1 (a)-(d) Top and side view conceptual drawings of the μPP illustrating key features of the design and operation; A_i and L_i are the cross-sectional area and length of the formalized diffusion path segments (i = 1, 2, 3)used for modeling; (e) CAD layout for the μPP with key components labeled; (f) bottom view microscopic image of completed μPP -- inset is an IR image of a section of the periphery showing the apertures and bonding locations of the pillars; (g) SEM of a section of apertures; (h) SEM (side view) of adsorbent retention pillars; (i) PCB-mounted μPP chip (8 mm × 8 mm) with interconnecting capillary. Images and diagrams courtesy of R. Hower and J. Potkay (except for 3.1i).……..…..87

Figure 3.2 Results of TGA(exposure, purge, and desorption): (a) 2.9 mg C-X was exposed to 60 mg/m^3 of m-xylene for 100 min and N_2 for 120 min, followed by thermal desorption at 250 °C; (b) 2.9 mg C-B was exposed to 78 mg/m^3 of m-xylene for 60 min and N_2 for 120 min, followed by thermal desorption at 250 °C. Note the loss of mass during ambient-temperature purge of C-B……...102

Figure 3.3 Plot of measured (filled) and modeled (unfilled) Se values for o-xylene as a function of concentration (0.25-hr samples). The collected mass ranged from 6.1 to 14 μg and DE values were > 96%. There is < 8% reduction in sampling rate over a 2,500-fold concentration range. Agreement between experimental and modeled Se values is within 3%, except at 1500 mg/m^3 where the modeled underestimates the observed Se by 19%.....104

Figure 3.4 Plot of measured (filled) and modeled (unfilled) Se values for DEMP as a function of sample duration. The challenge concentration was 1.4 mg/m^3 except for the 0.25-hr test (55 mg/m^3). Note that Se is constant out to 4 hr, decreases by 8% for the 12-hr sample, and by 23% for the 24-hr sample. The range of transferred masses was from 25 ng to 400 ng, and DE values were > 83% in all cases. Agreement between modeled and experimental values is within 4%..105

Figure 3.5 Plot of measured (filled) and modeled (unfilled) Se values for o-xylene as a function of sample duration. The challenge concentration was 3.5 mg/m3 except for the 0.5-hr and 1-hr tests (124 mg/m^3). Note that Se decreases by 21% for the 8-hr sample, and by 30% for the 24-hr sample. The range of transferred masses was from 25 ng to 4,300 ng, and DE values were > 97% in all cases. Agreement between modeled and experimental values is within 8%, except for the 24-hr test where the modeled value is 18% too low……..106

Figure 3.6 Se values of o-xylene (filled) and DEMP (unfilled) exposed for 0.5 hr individually, as a binary mixture (see text for concentrations), and as a mixture with DMSO (140 mg/m3), DIMP (19 mg/m^3), and NMP (8 mg/m^3). For the latter, the o-xylene and DEMP concentrations were 110 and 14 mg/m^3, respectively. Analysis was by GC-FID……112

Figure 3.7 GC-FID chromatogram of 8-vapor mixture passively sampled with the μPP, transferred to the μPCF and injected. Separation used a 15 m RTX-200 column at 30 °C for 2.5 min, followed by 30 °C/min to 125 °C, then hold. The concentrations of the 8 vapors ranged

from 2 mg/m^3 (cyclohexanol) to 12 mg/m^3(cyclohexanone) and injected masses from 37 to 250 ng. DE values were > 95% except for DEMP and DIMP (~80%)…….113

Figure A1. Summary of the fabrication process flow for the µPP device. Top SOI wafer layer thicknesses: device layer, 180µm; buried oxide layer, 1.5µm; handle layer, 380 µm. Bottom borofloat glass thickness was 200 µm…….127

Figure A2. Borofloat glass bottom substrate with heaters shown in gray and Au layer at the bases of the pillars and fluidic port where eutectic bonds will occur in white. 129

Figure A3. Top substrate prior to wafer bonding, showing adsorbent cavities, adsorbent retention pillars, fill ports (3), and fluidic channel (right side). Au layer is where eutectic bonding to the bottom substrate will occur. 129

Figure A4. Photo of µPCF. Lower image is the backside heater and upper image shows the two adsorbent cavities, fill ports, and fluidic channels of the unfilled device. See ref. A2 for more details. 130

Figure A5. Diagram of the µPP test system. The three six-port valves can be switched to achieve the following three functions: 1) monitoring the concentration and composition of the test-chamber atmosphere; 2) transferring collected samples from the µPP to µPCF; 3) analyzing samples injected from µPCF by GC-FID. 131

Figure A6. Photo of the exposure chamber with µPP mounted inside it. 132

Figure A7. Profiles from the RTD readings for one heating sequence of the inner and outer adsorbent cavities, as well as the chip area (outside of the cavities) of the µPP device. 133

Figure A8. W_e values of C-X for exposure to different concentrations of m-xylene. The curve is the fitted to the Langmuir model in Eq. A.2 (R^2 = 0.96). 135

Figure A9. W_e values of several VOCs with C-X as a function of 1/(vapor pressure). Vapor pressures of toluene, m-xylene, 1,2,4-TMB, and n-decane are 3.8, 1.1, 0.28, and 0.19 kPa, respectively (R^2 = 0.98). 135

Figure A10. Desorption profiles of o-xylene from the µPP under the two indicated flow rates at 250 °C as measured with an in-line photoionization detector (mini-PID). The indicated masses collected from the test atmosphere were determined. Challenge concentrations were ~ 12 mg/m^3. 137

Figure A11. a) Top view of µPP showing radii and adsorbent beds (the blue annulus corresponds to a hypothetical saturated C-B area at a certain time point); b) Enlarged version of Fig. 3.1b showing a side view of formalized segments of the diffusion path and individual sampling rates (S_1-S_7)……..139

LIST OF TABLES

Table 1.1 Classification of VOCs (adapted from WHO)……...2

Table 1.2 Three commonly used adsorbents and corresponding properties……..5

Table 1.3 Examples of four types of passive samplers……..22

Table 3.1 Results of short-term performance tests of the μPP with 15 individual compounds…….86

Table 3.2 μPP design parameters and estimated operating parameters……...100

Table A1. Values of $M_{b\text{-}10}$ for several compounds obtained in published breakthrough tests with C-B and C-X, and the corresponding W_e values at 3.5 mg/m^3 derived therefrom. Also included are the estimates of maximum uptake masses on the C-B bed of the μPP at 3.5 mg/m^3 for the same compounds……..136

Table A2. The sampling rates and desorption efficiencies (DE) of μPP at 250 °C for DMMP with different transfer conditions (transfer flow rate and transfer time)……..138

Table A3. The sampling rates and desorption efficiencies of μPP at a transfer flow rate of 5 mL/min and transfer temperature of 275 °C for DEMP with different transfer time. 139

Table A4. Results of μPP off-gassing tests for o-xylene, DMMP, and DEMP with 4 min and 60 min purge times after exposure..... 139

Table A5. Segmental effective sampling rates (S_i) and volumes relevant to the calculation of the response time (i.e., time to steady state) of the μPP for o-xylene. 142

Table A6. Results of exposures to o-xylene and DEMP individually and in various mixtures showing no effect on observed S_e values from the presence of other vapors. 149

Table A7. Results of exposures to eight compounds individually and as a mixture showing no effect on observed S_e values from the presence of other vapors..... 150

ABSTRACT

The on-site analysis of airborne volatile and semi-volatile organic compounds (S/VOC) is critical to addressing various issues, including human exposure assessment, homeland security, disease diagnostics, and exposure limit establishment. This dissertation focuses on the development of two critical Si-microfabricated components of a microscale gas chromatograph (μGC) for the determination (i.e., identification and quantification) of S/VOCs: the preconcentrator and the detector. The first study concerned a recently invented optical microsensor called the micro-optofluidic ring resonator (μOFRR). Resonator structures comprised SiO_x cylinders ~80 μm tall with 50-250 μm i.d. and walls ≤ 2 μm thick after partial release from the Si substrate. Optical resonances, excited in the wall by coupling a modulated laser signal via a proximal optical fiber taper, shift when vapors reversibly partition into a film coated on the inner μOFRR surface. Qualitative tests with a PDMS-coated μOFRR confirmed resonance shifts upon exposure to each of three VOCs. Similar tests using μOFRR devices coated with a functionalized monolayer-protected Au nanoparticle (MPN) or a functionalized Au nanorod also gave positive results. Implementation of the MPN-coated μOFRR as a detector for a conventional GC yielded low-ng level detection limits. The second study concerned a so-called microfabricated collector-injector (μCOIN). As conceived, the μCOIN would consist of two series-coupled devices, a micro passive preconcentrator (μPP) and a micro progressively heated injector. Here we describe the design, construction, and characterization of the μPP. Discrete devices (8 × 8 mm chips) were made from a micromachined silicon-on-insulator top layer and a glass bottom layer, joined by Si-

Au eutectic bonding. The top layer has an array of 237 square apertures (47 × 47 μm) distributed around the periphery of a 5.2-mm diameter circular region through which vapors diffuse at predictable rates. Two concentric annular cavities, separated by Si pillars and offset inwardly from the apertures, are packed with ~800 μg each of the graphitized carbon adsorbents Carbopack B (outer) and X (inner). Thin-film Pt heaters on the bottom substrate are used to thermally desorb captured S/VOCs, which are drawn by a downstream pump through the center of the device to a micro focuser and then injected to a bench scale GC for analysis. Test compounds included common solvents and chemical warfare agent simulants, which spanned a vapor pressure range of 0.033 to 1.1 kPa. Effective (diffusional) μPP sampling rates ranging from 0.16 to 0.78 mL/min were observed for short-duration samples among the 15 test compounds. Agreement between observed and modeled sampling rates was generally within ±15%, with exceptions explicable by one or more factors. Sampling rates for two representative compounds, diethylmethylphosphonate and o-xylene, declined by only ~20-30% from 0.25 to 24 hr of continuous exposure at fixed, low concentrations of these compounds. For o-xylene, the sampling rate declined by only 8% over a ~2,300-fold conc. range at a fixed sampling period of 0.25 hr. A model was developed that could estimate decreases in sampling rates as a function adsorbent saturation and time. Desorption/transfer efficiencies were > 85% for all individual vapors (most > 95%) at 250-275 °C in 60 sec at 5 mL/min. Sampling rates for mixtures of up to eight compounds matched those for the individual compounds. Possible design revisions for next-generation devices are presented.

Chapter 1

Introduction, Background, and Significance

1.1 Dissertation Overview

This dissertation describes the development of two critical components in a microscale gas chromatograph (μGC) for the analysis of volatile and semi-volatile organic compounds (S/VOC): the preconcentrator and the detector. The primary focus is on the modeling and performance characterization of a microfabricated passive preconcentrator (μPP) intended ultimately for use in a μGC system. The design, fabrication, and performance characterization of a microfabricated optofluidic ring resonator (μOFRR) sensor intended ultimately for use as a detector in a μGC system is also described.

This research is a part of the long-standing efforts of the Zellers group to develop μGC systems that enable the *in-situ* analysis of S/VOCs by use of so-called Micro-Electro-Mechanical Systems (MEMS) fabrication techniques. The remainder of Chapter 1 describes the background and significance of the research in this dissertation. Chapter 2 describes the fabrication, coating and performance characterization of μOFRR sensors coated with different functionalized nanomaterials, as a preliminary study for improving the VOC selectivity. Chapter 3 details the design, fabrication and characterization of a μPP device. Specifically, performance over a wide range of concentrations and time with various S/VOCs and mixtures is reported. In addition, the VOC adsorption capacities of two adsorbents are studied. Some of the work in Chapter 3 has been

published in the Proceedings of the 20th International Conference on Solid-State Sensors, Actuators and Microsystems, Transducers '19. A manuscript is being prepared for publication in a peer-reviewed journal.

1.2 Volatile and Semi-Volatile Organic Compounds

The term "volatile organic compound" has multiple definitions. The United States Environmental Protection Agency (EPA) defines VOC as "any compound of carbon, excluding carbon monoxide, carbon dioxide, carbonic acid, metallic carbides or carbonates and ammonium carbonate, which participates in atmospheric photochemical reactions".[1] The World Health Organization (WHO) defines and categorizes VOCs based on their boiling points as shown in Table 1.1. The n-alkanes listed in Table 1.1 are used as references. VOCs are also defined as "organic chemical compounds whose composition makes it possible for them to evaporate under normal indoor atmospheric conditions of temperature and pressure".[2] The definition has been used in multiple scientific literatures.[2] This dissertation also uses this broad definition, and as such the term 'VOC' covers all the compounds ranging from very-volatile organic compound (VVOC) to semi-volatile organic compound (SVOC).[2]

Table 1.1 Classification of VOCs (adapted from WHO)

Category	Boiling Point Range (°C)	Reference n-alkane	Reference p_v Range (mmHg)	Example Compounds
VVOC	<0 to 50-100	n-C1 to n-C7	4.7×10^{5} to 46	1-pentyne, propane
VOC	50-100 to 240-260	n-C8 to n-C12	14 to 0.14	o-xylene, diethyl methylphosphonate
SVOC	240-260 to 380-400	n-C13 to n-C30	0.038 to 2.7×10^{-11}	diethanolamine, tetraethylene glycol dimethyl ether

VOCs are ubiquitous in both outdoor and indoor environments since they are essential ingredients in various manufactured materials and products, including paints, household chemicals,

inks, fuel and so on.[3] Due to the diverse health effects of some VOCs,[4] the accurate assessment of exposure to these VOCs is critical to numerous problems regarding protecting the health of workers and the public, including defining exposure-response relationships in epidemiologic studies among worker populations,[5] establishing workplace exposure limits,[6,7] determining compliance with such limits,[8,9] diagnosing diseases,[10,11] and assessing indoor air quality.[12] Detection and analysis of VOCs are also a priority of the Intelligence Community (IC). Applications for the IC include but are not limited to facility and border protection, forensic analysis, production monitoring, and control of narcotics and illicit drugs. The examples of the VOCs that are of interest in the IC include explosives and energetics, chemical warfare agent (CWA) simulants and interferences, illicit drugs and their precursors, toxic industrial/environmental chemicals, nuclear fuel cycle materials, and products of forest fires.[13-19] Automated on-site monitoring of these VOCs over long periods of time is an interest of the IC. Additionally, the rapid warning of these VOCs remains a critical element of public safety.

1.2.1 Health Effects of VOCs

The types of health effects due to VOC exposures vary greatly. The health effects can be classified as acute and chronic. Generally, acute effects occur after exposures of short durations while chronic effects occur as a result of repeated long-term exposures. Short-term exposures to high concentrations of VOCs may result in headaches, dizziness, memory problems, and skin and respiratory tract irritation, whereas long-term exposures to VOCs may cause loss of coordination, cancer, or damage to the liver, kidney and central nervous system.[20,21]

To prevent occupational exposure to VOCs, regulations and recommendations on exposure limits have been established in the U.S., including Permissible Exposure Limits (PELs) issued by the Occupational Safety and Health Administration (OSHA),[22] Threshold Limit Values (TLVs) of

the American Conference of Governmental Industrial Hygienists (ACGIH),[23] and Recommended Exposure Limits (RELs) of the National Institute for Occupational Safety and Health (NIOSH).[24] Although tens of thousands of VOCs exist in various products and materials, less than 1,000 of them have corresponding regulations.[9,25,26] The lack of data of exposures to VOCs has been considered as the most critical factor impeding the epidemiologic studies on defining the relationship between the exposures and the health impacts. This hinders the efforts to establish permissible exposure limit which rely on the results of such relationships.

CWAs are extremely toxic synthetic chemicals. They generally have lower lethal dose than industrial VOCs.[27,28] Based on the volatility, CWAs can be classified as non-persistent (high volatility) and persistent (low volatility) agents. An agent with high volatility tends to evaporate and disperse fast. CWAs can be also classified according their physiological effects on humans into seven categories including nerve agents, blister agents, blood agents, choking agents, riot-control agents, psychomimetic agents, and toxins.[29] Examples of S/VOCs that are CWAs include sarin, sulfur mustard, and lewisite.[28] When there is a release of unknown CWAs, the important emergency responses include (1) qualitative identification and quantitative determination of the CWAs; (2) physical protections, e.g. protective masks and clothing, to create a barrier between the CWAs and the humans; (3) decontamination, i.e. reduction or removal of the CWAs. The rapid identification and quantification of unknown CWAs are critical since they can determine the selection of protective measures and decontamination strategies.[29]

1.3 Traditional Methods of VOC Sampling and Analysis

The quantitative evaluation of exposures to VOCs is a challenging problem. NIOSH, OSHA, and EPA made significant contributions to design and evaluation of methods for VOC

sampling and analysis.[30-32] A typical method describes the details of sampling procedure, sample preparation, and subsequent analysis procedure.

The time of a sampling procedure typically ranges from 15 minutes to several hours. As such the results of the VOC exposure analysis are time-averaged exposure concentrations. The air sample is drawn into a sample container, e.g. sampler, by a sampling pump under a predefined flow rate. The containers have three main categories including air storage devices (polymeric sampling bags and stainless steel canisters), collectors relying on liquid adsorption and chemical reaction (midget impingers and fritted bubblers), and solid-adsorption-based collectors (granular adsorbent tubes). Among the three samplers, the granular adsorbent tube is the most commonly used due to its capability to concentrate the samples at the surface of the micropores of the adsorbent. There are varieties of adsorbents used in the field of granular adsorbent tubes. Three commonly used adsorbents are shown in the Table 1.2. Other adsorbents include silica gel, petroleum charcoal, coconut charcoal, activated coconut charcoal, florisil, poly urethane foam, and molecular sieves (Zeolites).[33,34]

Table 1.2 Three commonly used adsorbents and corresponding properties[33]

Category	Examples	Surf. Area (m^2/g)	Max. Desorp. Temp. (°C)	Cmpds Designed to be Retained and Released
Graphitized Carbons	Carbopack-X, Carbopack-B	5 - 240	> 400	Mid to large M.W. cmpd
Porous Polymers	Tenax TA, Chromosorb 106	24 - 795	220 - 350	Mid to large M.W. cmpd
Carbon Molecular Sieves	Carboxen-1003, Carbosieve-SIII	400 - 1200	> 400	Small M.W. cmpd

Choosing the proper adsorbent is often difficult. The proper adsorbent needs to not only be capable of retaining an individual or group of analyte(s) during sampling but also be able to release the analyte(s) during desorption. The adsorbent selection would be a very difficult task when the

target analytes cover a wide range of polarities and vapor pressures. To solve the difficulties, some studies used multi-bed granular adsorbent tubes which place a weaker adsorbent at the sampling inlet followed by a stronger adsorbent.[35-38] Examples of the multi-bed granular adsorbent tubes include Carbotrap 217 and Carbotrap 349, which can be used in EPA TO-17 method and NIOSH 2549 method, respectively. The multiple adsorbents facilitated striking a balance between strong adsorption by virtue of higher surface area adsorbents and efficient desorption due to the lower surface area adsorbents. Examples of a single-bed and a multi-bed granular adsorbent tubes are shown in Figure 1.1.

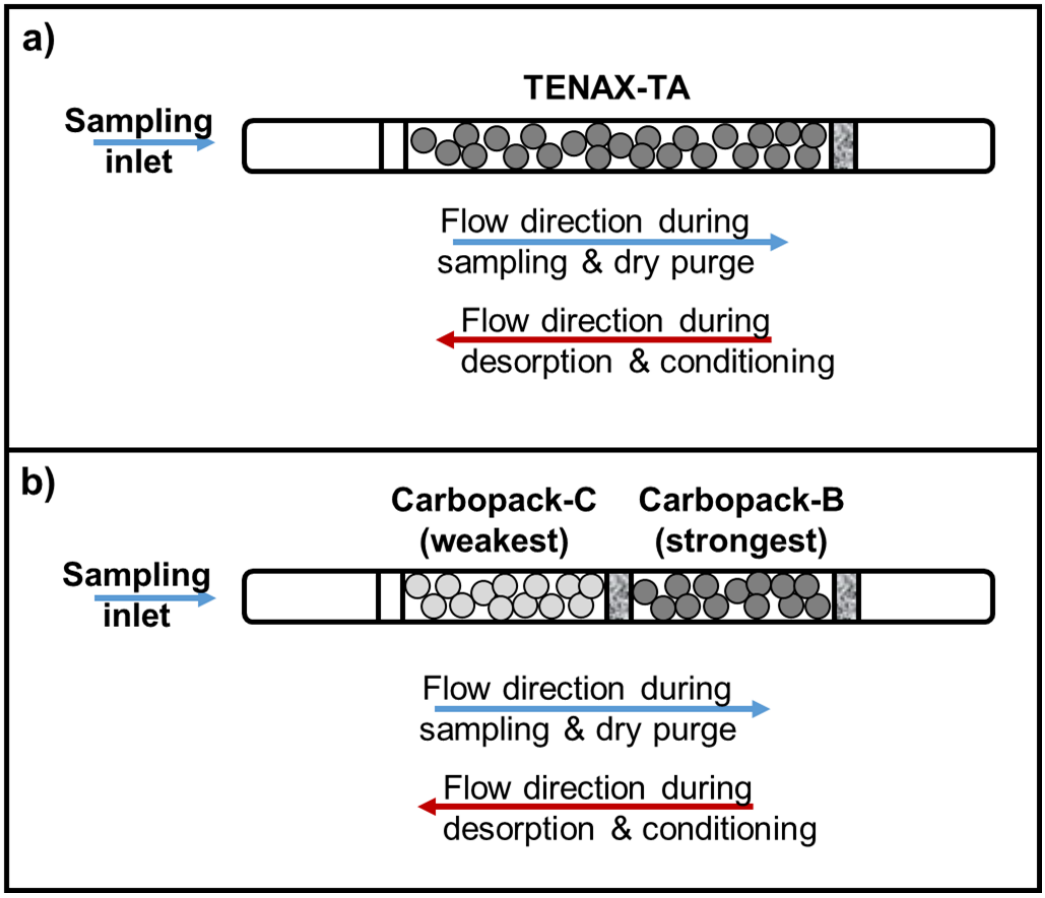

Figure 1.1 Cartoons of (a) a single-bed granular adsorbent tube; (b) a multi-bed granular adsorbent tube.[34]

After sampling, the exposed samplers require typically standard solvent or thermal extraction for subsequent analysis. Gas chromatography (GC) is a common technique to analyze mixtures of VOCs in the ambient air.[39] A bench-top GC system is shown in Figure 1.2. The basic principles of a bench-top GC that is operated in the laboratory include: 1) the sample VOC mixture is injected into a heated injection port where the sample is volatilized; 2) the sample is swept by the inert carrier gas into a separation column; 3) the compounds in the mixture are separated in the column based on the different interaction strengths of compounds with the polymeric stationary phase, e.g. PDMS, coated on the wall of the column; 4) the separated compounds elute from the column and are quantified by a detector by measuring the integrated area or the height the of signal peak; 5) the retention time is generally used to identify each of compounds in the sample mixture, and the identification can be enhanced when a mass spectrometer is used by virtue of the fragmentation pattern.[39]

Although the traditional sampling and analytical methods are reliable, they have some disadvantages. The use of the methods requires submission of exposed samplers to the laboratory after sampling, which raises the cost per sample and delays results from being obtained.

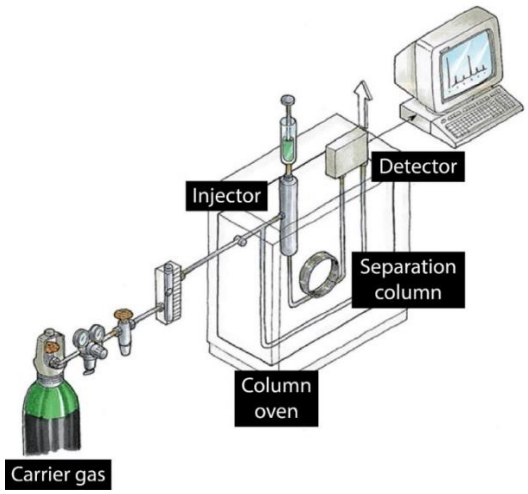

Figure 1.2 Cartoon depicting a bench-top GC system.[40]

1.4 Adsorption Theory

Adsorption capacity (W_e) is the quantity of adsorbate (vapor) taken up per unit weight of the adsorbent at equilibrium status. It can be determined statically or dynamically.[41] The difference between the two terms is a flow passing through the adsorbent during adsorption for the dynamic adsorption capacity. Generally, the dynamic adsorption capacity, determined from breakthrough testing by flowing a vapor challenge through a bed of the adsorbent, is lower than the static adsorption capacity, determined by direct mass uptake from a headspace test atmosphere.

Adsorption isotherms determined statically correlate W_e with the partial pressure or concentration of the adsorbate at constant temperature. In general, W_e increases with concentration. The adsorption isotherm can generally be classified into one of five types, which are shown in Figure 1.3.[42] Various isotherm models have been built to fit the five general forms such as linear isotherm, the Langmuir isotherm (Type I), Freundlich isotherm (Type I), and Brunauer, Emmet, and Teller (BET) isotherm (Type II).[43] The most commonly used isotherm model for studies of VOC adsorbates is the Langmuir isotherm.

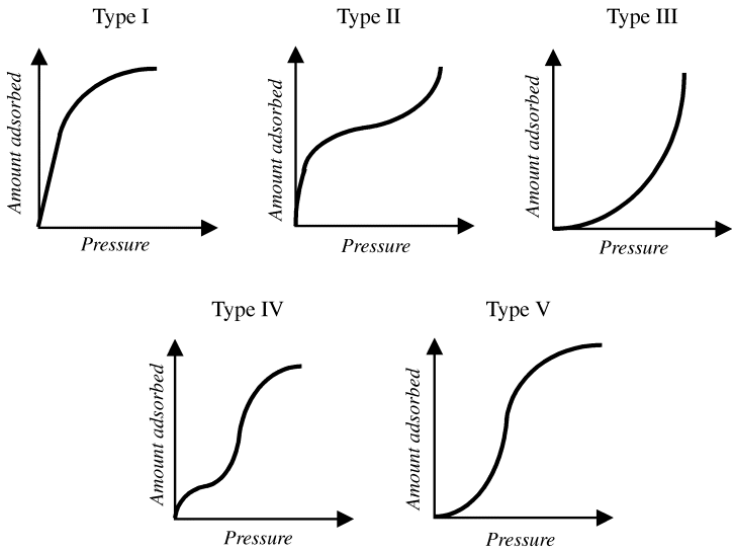

Figure 1.3 Five types of adsorption isotherm[42]

It has been found that the adsorption capacity is related to the concentration, vapor pressure, polarity and functionality of the VOC and the specific surface area of the adsorbent.[44] VOC adsorption behavior has been reported in a number of studies, most of which used the activated carbon adsorbents.[46-52] But studies also reported the VOC adsorption capacity for other adsorbent, i.e. porous clay heterostructures and activated carbon fiber.[53,54] Most of the existing studies showed that the VOC adsorption could be modelled accurately using the Langmuir adsorption isotherm. The expression of Langmuir adsorption isotherm model is shown as follows:

$$W_e = W_{e-max} \frac{b \times C}{1 + b \times C} \quad \text{Eq. 1.1}$$

where $W_{e\text{-}max}$ is the maximum monolayer coverage capacity (μg/g), b is the Langmuir isotherm constant (L/mg), and C is the VOC concentration (mg/m^3). The main assumptions of this model are shown as follows:[55]

- Definite vacant sites are available on the adsorbent surface.
- All the vacant sites are equivalent.
- The adsorbent surface is covered by a monolayer of adsorbate molecules.
- There are not interactions among adsorbate molecules.

The dynamic adsorption capacity can be determined from breakthrough testing of a microfabricated preconcentrators (μPC) by flowing vapor(s) in sample air through the μPC and monitoring the downstream breakthrough. There are two important performance parameters of a μPC, the breakthrough volume (V_b) and breakthrough time (t_b). They are defined as the air volume and time required to observe the exit concentration of a μPC to reach a predefined fraction of the inlet concentration, respectively. The equations in the modified Wheeler model (MWM) describe V_b and t_b, as follows:

$$V_b = \frac{W_e W_b}{C_0}\left[1 - \frac{1}{k_V \tau}\ln\left(\frac{C_0}{C_X}\right)\right] \quad \text{Eq. 1.2}$$

$$t_b = \frac{\rho_b W_e}{C_0}\left[\tau - \frac{1}{k_V}\ln\left(\frac{C_0}{C_X}\right)\right] \quad \text{Eq. 1.3}$$

where W_e is the dynamic adsorption capacity (g/g), W_b is the adsorbent mass (g), C_0 is the concentration at the μPC inlet (g/cm^3), k_v is the kinetic rate constant (min^{-1}), C_X is the concentration at the μPC outlet (g/cm^3), ρ_b is the adsorbent bed density (g/cm^3), τ is bed residence time (min) that can be described as follows:

$$\tau = \frac{W_b}{\rho_b Q} \quad \text{Eq. 1.4}$$

where Q is the volumetric flow rate (cm^3/min).

1.5 Portable Analytical Instruments for VOCs

Portable analyzers enable the on-site analysis of VOCs, thus reducing the cost of VOC analysis. The analyzers often permit real time detection, thus being called direct reading instruments. Current portable VOC analyzers can be roughly classified into three categories according the selectivity.[56,57] The first category refers to analyzers with poor selectivity. They generally measure the total volatile organic compounds (TVOCs), thus being known as universal VOC detectors[12]. Examples of such analyzers include the MicroFID II flame-ionization detector (FID) from INFICON and the MiniRAE 3000 photo-ionization detector (PID) from RAE Systems.[58,59] Although having relatively low prices and high sensitivity, use of these types of analyzers is restricted by the lack of selectivity. VOCs typically exist as mixtures, and these universal detectors can not identify the types of the VOCs. The detectors have different sensitivities for different VOCs so that they are not capable of providing accurate concentration

measurements for TVOCs. Generally, the detectors are used for vapor leak detection. FIDs and PIDs are also used as GC detectors.

The second category includes those detectors which have moderate selectivity. The examples in this category include sensor arrays. The sensor array is sometimes called an "electronic nose", which is composed of an array of standalone sensors. Examples of the sensor arrays include the FOX and GEMINI Electronic Noses from Alpha MOS and the PEN3 Portable Electronic Nose from AIRSENSE Analytics.[60,61] The moderate selectivity of sensor arrays is achieved by use of different interface materials/transducing mechanisms or probing different properties of a single film. A sensor array typically can generate multiple signals, i.e. a signal pattern. By applying pattern recognition techniques, e.g. neural network, K-nearest-neighbor (KNN), and principal component regression, the sensor arrays have presented moderate ability to differentiate among individual VOCs and some simple mixtures, but their performance of recognition is not good for complex mixtures.[62,63]

Detectors of the third category have good selectivity. The GC and mass spectrometry (MS) systems are examples of analyzers of this type. Portable GC instrumentation permits on-site VOC mixture analysis, such as ambient/workplace air or water pollution monitoring, drug or explosives detection, and point-of-care diagnostic testing. The selectivity of GC systems is achieved by the separation of VOC mixtures in space when the mixtures travel through a GC column. Examples of portable GC systems include the Model 4200 Portable zNose from Electronic Sensor Technology and the FROG-4000 Portable GC from Defiant Technologies.[64,65] Although the current portable GC instruments can achieve the on-site analyses of VOC mixtures, their defects include relatively large size, high cost, and high power consumption that collectively limit the routine or long-term deployment on battery power.

Portable MS systems have increased in popularity. One example of MS systems is the MX908 from 908 Devices.[66] In a typical MS analysis procedure, a sample is ionized during which the sample molecules may get smashed into small charged fragments, i.e. ions. These ions are separated by an electric or magnetic field due to different mass-to-charge ratios of the ions. The separated ions are then measured by a detector which can analyze charged particles. The identification of molecules is achieved by comparison to a library of reference fragmentation spectra of known compounds.[67]

Portable gas chromatography–mass spectrometry (GC-MS) instrumentation combines the features of GC and MS systems. Examples of the portable GC-MS instrumentation include the HAPSITE ER Chemical Identification System from INFICON, the Griffin G510 portable GC-MS from FLIR Systems, and the Torion T-9 Portable GC/MS from PerkinElmer.[68-70] Although they are almost the best VOC analyzers in the market and have grown in popularity, their use is limited by the large size, demand for high vacuum, and high price and power consumption.

Another example of the third category is IR systems. One example of IR systems is Gasmet DX4040 from Gasmet Technologies.[71] The FTIR analyzers can often analyze multiple compounds simultaneously, provide results rapidly (a few seconds to tens of seconds), and have a relatively low detection limit (sub-ppm level). The selectivity of IR systems is achieved by virtue of varying absorbance wavelengths and intensities of different VOCs. Although having shown capability to recognize VOCs, the systems have relatively large size.

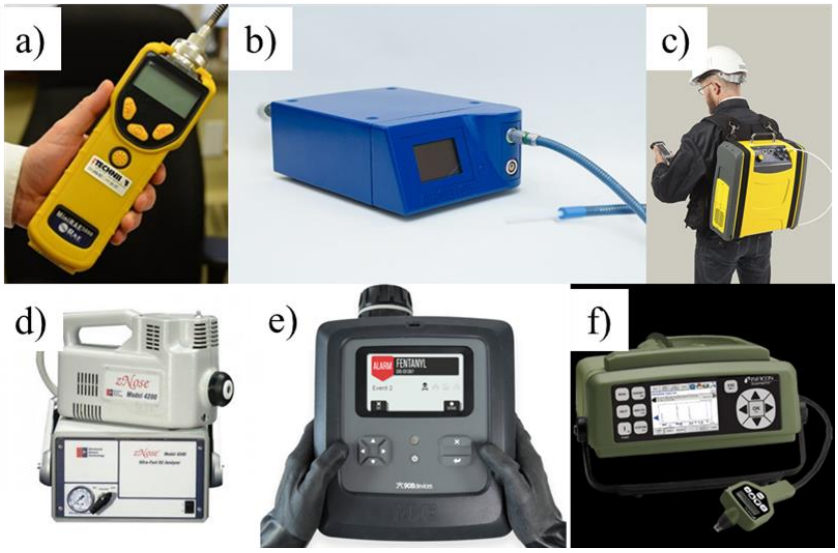

Figure 1.4 Photographs of (a) MiniRAE 3000 PID ref. 59; (b) PEN3 Portable Electronic Nose ref. 61; (c) Gasmet DX4040 FTIR analyzer ref. 71; (d) Model 4200 zNose GC ref. 65; (e) MX908 MS ref. 66; (f) HAPSITE ER GC-MS ref. 68.

1.6 Microfabricated GC

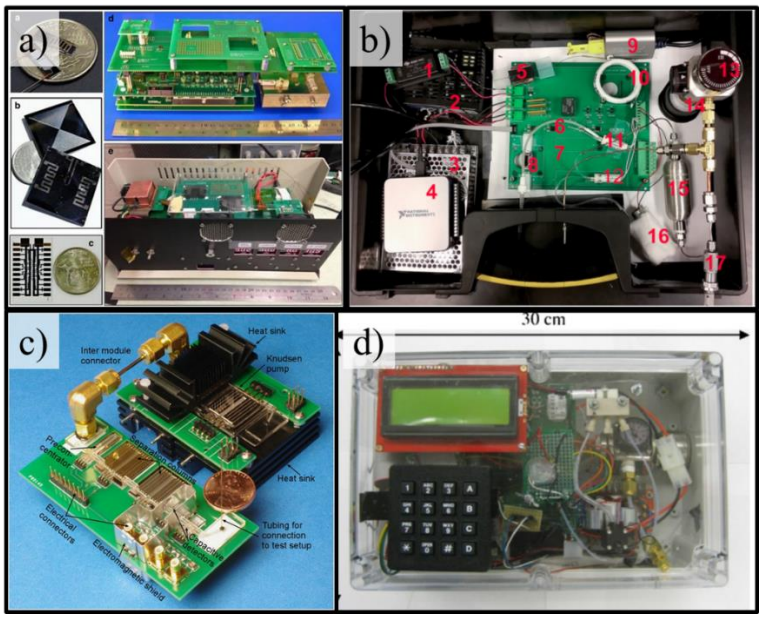

Figure 1.5 µGC prototypes from (a) Wang et. al. in ref. 72; (b) Zhou et. al. in ref. 73; (c) Qin et. al. in ref. 74; (d) Garg et. al. in ref. 75

The µGC systems,[76] integrating MEMS based components, have been attracting great interest from research groups at the University of Michigan,[73,77-82] the University of Illinois,[83-85]

Sandia National Labs[86,87] and Virginia Tech[75,88] because of their potential for reducing the size, cost, and power consumption of GC systems. Examples of the μGC systems are shown in Figure 1.5. μGC systems have been produced by several instrument manufacturers. Examples of commercial μGC systems include the GCAP from Analytical Pixels Technology (APIX) and Zebra-GC from Zebra Analytix.[89-91] A μGC system, such as the hypothetical systems shown in Figure 1.6, usually includes an adsorbent-packed μpreconcentrator that also serves as an injector, a μcolumn coated with stationary phase, and a μsensor array or other detector. Although the reductions in size associated with microfabrication lead to commensurate reductions in heating power requirements, overall power demands in reported μGC systems remain high, and represent a limiting factor in simultaneously meeting goals of high performance, miniaturization, and long-term battery operation. Additionally, most of the GC scaling laws favor the miniaturization of components in μGC systems, however, the reduced length of separation column results in the loss of resolution (a characteristic of the separation between two peaks with different retention time) and peak capacity (the number of compounds that can be separated in a single analysis).

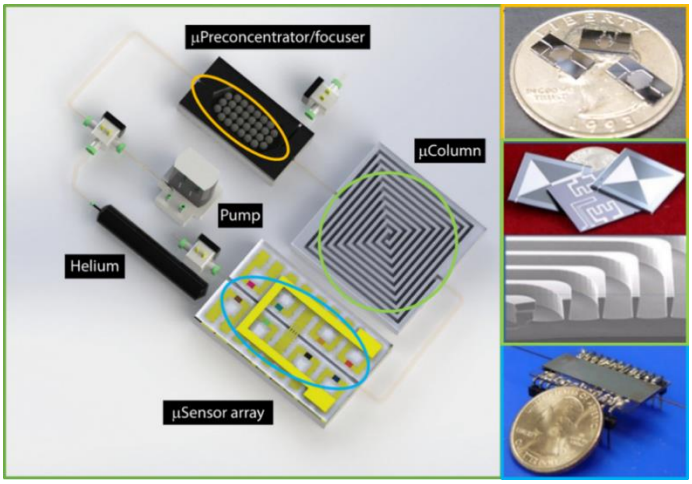

Figure 1.6 Cartoon showing the layout of a μGC system, with accompanying photographs of individual MEMS components.[92]

1.6.1 Microfabricated Preconcentrators

1.6.1.1 Active Preconcentrators and Microfabricated Preconcentrators

Preconcentration involves two main procedures: 1) trapping of VOC(s) in a large volume of sample air with adsorbent(s); 2) thermal desorption and injection into the downstream separation column in a much smaller volume.[93] The preconcentration process is shown in Figure 1.7. By virtue of the preconcentration, the analytes can generally be injected as a focused band, which would improve subsequent separation or detection. The performance of preconcentration can generally be quantified by the preconcentration factor (PF). The definition of PF is the ratio of the collected air sample volume to the volume of the space containing all the analytes at the point of detection.[93] This assumes conservation of mass, i.e. exhaustive trapping and desorption of the vapor(s) in the preconcentrated sample.

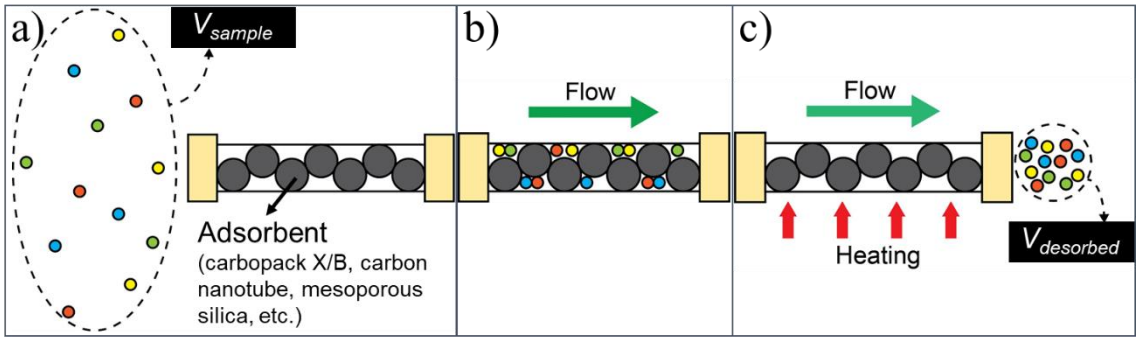

Figure 1.7 Cartoon depicting (a) and (b) trapping of VOC(s); (c) thermal desorption and injection of VOC(s).

Conventional packed-bed preconcentrators use a stainless steel/glass tube to contain the granular adsorbent material. The stainless steel tube itself or a heating wire coiled around the tube is employed as heater during the thermal desorption.[94,95] Fabrication of these preconcentrators is not complex and does not require any MEMS techniques. However, they have a large dead volume as well as low heating efficiency, which broadens the injection band.

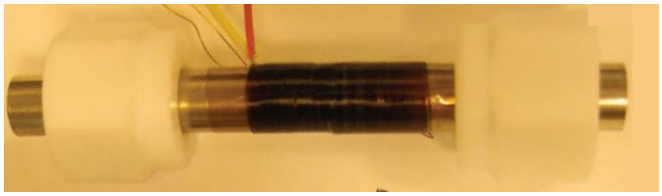

Figure 1.8 Photograph of a tube preconcentrator. The o.d., i.d., and length of the stainless-steel tube are 0.64 cm, 0.54 cm, and 6 cm, respectively.[97]

The µPC have presented promise to outperform the tube preconcentrators by virtue of MEMS techniques and improved design of fluidic channels and heaters.[13,75,96,98] They are capable of being integrated into a µGC system. However, the design of µPCs faces many issues that are not generally considered in developing tube preconcentrators due to the miniaturization. The µPCs not only need to have sufficient adsorption capacity to enable the quantitative analysis, but also demand minimized bed mass to reduce heating power, heating efficiency, and dead volume, and thus the desorption bandwidth. Achievable sampling flow rate is also a problem which depends on the pressure drop of µPC adsorbent bed and the pumping capability.

In order to facilitate the design and characterization of µPCs, the modified Wheeler model (discussed in 1.4) that correlates several design and performance parameters of a µPC with retention capacity of an adsorbent bed has been employed in previous µPC studies.[95,96] In Eq. 1.2, the term $\frac{W_e W_b}{C_0}$ is the volume of air sample containing VOC(s) required to reach the thermodynamic equilibrium while the term $1-\frac{1}{k_V \tau}\ln(\frac{C_0}{C_X})$ is called the adsorption efficiency.[95] This equation suggests that the breakthrough volume decreases with increasing concentration at the µPC inlet, decreasing bed residence time, and decreasing adsorbent mass. The increase of concentration at the µPC inlet can accelerate the saturation of adsorption sites, thereby reducing the breakthrough volume. The reduction of breakthrough volume as C_0 increases is offset by the W_e increase with

C_0. However, this offset effect gradually diminishes with C_0 since relationship between W_e and C_0 typically follows a Langmuir isotherm model. As bed residence time decreases, the time available to find and get trapped by adsorption sites for analytes decreases when they pass through the adsorbents, which might result in the decrease in breakthrough volume. Similarly, the decrease in adsorbent mass would reduce the number of adsorption sites, which would lead to the reduction in breakthrough volume.[95]

Based on the device design, most of reported µPCs can be classified into two categories: equilibrium µPC and exhaustive µPC.[96] In equilibrium µPCs, only a fraction of the VOC(s) is trapped by the adsorbents when the air sample passes through the device during sampling. The quantitative analyses of these µPCs are based on the adsorption equilibrium status established between the concentrations of adsorbent surface and atmosphere containing the VOC(s). Although these equilibrium µPCs can increase the detection sensitivity significantly, it is not possible to calculate a bonafide PF due to the partial mass loss during the sampling procedure. Most reported µPC employ this equilibrium approach.

One example of the equilibrium µPC is the µPC developed by researchers at Sandia National Laboratories.[86,99] The main structure is an integrated platinum microhotplate coated with surfactant templated sol gel layer as adsorbent. By virtue of the adsorption selectivity, the device achieved the collection of some chemical warfare agents, i.e. dimethyl methyl phosphonate (DMMP) at ppb concentration, from a range of background interferences. Martin et al. developed an equilibrium µPC having a similar planar structure.[100] The device comprises microfabricated dual serpentine platinum heaters coated with adsorbents (functionalized carbosilane sorbent polymer). The polymer used in the study also has selectivity, which enables the collection of

analytes of interest, 2,4,6-trinitrotoluene (TNT), and thereby achieves the trace explosives detection.

As for exhaustive μPCs, the entire mass of VOCs in the air sample are trapped, which makes the measurement of the VOC concentration more straightforward. Additionally, the legitimate PF can be calculated. The Zellers group has developed multi-stage exhaustive microfabricated preconcentrator-focuser (μPCF) devices.[93,96,97,101] The name reflects the dual functions of the device: sample collection and injection with a focused band. Devices were packed with one/several types of granular solids, Carbopack X (C-X), Carbopack B (C-B), and Carboxen 1000 (C-1000). Each type of material was loaded into an individual microfabricated cavity flanked by retaining micropillars. The multi-stage design, achieved with adsorbents differing in specific surface area, leads to a balance between strong adsorption (high capacity) and efficient desorption (lower temp. and time for desorption) and allows effective preconcentration and injection of a wider range of VOCs than could be achieved with a single-adsorbent design. One μPCF device enabled the analyses of mixtures of ~10-20 compounds with vapor pressure values ranging from 0.03 to 13 kPa and PFs ranging from 200 to 1,600.[96]

The Agah group at Virginia Tech has developed an exhaustive μPC composed of microposts embedded in the microfabricated cavity with deposited Cr/Ni stack as integrated heaters and temperature sensors.[75,102,103] The adsorbent used was a thin film of Tenax Ta coated witk the inkjet printing principle. Researchers at Ecole Nationale Supérieure des Mines and University of Neuchâtel reported exhaustive μPC devices with carbon nano-powders as adsorbents.[104,105] They presented that the porous silicon facilitates the adsorbent deposition procedure in the micro-channels as well as reduces the temperature required for desorption. It

achieved the successful collection and injection for benzene at sub-ppm concentrations. But the preconcentration factor was only ~55.

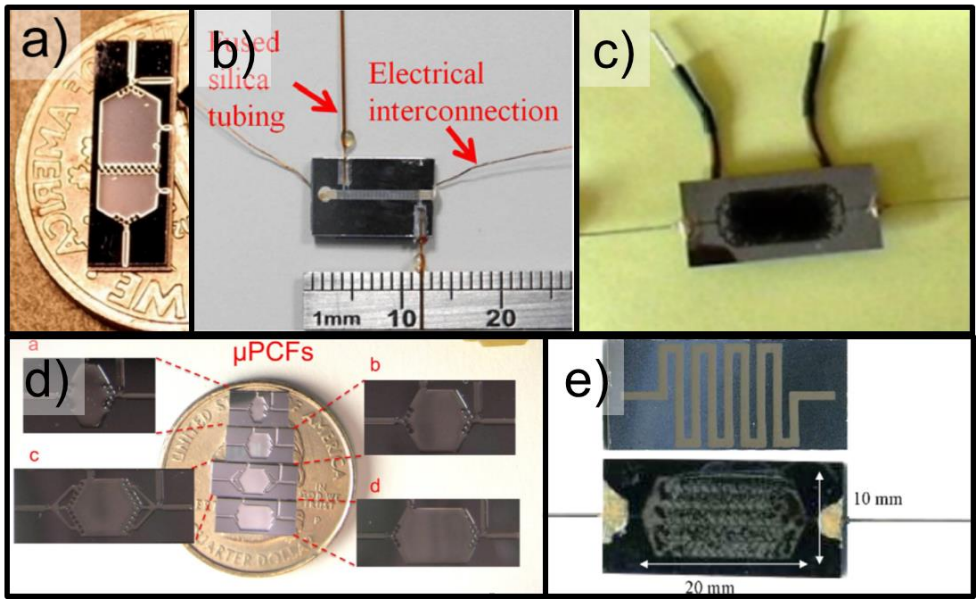

Figure 1.9 μPCF works from (a) Bryant-Genevier et. al. in ref. 96; (b) Tian et. al. in ref. 106; (c) Camara et. al. in ref. 104; (d) Sukaew et. al. in ref. 93; (e) Pijolat et. al. in ref. 105.

1.6.1.2 Theory of Passive Sampling

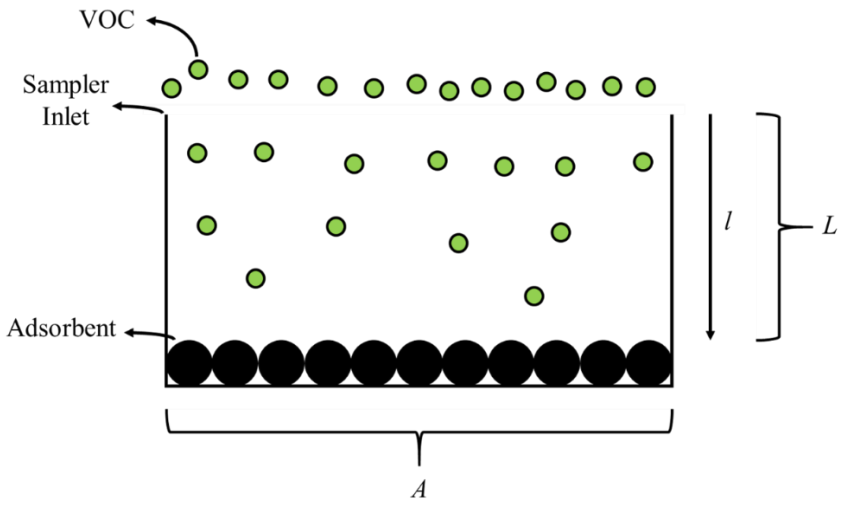

Figure 1.10 Cartoon depicting operation of passive sampler

The operation of passive samplers relies on the molecular diffusion of gaseous analytes through a defined pathway onto an adsorbent or other trap. Unlike active samplers, passive samplers do not require a pump to transfer vapors into the device during sampling. Passive samplers are inexpensive, easy to use (no pump calibration or operation), and noiseless. The basic operation of a passive sampler is shown in Figure 1.10. VOCs diffuse toward the surface of adsorbents along the length of the diffusion path due to the concentration gradient. It is assumed that A is the cross sectional area of the sampler and L is the diffusion path length, i.e. the length of quiescent diffusion zone in the sampler. The effective sampling rate of a passive sampler can be derived from Fick's first law:

$$j = -D\frac{dC(l)}{dl} \qquad \text{Eq. 1.5}$$

where j is the vapor flux (μg cm^{-2} s^{-1}), D is the vapor diffusion coefficient (cm^2/s), C is the vapor concentration ($\mu g/cm^3$), and l represents the location on the flow path (cm). It should be noted that C is a function of l. Assuming steady-state conditions have been achieved such that j is a constant, we have:

$$\int_0^L jdl = \int_{C_0}^{C_1} -DdC(l) \qquad \text{Eq. 1.6}$$

i.e.

$$jL = D[C_0 - C_1] \qquad \text{Eq. 1.7}$$

where C_0 and C_1 are the concentration in the ambient atmosphere and at the surface of the adsorbent, respectively. Based on the definition of vapor flux (j), we can get:

$$j = \frac{M}{At} \qquad \text{Eq. 1.8}$$

where *t* is the sampling time (s), and *M* is the vapor mass passing to the adsorbent during the sampling time (μg). Based on Eq. 1.7 and Eq. 1.8, we can get:

$$\frac{D[C_0-C_1]}{L} = j = \frac{M}{At} \quad \text{Eq. 1.9}$$

Assuming that the air concentration at the surface of the adsorbent, i.e. C_1, is 0, we can get:

$$S_e = \frac{M}{C_0 t} = \frac{DA}{L} \quad \text{Eq. 1.10}$$

where S_e is the effective sampling rate (mL/min). Put another way, S_e is the volume of contaminated air passing through the sampler per unit time. As shown, S_e is simply a function of the physical dimensions of the sampler and the diffusion coefficient of the analyte. Although Eq. 10 suggests that S_e is a function of the air concentration of the vapor, since *M* increases in direct proportion to C_0, in fact, S_e is independent of concentration.

1.6.1.3 Passive Sampling Devices

Commercial passive samplers have been available for decades. They are small, wearable devices that can be used to collect personal breathing zone samples of VOCs.[107,108] Based on their configurations, they can be classified into four categories including tube samplers, permeation samplers, radial samplers, and badge samplers.[109] Their schematic diagrams are shown in Figure 1.11. Examples of these four types of passive samplers are presented in Table 1.3. As discussed above, the effective sampling rate of a passive sampler increases as the cross sectional area of the sampler increases and as the diffusion path length decreases. Thus, the tube passive samplers generally have relatively low sampling rate due to the small cross sectional area and long diffusion path length while the radial samplers have relatively high sampling rates by virtue of the large cross sectional area and short diffusion path length.

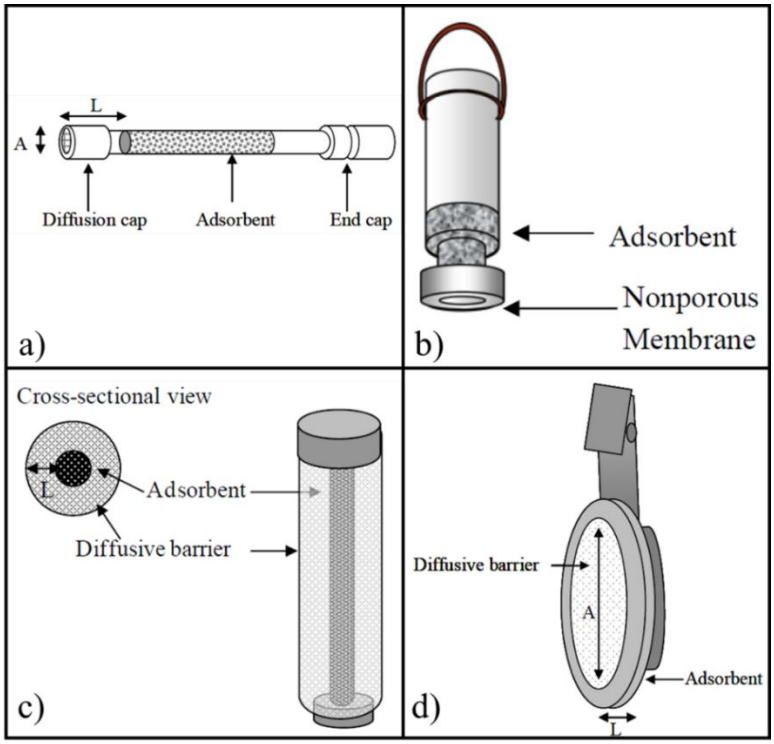

Figure 1.11 Schematic diagrams of four passive sampler configurations: (a) tube sampler; (b) permeation sampler; (c) radial sampler; (d) badge sampler.[109-113]

Table 1.3 Examples of four types of passive samplers[110-113]

Category	General Sampling Rate	Examples
Tube sampler	Very low	ORSA 5 organic vapor samplers from Dräger
Permeation sampler	Low	Waterloo Membrane Sampler from SiREM
Badge sampler	Medium	Organic Vapor Monitor 3500 from 3M
Radial sampler	High	Radiello Sampler from Fondazione Salvatore Maugeri

The advantages of the passive samplers include pumpless sampling, supporting long-term (days to weeks) sampling, reliable deployment with little required training, and low price. However, their use generally requires submission of exposed samplers to the laboratory, standard solvent or thermal extraction, and (typically) GC analysis, which raises the cost per sample and delays results from being obtained.

1.6.1.4 Passive Microfabricated Preconcentrators

Based on the passive sampling theory discussed above, the effective sampling rate of a passive sampler can be expressed in terms of readily accessible variables, i.e. the diffusion coefficient of the VOC in air (D), and the cross sectional area (A) and the diffusion path length (L) of the sampler. If the ratio of A to the L is held constant, the sampler can be scaled down and its sampling rate will remain constant, assuming that the (reduced) adsorbent mass has sufficient capacity.[114] MEMS techniques offer a path to miniaturize A and L and to integrate heaters to permit thermal desorption of captured VOCs and unlimited re-use of the device.

The Zellers and Kurabayashi groups jointly developed a device, called the microfabricated passive preconcentrator/injector (μPPI), which was designed to be an integral component of a μGC system, and characterized the passive sampling and thermal desorption performance of the device.[114] Photographs of their μPPI are shown in Figure 1.12. The two-layer device had a top layer of Si having a grid of 1530 microfabricated parallel diffusion apertures (area = 54 × 54 μm; length = 200 μm) through which vapors would diffuse at a known rate; a bottom layer of Si having an etched cavity (3.2 × 2.4 × 0.25 mm) packed with 750 μg of granular carbon adsorbent (Carbopack X); and an integrated Ti/Pt microheater for heating the capacity to 300 °C for thermal desorption.

The μPPI device exhibited a passive diffusional sampling rate of ~9 mL/min for toluene and was thermally cycled 2000 times from 25 to 300 °C with no evidence of a decline in device health. However, the design of the μPPI device suffered from sample loss back through the inlet grid during thermal desorption unless an extremely high flow rate (> 50 mL/min) was applied. This desorption flow rate is sub-optimal for μGC columns and pumps. In addition, the μPPI device had a limited effective capacity above which the sampling rate started to gradually decline. More

specifically, the sampling rate began to decline after only 30 min (i.e., above 1 µg of accumulated toluene mass at 1 ppm).

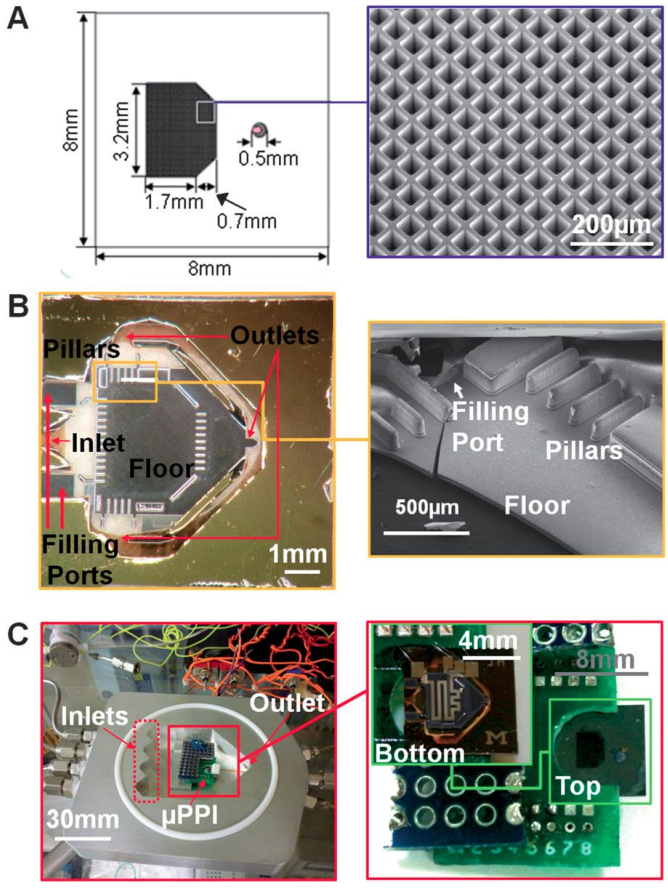

Figure 1.12 (a) dimensional diagram of µPPI (left-hand) and SEM image of µPPI grid structure (right-hand); (b) photographs of µPPI bottom layer (left-hand) and SEM image of µPPI bottom layer near one filling port (right-hand); (c) µPPI in the exposure chamber (left- hand) and µPPI mounted on the carrier PCB (right-hand).[114]

In another study, the µPPI device was further characterized in a custom GC system comprising a µPPI, a separation column and two on-column Fabry-Pe´rot (FP) cavity sensors at both ends of the column.[115] The µPPI device was tested with four compounds (benzene, TCE, toluene, and m-xylene) which spanning one decade in vapor pressure. Experimental sampling rates of the four compounds measured in the individual compound tests were 3% to 15% lower than the theoretical rates. Sampling rates of the four compounds can remain constant over up to ~45 min

beyond which the sampling rates started to decrease. Injection profiles of the μPPI desorption processes were measured by the on-column detector. The results exhibited that the peak got sharper with the increasing the heating rates from 60 °C/s to 90 °C/s. Additionally, the μPPI device was characterized with a mixture of the four compounds. Obvious competitive adsorptions occurred in the mixture tests, which hindered the quantification of compositions of the mixture, thereby impeding the use of μPPI in the real-world situations.

1.6.2 Microfabricated Columns

Gas chromatography is a technique used to separate and analyze components of a mixture that can be vaporized without decomposition. The separation depends on the differences in interactions between analytes and the stationary phase.[116] As such it is one of the most important parts of a GC instrument. There are various stationary phases, e.g. dimethyl polysiloxane, trifluoropropylmethyl polysiloxane, and polyethylene glycol,[117] and selecting the right stationary phase is application specific. GC columns can be classified into two categories, packed column and open tubular column. The latter is commonly used nowadays due to its efficient and fast separation while the former is rarely used in modern applications.[116] Thus, we will not discuss the packed column in this dissertation.

Various models have been developed to describe the separation, including plate model, Van Deemter equation, and Golay equation.[118,119] The plate model assumes that the GC column contains a large quantity of separate layers, i.e. theoretical plates. At each plate, equilibrium is reached between the stationary phase and mobile phase, i.e. carrier gas. By the transfer of the (typically pressurized) mobile phase among the plates, analytes move through the column. Although these plates do not actually exist, they serve as an imaginary picture that helps us understand the processes in the column. They provide a way of evaluating the column efficiency

by either estimating the number of theoretical plates (N) in a column of a given length (L), or the height equivalent to a theoretical plate (H). These quantities can be defined as follows:

$$N = 5.545(\frac{t_R}{fwhm})^2 \quad \text{Eq. 1.11}$$

$$H = \frac{L}{N} \quad \text{Eq. 1.12}$$

where t_R is the retention time (the time between sample injection and analyte peak elution at the end of the column), and *fwhm* is full width at half maximum of a peak for the analyte chosen for evaluating *N*.

The t_R in Eq. 1.11 includes the mobile phase hold-up time (t_M) which is not related to the separation process. Thus, the t_R can be adjusted by subtracting t_M from it. The adjusted retention time (t_R'), plate number (N'), and plate height (H') can be expressed by the following equations:

$$t_R' = t_R - t_M \quad \text{Eq. 1.13}$$

$$N' = 5.545(\frac{t_{R'}}{fwhm})^2 \quad \text{Eq. 1.14}$$

$$H' = \frac{L}{N'} \quad \text{Eq. 1.15}$$

One primary limitation of the plate theory is that the model assumes the time taken to reach the equilibrium between stationary and mobile phases is infinitely short. By virtue of considering the time required to reach equilibrium, the Van Deemter equation can explain how the peak broadening is affected by the rate of elution.[119,120] The equation relates the H of a column to the linear mobile phase velocity and factors causing the peak broadening, as follows:

$$H = A + \frac{B}{u} + Cu \quad \text{Eq. 1.16}$$

where *A* is eddy-diffusion parameter, *B* is the analyte diffusion coefficient in the mobile phase in the longitudinal direction, *C* is a coefficient representing the resistance to mass transfer in both the stationary phase and the mobile phase, and *u* is the linear mobile phase velocity. The A term relates to the band broadening caused by random diffusion paths of the analyte in a packed column. The A term is not considered significant in wall-coated capillary columns. The B term describes the band broadening related to longitudinal diffusion. The effects of longitudinal diffusion decrease with increasing mobile phase velocity because less time is spent on the column. The C term relates to the rates of mass transfer between the mobile phase and the stationary phase, and the corresponding band broadening is due to different velocities of analyte molecules in the mobile phase and stationary phase.

With removal of the term A and some simple assumptions, the Golay equation is developed as follows:[39]

$$H = \frac{B}{u} + C_s u + C_m u + D u^2 \qquad \text{Eq. 1.17}$$

$$B = 2 D_m f_1 f_2 \qquad \text{Eq. 1.18}$$

$$C_s = \frac{2 k d_f^2}{3(k+1) D_s} \qquad \text{Eq. 1.19}$$

$$C_m = \frac{(1+6k+11k^2) r^2 f_1}{24(k+1)^2 D_m f_2} \qquad \text{Eq. 1.20}$$

$$D = \frac{\Delta t^2}{L(k+1)^2} \qquad \text{Eq. 1.21}$$

where *H*, *B*, and *u* have the same definitions as the Van Deemter equation, C_s is the mass transfer resistance coefficient for the stationary phase, C_m is the mass transfer resistance coefficient for the mobile phase, *D* is a coefficient relating to the peak broadening outside the column such as GC

injection and detection parts, D_m is the analyte diffusion coefficient in the mobile phase, D_s is the analyte diffusion coefficient in the stationary phase, f_1 is the Martin-James gas compression coefficient, f_2 is the Golay-Gidding gas compression coefficient, k is the capacity factor, d_f is the stationary phase film thickness, r is the column inner radius, Δt is the instrument dead time, and L is the column length.

The Golay model can provide insight into the selection of experimental operating conditions. Figure 1.13 shows typical Golay curves that depict the influence of carrier gas linear velocity on the column efficiency for three commonly used carrier gases (N_2, He, and H_2).[117] The figure demonstrates that He has the highest column efficiency when linear velocity is at ~25 cm/s. As linear velocity increases, the column efficiency of He decreases. This results from the effect of mass transfer term on the column performance. When the velocity is on the far right side of the plot, e.g. 50 cm/s, H_2 becomes optimum in terms of column efficiency. In addition, the column efficiency of He decreases as the linear velocity decreases, which is due to the influence of the longitudinal diffusion term on the column efficiency. When the velocity is on the far left side of the plot, e.g. 10 cm/s, N_2 has the highest column efficiency.

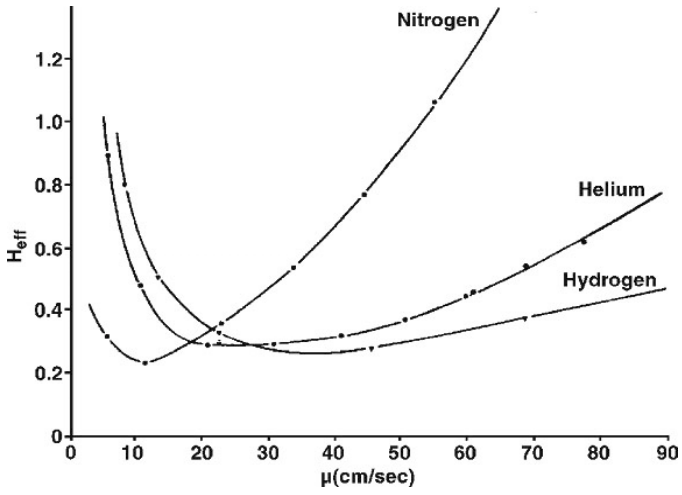

Figure 1.13 Typical Golay curves for three commonly used carrier gases (N_2, He, and H_2).[117]

Microfabricated columns (μcolumn) have been widely studied and developed for μGC systems. A typical fabrication process flow of μcolumns mainly includes: (1) deep reactive ion etching (DRIE) of a Si substrate, which creates a fluidic channel; (2) sealing the etched Si substrate with a glass substrate; (3) deposition of heaters and temperature sensors on the back side of the Si substrate.[121] After microfabrication, the fluidic channel is coated with a polymeric stationary phase such as PDMS, which can be cross-linked in situ to help stabilize it. Due to the anisotropic characteristic of DRIE process, the μcolumns usually have rectangular or square cross-section. These columns have slightly different performance than the traditional columns with round channels. Theoretically, the C_m term in the Golay equation needs to be adjusted for the change in column channel shape. The corresponding theoretical problem has been studied by Spangler, Giddings, and Ahn.[122,123] Although μcolumns with round or semi-circular channels have been developed, they are less common.[76,124-128]

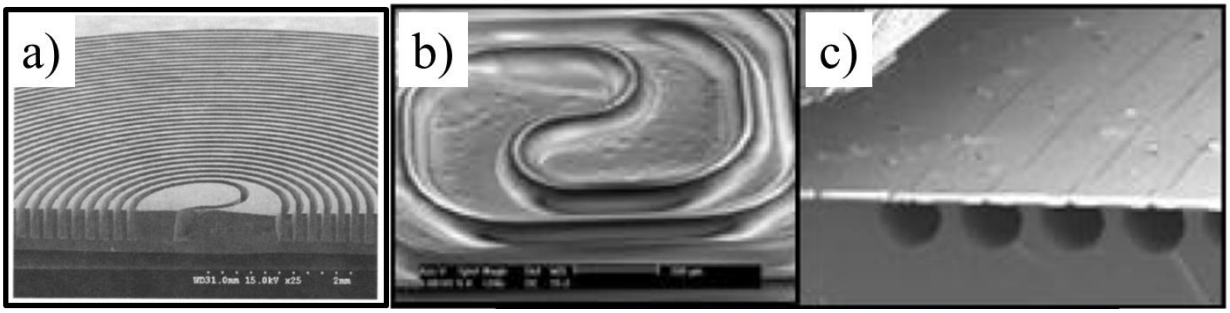

Figure 1.14 (a) SEM image of a μcolumn on basis of anisotropic etching in ref. 129; (b) (c) SEM images of a μcolumn on basis of isotropic etching in ref. 124.

1.6.3 Microfabricated Sensors

1.6.3.1 Microsensors for VOC Detection

With the development of MEMS techniques, various microfabricated sensors (μsensor) have been created for VOC analysis. A typical VOC μsensor is composed of two parts: an interface

layer, which interacts VOCs reversibly, and a transducer, which converts the interaction to an electronic or photonic output signal. The schematic diagram of a generic VOC sensor is shown in Figure 1.15. Various transduction mechanisms have been used for the development of μsensors such as resistors, capacitors, mechanical and optical resonators.[130-139] Different transduction mechanisms probe different features of VOC-interface interaction that include charge carrier density, mass, dielectric constant, viscoelasticity, and refractive index. Figure 1.16 depicts the basic designs and operations of multiple sensors including

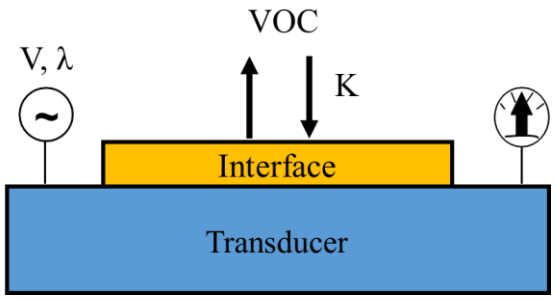

Figure 1.15 Schematic diagram of a VOC μsensor

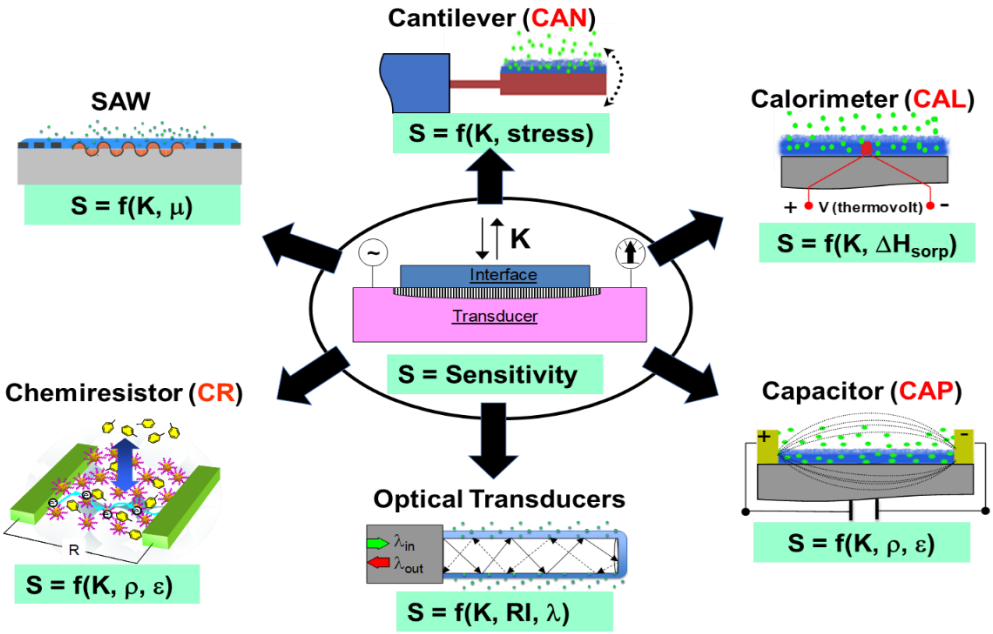

Figure 1.16 Schematic diagram depicting the basic designs and operations of multiple sensors.[140]

Analysis of VOC mixtures requires the integration of the μsensor into the μGC systems. The key performance metrics of a μsensor in a μGC system include sensitivity to various VOCs, response time, power demand, stability, and compatibility with proper flow rates required by efficient separation (0.5-3 mL/min). A small set of μsensors have been demonstrated as μGC detectors such as microfabricated nanoparticle chemiresistors (μCR), μOFRR, microfabricated thermal conductivity detectors (μTCD), and metal-oxide (MOX) semiconductors.[78,79,123,128,138,139,141]

Various interface layers used in VOC μsensors include but are not limited to polymers, nanoparticles, nanowires, and ionic liquids.[136,150] The interface layer of a μsensor interacts with VOCs through a reversible sorption-desorption process. The magnitude of the output signal is related to the quantity of VOC molecules that are absorbed or adsorbed by the interface layer. The definition of the partition coefficient (*K*) is the ratio of the analyte concentration in the interface layer to that in the gaseous phase at equilibrium. *K* is a measures of the equilibrium vapor-interface solubility at a given temperature which can be expressed as follows:

$$K = \frac{C_c}{C_v} \qquad \text{Eq. 1.22}$$

where C_c is the concentration of the (condensed) VOC in the interface layer, and C_v is the air concentration of the VOC.

For a polymeric interface layer, the K can be described as follows:

$$K = \frac{\rho RT}{\gamma M p_v} \qquad \text{Eq. 1.23}$$

where ρ is the density of the polymer, R is the ideal gas constant, T is the temperature, γ is the VOC activity coefficient (for ideal solutions $\gamma = 1$), M is the molecular weight of the polymer, p_v is the

saturated vapor pressure of the VOC.[151] Ideally, the *K* value is inversely proportional to the saturated vapor pressure of the VOC. Thus, low-volatility compounds will generally give larger μsensor responses than high-volatility compounds at the same air concentration, all other thing being equal.

1.6.3.2 Single Transducer (ST) Arrays

Transducer arrays comprising multiple sensors are frequently employed to achieve a diversity of responses and thereby to enhance the selectivity of VOC mixture analyses by virtue of their capability of generating several independent output signals.[152-156] A single transducer array is typically composed of several transducers which have the same transduction principle but use different interface materials. Examples of ST arrays include chemiresistor sensor arrays with multiple monolayer protected gold nanoparticle (MPN) films and mechanical resonator sensor arrays using different polymer coatings.[131,136,156,157] It was reported that ST arrays were capable of differentiating many individual VOC from each other.[158-160] However, ST arrays can only discriminate a limited number of binary VOC mixtures and generally cannot determine the components of the ternary and more complex VOC mixtures, which can be attributed to the limited range of vapor partitioning and limited diversity of properties measured in ST arrays.[152,161,162]

The concept that more sensors can yield greater diversity and achieve the analysis of more complex mixtures[85,86] is specious. It was reported that that increasing the number of sensors in ST arrays beyond ~4-6 sensors did not improve VOC recognition, regardless of the transduction mechanism or interface layers used.[86,156,163]

1.6.3.3 Multi-Transducer (MT) and Multi-Variable (MV) Arrays

A multi-transducer (MT) array comprises several sensors with different transduction principles. It therefor makes sense that using different transduction mechanisms among the sensors in an array should enhance the diversity of the responses by virtue of probing more physical properties, and thereby improve the recognition and differentiation of VOC mixtures components. Although the idea was proposed >20 years ago, the systematic study of MT arrays has been limited.[153,163] Göpel et al. developed various MT arrays using different transduction mechanisms which probed interface layer changes in a range of physical properties such as resistance, temperature, mass, and dielectric constant.[154,156,164,165] Jin et al. reported that a MT transducer array assembled from judiciously chosen subsets of 15 polymer-coated sensors, i.e. 5 cantilevers, 5 capacitors and 5 calorimeters. The study exhibited the optimal MT arrays provided measurable improvements over the optimal ST arrays. MT arrays consisting of 5 sensors can discriminate one-third of 165 ternary VOC mixtures from the corresponding individual compounds and binary-compound mixtures. However, the MT arrays can not analyze any of 330 quaternary VOC mixtures.[152]

For the same purpose of enhancing discrimination, a relatively new concept called multi-variable (MV) sensing was proposed.[166-168] An MV sensor is a single sensor that can yield partially uncorrelated responses in different operation modes. An array of MV sensors could have potential advantages over ST and MT arrays, including fewer noise sources, and easier coating and packaging. One example of an MV array include the polymer-coated impedance-based sensor RFID antenna array reported by Potyrailo et al.[166], which simultaneously measures changes in capacitance and resistance arising from vapor sorption into the polymer film. They also incorporated an RFID antenna for remote interrogation. Another, earlier, example is a surface

acoustic wave sensor driven in multiple resonant modes that detects changes in elastic coefficients and mass loading.[167] Another study showed that a single optical MV sensor that exploited changes in the localized surface plasmon resonance (LSPR) of a nanoparticle film could differentiate several individual VOCs and some simple VOC mixtures.[168]

1.6.3.4 LSPR

LSPR is the result of interaction between incident light and the collective oscillation of free electrons in noble metal nanostructures.[169] Figure 1.17 illustrates the basic mechanism of LSPR. It has two important effects: 1) the electric field around the surface of the nanostructures will be significantly enhanced; 2) the optical extinction will reach the maximum when the incident light is at the resonance frequency of nanostructures.[169,170] This extinction peak wavelength is affected by size, shape and the composition of the nanostructures, as well as the refractive index of the surrounding environment.[171] The sorption of VOCs into a film of the nanostructured material can change the refractive index of surrounding medium, and thereby can change the extinction peak wavelength. Thus, VOC sensing can be achieved on the basis of measuring the change of extinction peak wavelength.[172-176] However, the sensing devices in most studies had low sensitivity.

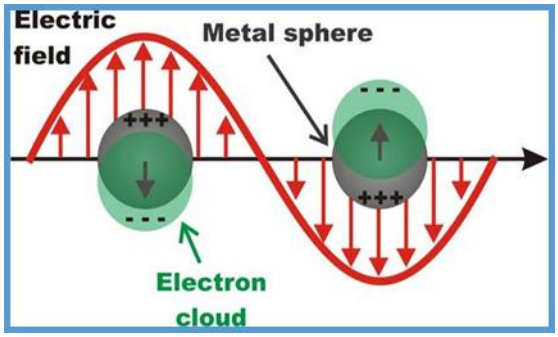

Figure 1.17 Schematic diagram illustrating the mechanism of LSPR.[177]

1.6.3.5 Chemometrics

Chemometrics is the chemical discipline that uses mathematical and statistical methods to extract information from chemical systems. For microsensor arrays, chemometrics generally entails multivariate statistical methods to evaluate the collective responses from the sensors in the array and assess the degree to which the patterns of responses can be used to recognize and differentiate one vapor from another. Two broad classifications of such methods are supervised learning methods and unsupervised learning methods. In supervised learning methods, the signal generated by each sensor in an array is combined to create a response vector. Each vector has a "label" indicating the type of a VOC or the composition of a mixture, as determined by calibration. These methods are often used to build pattern classification models for identification of different VOCs. Building a typical pattern classification model mainly includes three steps: (1) data preprocessing to convert the raw signal data generated from the array to the cleaned data vectors as the model input; (2) data extraction to transform the input data to new salient features; and (3) classification model training to define the relevant parameters of the model. Examples of pattern classification models used for VOC identification include extended disjoint principal component regression (EDPCR),[178] k–nearest neighbor (KNN), and linear discriminant analysis (LDA).[179] Some studies compared the identification performance of different models.[180-185] The results of these studies suggest that there is no single model that can always provide the best fit for all VOC identification problems. In other words, one best-fit model for one VOC identification/differentiation problem might not still provide the best fit for another problem in which there are different target analytes or a different sensor array system. Model selection techniques have been used in some studies to help select a model from a set of candidate models.[182,185]

In unsupervised learning methods, unlike supervised learning methods, composite signals from an array are not labeled. The unsupervised learning methods are often used in exploratory analyses of sensor array data.[186] Some unsupervised learning methods, e.g. k-means, are used in clustering analysis of sensor array data, but the report of this is less common. Another commonly used unsupervised learning method is principal component analysis (PCA). Signal data generated by sensor arrays are generally in a high-dimensional data space. Using PCA, the dimensionality of the data can be reduced to a few orthogonal dimensions in a way that can best explain the variance of the data. The PCA also provides an easy way to visualize the data originally in a high-dimensional space.[187,188] An example of PCA implementation with data generated by an μCR sensor array of a μGC system is shown in Figure 1.18.

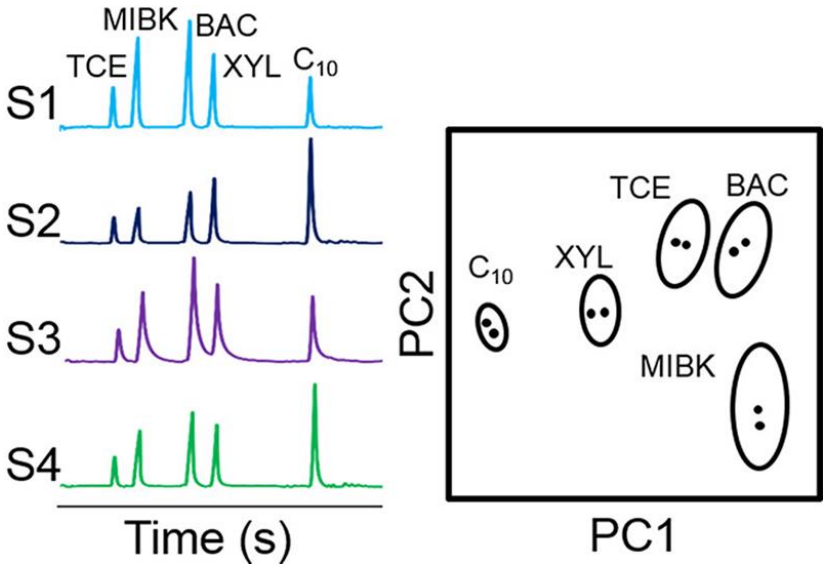

Figure 1.18 A PCA analysis implemented with data generated by an array of 4 μCR sensors in a μGC system[188]

1.6.3.6 Microfabricated Optofluidic Ring Resonator (μOFRR)

The optofluidic ring resonator (OFRR) is an optical sensor that combines vapor sensing and fluidic transport functions.[85,189] The first configuration was a fused silica or glass capillary

with a thinned wall. So-called whispering gallery modes (WGM) can be formed in capillary wall by touching it with a tapered optical fiber carrying light from a remote source. The evanescent component of the circulating WGM optical signal can probe the interior surface of the capillary. A resonant wavelength (λ_{WGM}) can be detected by scanning the wavelength of a tunable diode-laser and monitoring the output optical intensity. The value of λ_{WGM} is governed by the following equation for a circumferential WGM:

$$\lambda_{WGM} = \frac{2\pi r n_{eff}}{m} \qquad \text{Eq. 1.24}$$

where r is the resonator radius, n_{eff} is the effective waveguide refractive index, and m is an integer.

When the sensing interface material coated on the inner wall of the OFRR interacts with VOC molecules, the refractive index and thickness of the film will change, and thereby a WGM spectral shift will be generated.[190] The shift serves as a sensor response. The sensing concept is shown in Figure 1.19.

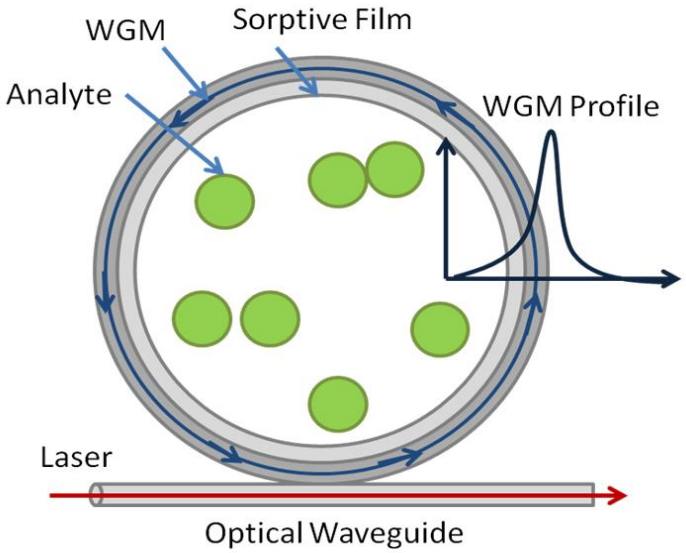

Figure 1.19 The schematic diagram depicting the operation mechanism of OFRR sensing[189]

Drawn-capillary OFRRs have been reported as GC detectors.[191] However, the OFRRs reported were fragile and had high variance in wall thickness and length among devices. In addition, they can hardly be integrated in microsystems, which hinders their use in on-site analysis. μOFRR sensors are suitable for integration in μGC systems by virtue of MEMS techniques. Scholten et al. reported two μOFRR sensors coated with PDMS and 1-mercapto-(triethylene glycol) methyl ether (TEG) functionalized MPNs respectively, and characterized their performance as the detectors in conventional bench-top GC and μGC systems.[138,139]

Recently some research groups reported that the plasmonic nanomaterials can significantly enhance the sensitivity of WGM sensing by virtue of the local electric field enhancement near the nanomaterial surface.[192-194] The responses of these sensors are affected by both of WGM sensing characteristics and plasmonic characteristics of nanomaterials, and thereby will be dependent on the partition coefficient, air concentration, electric field enhancement factor and refractive index of each VOC. Both electric field enhancement factor and refractive index are associated with the wavelength of probing light. When probed at different wavelengths, the sensor would have different relationships between sensor responses and air concentrations of analytes. Thus, response patterns can be expected, and thereby achieving the VOC recognition.

1.7 Significance of This Research

The work described in Chapter 2 concerns the μOFRR sensor, using plasmonic nanomaterial interface layers for VOC analysis. Qualitative tests were performed with a PDMS-coated μOFRR, a MPN-coated μOFRR, and a functionalized Au nanorod coated μOFRR. The results showed that all the μOFRR devices can provide rapid and reversible response to VOCs. Implementation of the MPN-coated μOFRR as a detector for a conventional GC yielded low-ng

level detection limits, which was consistent with previously reported results. This indicates that the fabrication, coating, and system integration techniques we have developed are reliable.

The study described in Chapter 3 concerns a new microfabricated passive preconcentrator for μGC systems, i.e. the μPP device. This device combining with a microfabricated progressively heated injector (μPHI), would produce an integrated microscale collector-injector (μCOIN), which serves as a collector module for a μGC system for autonomously measuring S/VOC mixture analysis. The μPP device achieved the collections of mixtures of S/VOCs spanning a wide structure and volatility range by passive diffusion with zero expended power throughout the sampling cycle. Using dual adsorbents and optimizing designs of the device and heaters, the μPP outperformed the previous μPPI device with respect to sampling rate and duration, desorption efficiency and flow rate, energy efficiency, fabrication simplicity, and the range of compounds and mixtures for which quantitative capture and desorption are possible.

1.8 References

1. ScienceDirect, https://www.sciencedirect.com/topics/medicine-and-dentistry/volatile-organic-compound, (accessed October 2019).
2. United States Environmental Protection Agency, https://www.epa.gov/indoor-air-quality-iaq/technical-overview-volatile-organic-compounds, (accessed October 2019).
3. S. Cakmak, R. E. Dales, L. Liu, L. M. Kauri, C. L. Lemieux, C. Hebbern and J. Zhu, Residential exposure to volatile organic compounds and lung function: results from a population-based cross-sectional survey, *Environmental pollution*, 2014, **194**, 145-151.
4. K. Rumchev, H. Brown and J. Spickett, Volatile organic compounds: do they present a risk to our health?, *Reviews on environmental health*, 2007, **22**, 39-56.
5. P. J. Villeneuve, M. Jerrett, D. Brenner, J. Su, H. Chen and J. R. McLaughlin, A case-control study of long-term exposure to ambient volatile organic compounds and lung cancer in Toronto, Ontario, Canada, *American journal of epidemiology*, 2013, **179**, 443-451.
6. S. O. Hansson, *Setting the limit: occupational health standards and the limits of science*, Oxford University Press, USA, 1998.
7. A. C. o. G. I. Hygienists, *Documentation of the Threshold Limit Values and Biological Exposure Indices*, American Conference of Governmental Industrial Hygienists, USA, 2001.
8. S. M. Rappaport and L. L. Kupper, *Quantitative exposure assessment*, Stephen Rappaport, USA, 2008.
9. W. H. Bullock and J. S. Ignacio, *A strategy for assessing and managing occupational exposures*, AIHA, USA, 2006.
10. C. Lourenço and C. Turner, Breath analysis in disease diagnosis: methodological considerations and applications, *Metabolites*, 2014, **4**, 465-498.
11. C. S. Probert, T. Khalid, I. Ahmed, E. Johnson, S. Smith and N. M. Ratcliffe, Volatile organic compounds as diagnostic biomarkers in gastrointestinal and liver diseases, *Journal of Gastrointestinal and Liver Disease*, 2009, **18**, 337-343.
12. L. Mølhave, G. Clausen, B. Berglund, J. De Ceaurriz, A. Kettrup, T. Lindvall, M. Maroni, A. Pickering, U. Risse and H. Rothweiler, Total volatile organic compounds (TVOC) in indoor air quality investigations, *Indoor Air*, 1997, **7**, 225-240.
13. G. Serrano, T. Sukaew and E. T. Zellers, Hybrid preconcentrator/focuser module for determinations of explosive marker compounds with a micro-scale gas chromatograph, *Journal of Chromatography A*, 2013, **1279**, 76-85.

14. O. Suzuki, H. Seno, K. Watanabe-Suzuki and A. Ishii, Situations of poisoning and analytical toxicology in Japan, *Forensic science international*, 2000, **113**, 331-338.

15. D. Matatagui, J. Martí, M. Fernández, J. Fontecha, J. Gutiérrez, I. Gràcia, C. Cané and M. Horrillo, Chemical warfare agents simulants detection with an optimized SAW sensor array, *Sensors and Actuators B: Chemical*, 2011, **154**, 199-205.

16. N. Kostesha, T. S. Alstrøm, C. Johnsen, K. Nilesen, J. Jeppesen, J. Larsen, M. H. Jakobsen and A. Boisen, Advanced environmental, chemical, and biological sensing technologies VII, USA, April, 2010.

17. S. Giannoukos, A. Agapiou and S. Taylor, Advances in chemical sensing technologies for VOCs in breath for security/threat assessment, illicit drug detection, and human trafficking activity, *Journal of breath research*, 2018, **12**, 027106.

18. P. Guerra-Diaz, S. Gura and J. R. Almirall, Dynamic planar solid phase microextraction− ion mobility spectrometry for rapid field air sampling and analysis of illicit drugs and explosives, *Analytical chemistry*, 2010, **82**, 2826-2835.

19. T. Karl, T. J. Christian, R. J. Yokelson, P. Artaxo, W. M. Hao and A. Guenther, The Tropical Forest and Fire Emissions Experiment: method evaluation of volatile organic compound emissions measured by PTR-MS, FTIR, and GC from tropical biomass burning, *Atmospheric Chemistry and Physics*, 2007, **7**, 5883-5897.

20. World Health Organization, http://www.euro.who.int/__data/assets/pdf_file/0009/128169/e94535.pdf, (accessed October 2019).

21. Tox Town, https://toxtown.nlm.nih.gov/chemicals-and-contaminants/volatile-organic-compounds-vocs, (accessed October 2019).

22. Occupational Safety and Health Administration, https://www.osha.gov/dsg/annotated-pels/tablez-1.html, (accessed October 2019).

23. ACGIH, https://www.acgih.org/tlv-bei-guidelines/tlv-chemical-substances-introduction, (accessed October 2019).

24. The National Institute for Occupational Safety and Health (NIOSH), https://www.cdc.gov/niosh/npg/, (accessed October 2019).

25. J. L. Perkins, *Modern industrial hygiene*, ACGIH, USA, 2008.

26. D. H. Anna, *The occupational environment: its evaluation, control and management*, American Industrial Hygiene Association, USA, 2011.

27. TOXNET, https://toxnet.nlm.nih.gov/cgi-bin/sis/htmlgen?HSDB, (accessed November 2019).

28. DHS, https://www.dhs.gov/xlibrary/assets/prep_chemical_fact_sheet.pdf, (accessed November 2019).

29. K. Ganesan, S. Raza and R. Vijayaraghavan, Chemical warfare agents, *Journal of pharmacy and bioallied sciences*, 2010, **2**, 166.

30. The National Institute for Occupational Safety and Health (NIOSH), http://www.cdc.gov/niosh/docs/2003-154/, (accessed October 2019).

31. Occupational Safety and Health Administration, https://www.osha.gov/dts/sltc/methods/, (accessed October 2019).

32. Index to EPA Test Methods, https://www.epa.gov/sites/production/files/2015-03/documents/testmeth.pdf, (accessed October 2019).

33. SUPELCO, https://www.sigmaaldrich.com/content/dam/sigma-aldrich/docs/Supelco/General_Information/1/04_Selecting%20the%20most%20suitable%20adsorbent%20for%20Air%20Monitoring.pdf, (accessed November 2019).

34. SUPELCO, http://academy.webvent.tv/uploads/assets/1240/document/ChoosingtheRightAdsorbentforyourThermalDesorptionGasChromatographyApplications.pdf, (accessed November 2019).

35. SUPELCO, https://www.sigmaaldrich.com/content/dam/sigma-aldrich/docs/Supelco/General_Information/t402025.pdf, (accessed November 2019).

36. Ö. O. Kuntasal, D. Karman, D. Wang, S. G. Tuncel and G. Tuncel, Determination of volatile organic compounds in different microenvironments by multibed adsorption and short-path thermal desorption followed by gas chromatographic–mass spectrometric analysis, *Journal of Chromatography A*, 2005, **1099**, 43-54.

37. E. J. Staples and S. Viswanathan, Detection of contrabands in cargo containers using a high-speed gas chromatograph with surface acoustic wave sensor, *Industrial & Engineering Chemistry Research*, 2008, **47**, 8361-8367.

38. J. M. Sanchez and R. D. Sacks, GC analysis of human breath with a series-coupled column ensemble and a multibed sorption trap, *Analytical chemistry*, 2003, **75**, 2231-2236.

39. R. L. Grob and E. F. Barry, *Modern Practice of Gas Chromatography*, Wiley, USA, 2004.

40. My Scientific Blog, http://upendrats.blogspot.com/2013/06/gas-chromatography.html, (accessed October 2019).

41. S. Mokhatab, W. A. Poe and J. Y. Mak, *Handbook of Natural Gas Transmission and Processing: Principles and Practices*, Elsevier Science, UK, 2015.

42. H. Huang, F. Haghighat and P. Blondeau, Volatile organic compound (VOC) adsorption on material: influence of gas phase concentration, relative humidity and VOC type, *Indoor Air*, 2006, **16**, 236-247.

43. K. Y. Foo and B. H. Hameed, Insights into the modeling of adsorption isotherm systems, *Chemical engineering journal*, 2010, **156**, 2-10.

44. G. O. Wood, Activated carbon adsorption capacities for vapors, *Carbon*, 1992, **30**, 593-599.

45. G. O. Wood and J. Stampfer, Adsorption rate coefficients for gases and vapors on activated carbons, *Carbon*, 1993, **31**, 195-200.

46. Y.-C. Chiang, P.-C. Chiang and E.-E. Chang, Effects of surface characteristics of activated carbons on VOC adsorption, *Journal of environmental engineering*, 2001, **127**, 54-62.

47. Y.-C. Chiang, P.-C. Chiang and C.-P. Huang, Effects of pore structure and temperature on VOC adsorption on activated carbon, *Carbon*, 2001, **39**, 523-534.

48. C. Chuang, P. Chiang and E. Chang, Modeling VOCs adsorption onto activated carbon, *Chemosphere*, 2003, **53**, 17-27.

49. K.-J. Kim, C.-S. Kang, Y.-J. You, M.-C. Chung, M.-W. Woo, W.-J. Jeong, N.-C. Park and H.-G. Ahn, Adsorption–desorption characteristics of VOCs over impregnated activated carbons, *Catalysis Today*, 2006, **111**, 223-228.

50. M. Lillo-Ródenas, A. Fletcher, K. Thomas, D. Cazorla-Amorós and A. Linares-Solano, Competitive adsorption of a benzene–toluene mixture on activated carbons at low concentration, *Carbon*, 2006, **44**, 1455-1463.

51. F. D. Yu, L. A. Luo and G. Grevillot, Adsorption isotherms of VOCs onto an activated carbon monolith: experimental measurement and correlation with different models, *Journal of Chemical & Engineering Data*, 2002, **47**, 467-473.

52. G. O. Wood and J. Stampfer, Adsorption rate coefficients for gases and vapors on activated carbons, *Carbon*, 1993, **31**, 195-200.

53. F.-Y. Yi, X.-D. Lin, S.-X. Chen and X.-Q. Wei, Adsorption of VOC on modified activated carbon fiber, *Journal of Porous Materials*, 2009, **16**, 521-526.

54. F. Qu, L. Zhu and K. Yang, Adsorption behaviors of volatile organic compounds (VOCs) on porous clay heterostructures (PCH), *Journal of Hazardous Materials*, 2009, **170**, 7-12.

55. C. M. Hussain, *Nanomaterials in Chromatography: Current Trends in Chromatographic Research Technology and Techniques*, Elsevier Science, Dutch, 2018.

56. D.C. Harris, *Quantitative Chemical Analysis*, W. H. Freeman, USA, 2007.

57. L. Spinelle, M. Gerboles, G. Kok, S. Persijn and T. Sauerwald, Review of portable and low-cost sensors for the ambient air monitoring of benzene and other volatile organic compounds, *Sensors*, 2017, **17**, 1520.

58. PHOTOVAC, https://products.inficon.com/getattachment.axd/?attaName=MicroFIDII-Brochure, (accessed October 2019).

59. Honeywell RAE Systems, https://www.raesystems.com/products/minirae-3000-wireless-handheld-voc-monitor, (accessed October 2019).

60. norlab, https://www.norlab.fi/library/brochure/10286, (accessed October 2019).

61. AIRSENSE ANALYTICS, https://airsense.com/en/products/portable-electronic-nose, (accessed October 2019).

62. J. Srivastava, P. Pandey, S. K. Jha, V. Mishra and R. Dwivedi, Chemical vapor identification by plasma treated thick film tin oxide gas sensor array and pattern recognition, *Sensors & Transducers*, 2011, **125**, 42.

63. A. Srivastava, Detection of volatile organic compounds (VOCs) using SnO2 gas-sensor array and artificial neural network, *Sensors and Actuators B: Chemical*, 2003, **96**, 24-37.

64. Defiant Technologies, www.defiant-tech.com, (accessed October 2019).

65. Electronic Sensor Technology, http://www.estcal.com, (accessed October 2019).

66. 908devices, https://908devices.com/products/mx908/, (accessed October 2019).

67. O. D. Sparkman, Mass spectrometry desk reference 2, *Journal of the American Society for Mass Spectrometry*, 2000, **12**, 1144.

68. INFICON, https://products.inficon.com/en-us/nav-products/product/detail/hapsite-er-identification-system/, (accessed October 2019).

69. FLIR, https://www.flir.com/products/griffin-g510/, (accessed October 2019).

70. PerkinElmer, https://www.perkinelmer.com/product/torion-t-9-portable-gc-ms-instrument-ntsst090500, (accessed October 2019).

71. Gasmet, https://www.gasmet.com/products/category/portable-gas-analyzers/dx4040/, (accessed October 2019).

72. J. Wang, J. Bryant-Genevier, N. Nuñovero, C. Zhang, B. Kraay, C. Zhan, K. Scholten, R. Nidetz, S. Buggaveeti and E. T. Zellers, Compact prototype microfabricated gas chromatographic analyzer for autonomous determinations of VOC mixtures at typical workplace concentrations, *Microsystems & Nanoengineering*, 2018, **4**, 17101.

73. M. Zhou, J. Lee, H. Zhu, R. Nidetz, K. Kurabayashi and X. Fan, A fully automated portable gas chromatography system for sensitive and rapid quantification of volatile organic compounds in water, *RSC Advances*, 2016, **6**, 49416-49424.

74. Y. Qin and Y. B. Gianchandani, A fully electronic microfabricated gas chromatograph with complementary capacitive detectors for indoor pollutants, *Microsystems & nanoengineering*, 2016, **2**, 15049.

75. A. Garg, M. Akbar, E. Vejerano, S. Narayanan, L. Nazhandali, L. C. Marr and M. Agah, Zebra GC: A mini gas chromatography system for trace-level determination of hazardous air pollutants, *Sensors and Actuators B: Chemical*, 2015, **212**, 145-154.

76. S. C. Terry, J. H. Jerman and J. B. Angell, A gas chromatographic air analyzer fabricated on a silicon wafer, *IEEE transactions on electron devices*, 1979, **26**, 1880-1886.

77. C.-J. Lu, W. H. Steinecker, W.-C. Tian, M. C. Oborny, J. M. Nichols, M. Agah, J. A. Potkay, H. K. Chan, J. Driscoll and R. D. Sacks, First-generation hybrid MEMS gas chromatograph, *Lab on a Chip*, 2005, **5**, 1123-1131.

78. W. R. Collin, G. Serrano, L. K. Wright, H. Chang, N. s. Nuñovero and E. T. Zellers, Microfabricated gas chromatograph for rapid, trace-level determinations of gas-phase explosive marker compounds, *Analytical chemistry*, 2013, **86**, 655-663.

79. S. K. Kim, H. Chang and E. T. Zellers, Microfabricated gas chromatograph for the selective determination of trichloroethylene vapor at sub-parts-per-billion concentrations in complex mixtures, *Analytical chemistry*, 2011, **83**, 7198-7206.

80. C.-J. Lu, J. Whiting, R. D. Sacks and E. T. Zellers, Portable gas chromatograph with tunable retention and sensor array detection for determination of complex vapor mixtures, *Analytical chemistry*, 2003, **75**, 1400-1409.

81. G. Serrano, H. Chang and E. Zellers, TRANSDUCERS 2009-2009 International Solid-State Sensors, Actuators and Microsystems Conference, USA, June, 2009.

82. Q. Zhong, W. H. Steinecker and E. T. Zellers, Characterization of a high-performance portable GC with a chemiresistor array detector, *Analyst*, 2009, **134**, 283-293.

83. J. Yeom, C. R. Field, B. Bae, R. I. Masel and M. A. Shannon, The design, fabrication and characterization of a silicon microheater for an integrated MEMS gas preconcentrator, *Journal of Micromechanics and Microengineering*, 2008, **18**, 125001.

84. B. Bae, J. Yeom, A. D. Radadia, R. I. Masel and M. A. Shannon, TRANSDUCERS 2007-2007 International Solid-State Sensors, Actuators and Microsystems Conference, France, June, 2007.

85. A. D. Radadia, R. I. Masel and M. A. Shannon, TRANSDUCERS 2007-2007 International Solid-State Sensors, Actuators and Microsystems Conference, France, June, 2007.

86. P. R. Lewis, P. Manginell, D. R. Adkins, R. J. Kottenstette, D. R. Wheeler, S. S. Sokolowski, D. E. Trudell, J. E. Byrnes, M. Okandan and J. M. Bauer, Recent advancements in the gas-phase MicroChemLab, *IEEE Sensors Journal*, 2006, **6**, 784-795.

87. G. C. Frye-Mason, R. J. Kottenstette, E. J. Heller, C. M. Matzke, S. A. Casalnuovo, P. R. Lewis, R. P. Manginell, W. K. Schubert, V. M. Hietala and R. J. Shul, Micro Total Analysis Systems' 98, Canada, October, 1998.

88. M. Akbar, M. Restaino and M. Agah, Chip-scale gas chromatography: From injection through detection, *Microsystems & Nanoengineering*, 2015, **1**, 15039.

89. Applied Sciences from TECHNOLOGY NETWORKS, https://www.technologynetworks.com/applied-sciences/product-news/apix-technology-introduces-industrys-first-gas-chromatography-device-215508, (accessed October 2019).

90. zebra ANALYTIX, https://zebraanalytix.com/technology/, (accessed October 2019).

91. Nanova Environmental, https://www.nanovaenv.com/novatest-p300/, (accessed October 2019).

92. K. Scholten, Microfabricated optofluidic ring resonators for sensitive, high-speed detection of volatile organic compounds, University of Michigan, 2015

93. T. Sukaew and E. T. Zellers, Evaluating the dynamic retention capacities of microfabricated vapor preconcentrators as a function of flow rate, *Sensors and Actuators B: Chemical*, 2013, **183**, 163-171.

94. W. A. Groves, E. T. Zellers and G. C. Frye, Analyzing organic vapors in exhaled breath using a surface acoustic wave sensor array with preconcentration: Selection and characterization of the preconcentrator adsorbent, *Analytica Chimica Acta*, 1998, **371**, 131-143.

95. C.-J. Lu and E. T. Zellers, A dual-adsorbent preconcentrator for a portable indoor-VOC microsensor system, *Analytical chemistry*, 2001, **73**, 3449-3457.

96. J. Bryant-Genevier and E. T. Zellers, Toward a microfabricated preconcentrator-focuser for a wearable micro-scale gas chromatograph, *Journal of Chromatography A*, 2015, **1422**, 299-309.

97. T. Sukaew, H. Chang, G. Serrano and E. T. Zellers, Multi-stage preconcentrator/focuser module designed to enable trace level determinations of trichloroethylene in indoor air with a microfabricated gas chromatograph, *Analyst*, 2011, **136**, 1664-1674.

98. M. M. McCartney, Y. Zrodnikov, A. G. Fung, M. K. LeVasseur, J. M. Pedersen, K. O. Zamuruyev, A. A. Aksenov, N. J. Kenyon and C. E. Davis, An easy to manufacture micro gas preconcentrator for chemical sensing applications, *ACS sensors*, 2017, **2**, 1167-1174.

99. Microfabricated Planar Preconcentrator, https://www.osti.gov/servlets/purl/753448, (accessed November 2019).

100. M. Martin, M. Crain, K. Walsh, R. A. McGill, E. Houser, J. Stepnowski, S. Stepnowski, H.-D. Wu and S. Ross, Microfabricated vapor preconcentrator for portable ion mobility spectroscopy, *Sensors and Actuators B: Chemical*, 2007, **126**, 447-454.

101. W.-C. Tian, H. K. Chan, C.-J. Lu, S. W. Pang and E. T. Zellers, Multiple-stage microfabricated preconcentrator-focuser for micro gas chromatography system, *Journal of Microelectromechanical systems*, 2005, **14**, 498-507.

102. M. Akbar, D. Wang, R. Goodman, A. Hoover, G. Rice, J. R. Heflin and M. Agah, Improved performance of micro-fabricated preconcentrators using silica nanoparticles as a surface template, *Journal of Chromatography A*, 2013, **1322**, 1-7.

103. B. Alfeeli, D. Cho, M. Ashraf-Khorassani, L. T. Taylor and M. Agah, MEMS-based multi-inlet/outlet preconcentrator coated by inkjet printing of polymer adsorbents, *Sensors and Actuators B: Chemical*, 2008, **133**, 24-32.

104. E. Camara, P. Breuil, D. Briand, L. Guillot, C. Pijolat and N. De Rooij, Micro gas preconcentrator in porous silicon filled with a carbon absorbent, *Sensors and Actuators B: Chemical*, 2010, **148**, 610-619.

105. C. Pijolat, M. Camara, J. Courbat, J.-P. Viricelle, D. Briand and N. F. de Rooij, Application of carbon nano-powders for a gas micro-preconcentrator, *Sensors and Actuators B: Chemical*, 2007, **127**, 179-185.

106. W. Tian, T. Wu, C.-J. Lu, W. Chen and H. Sheen, A novel micropreconcentrator employing a laminar flow patterned heater for micro gas chromatography, *Journal of Micromechanics and Microengineering*, 2012, **22**, 065014.

107. P. T. Scheepers, J. Konings, G. Demirel, E. O. Gaga, R. Anzion, P. G. Peer, T. Dogeroglu, S. Ornektekin and W. van Doorn, Determination of exposure to benzene, toluene and xylenes in Turkish primary school children by analysis of breath and by environmental passive sampling, *Science of the total environment*, 2010, **408**, 4863-4870.

108. P. Bohlin, K. C. Jones and B. Strandberg, Occupational and indoor air exposure to persistent organic pollutants: A review of passive sampling techniques and needs, *Journal of Environmental Monitoring*, 2007, **9**, 501-509.

109. EPA, https://clu-in.org/download/issues/vi/VI-passive-samplers-600-R-14-434.pdf, (accessed October 2019).

110. Kleinschmidt GmbH, https://www.kleinschmidtgmbh.com/Draeger-ORSA-5/en, (accessed November 2019).

111. SiREM, http://www.siremlab.com/waterloo-membrane-sampler-receives-regulatory-approval-in-israel/, (accessed November 2019).

112. 3M, https://www.3m.com/3M/en_US/company-us/all-3m-products/~/?N=5002385+3294770268+3294857497&rt=rud, (accessed November 2019).

113. MilliporeSigma, https://www.sigmaaldrich.com/catalog/product/supelco/rad1231?lang=en&region=US, (accessed November 2019).

114. J. H. Seo, S. K. Kim, E. T. Zellers and K. Kurabayashi, Microfabricated passive vapor preconcentrator/injector designed for microscale gas chromatography, *Lab on a Chip*, 2012, **12**, 717-724.

115. J. H. Seo, J. Liu, X. Fan and K. Kurabayashi, Fabry-Pérot cavity sensor-based optofluidic gas chromatography using a microfabricated passive preconcentrator/injector, *Lab on a Chip*, 2013, **13**, 851-859.

116. M. M. Rahman, A. Abd El-Aty, J. H. Choi, H. C. Shin, S. C. Shin and J. H. Shim, Basic overview on gas chromatography columns, *Analytical Separation Science*, 2015, **3**, 823-834.

117. Carrier Gas Selection for Capillary Gas Chromatography , https://www.sigmaaldrich.com/content/dam/sigma-aldrich/docs/Supelco/General_Information/1/t411126h.pdf, (accessed October 2019).

118. A. James, A. Martin and G. H. Smith, Gas-liquid partition chromatography: the separation and micro-estimation of ammonia and the methylamines, *Biochemical Journal*, 1952, **52**, 238.

119. K. Dettmer-Wilde and W. Engewald, *Practical gas chromatography*, Springer, USA, 2014.

120. J. Van Deemter, F. Zuiderweg and A. v. Klinkenberg, Longitudinal diffusion and resistance to mass transfer as causes of nonideality in chromatography, *Chemical Engineering Science*, 1956, **5**, 271-289.

121. A. Ghosh, C. R. Vilorio, A. R. Hawkins and M. L. Lee, Microchip gas chromatography columns, interfacing and performance, *Talanta*, 2018, **188**, 463-492.

122. Reidy, Shaelah M, High-Performance Micro-Fabricated Gas Chromatography Columns for Complex Mixture Analysis, University of Michigan, 2009

123. S. Zampolli, I. Elmi, F. Mancarella, P. Betti, E. Dalcanale, G. Cardinali and M. Severi, Real-time monitoring of sub-ppb concentrations of aromatic volatiles with a MEMS-enabled miniaturized gas-chromatograph, *Sensors and Actuators B: Chemical*, 2009, **141**, 322-328.

124. E. T. Zellers, S. Reidy, R. A. Veeneman, R. Gordenker, W. H. Steinecker, G. R. Lambertus, H. Kim, J. A. Potkay, M. P. Rowe and Q. Zhong, TRANSDUCERS 2007-2007 International Solid-State Sensors, Actuators and Microsystems Conference, France, June, 2007.

125. M. Agah, J. A. Potkay, J. A. Driscoll, R. D. Sacks, M. Kaviany and K. D. Wise, TRANSDUCERS 2003-12th International Conference on Solid-State Sensors, Actuators and Microsystems, Digest of Technical Papers, USA, June, 2003.

126. J. A. Potkay, G. R. Lambertus, R. D. Sacks and K. D. Wise, A low-power pressure- and temperature-programmable micro gas chromatography column, *Journal of Microelectromechanical Systems*, 2007, **16**, 1071-1079.

127. A. D. Radadia, R. D. Morgan, R. I. Masel and M. A. Shannon, Partially buried microcolumns for micro gas analyzers, *Analytical chemistry*, 2009, **81**, 3471-3477.

128. D. Cruz, J. Chang, S. Showalter, F. Gelbard, R. Manginell and M. Blain, Microfabricated thermal conductivity detector for the micro-ChemLab™, *Sensors and Actuators B: Chemical*, 2007, **121**, 414-422.

129. H.-s. Noh, P. J. Hesketh and G. C. Frye-Mason, Parylene gas chromatographic column for rapid thermal cycling, *Journal of microelectromechanical systems*, 2002, **11**, 718-725.

130. F. I. Bohrer, E. Covington, C. a. Kurdak and E. T. Zellers, Characterization of dense arrays of chemiresistor vapor sensors with submicrometer features and patterned nanoparticle interface layers, *Analytical chemistry*, 2011, **83**, 3687-3695.

131. Q.-Y. Cai and E. T. Zellers, Dual-chemiresistor GC detector employing monolayer-protected metal nanocluster interfaces, *Analytical chemistry*, 2002, **74**, 3533-3539.

132. M.-D. Hsieh and E. T. Zellers, Adaptation and evaluation of a personal electronic nose for selective multivapor analysis, *Journal of occupational and environmental hygiene*, 2004, **1**, 149-160.

133. R.-S. Jian, R.-X. Huang and C.-J. Lu, A micro GC detector array based on chemiresistors employing various surface functionalized monolayer-protected gold nanoparticles, *Talanta*, 2012, **88**, 160-167.

134. W. H. Steinecker, S. K. Kim, F. I. Bohrer, L. Farina, Ç. Kurdak and E. T. Zellers, Electron-beam patterned monolayer-protected gold nanoparticle interface layers on a chemiresistor vapor sensor array, *IEEE Sensors Journal*, 2010, **11**, 469-480.

135. J. W. Grate, Acoustic wave microsensor arrays for vapor sensing, *Chemical Reviews*, 2000, **100**, 2627-2648.

136. M. Li, E. Myers, H. Tang, S. Aldridge, H. McCaig, J. Whiting, R. Simonson, N. S. Lewis and M. Roukes, Nanoelectromechanical resonator arrays for ultrafast, gas-phase chromatographic chemical analysis, *Nano letters*, 2010, **10**, 3899-3903.

137. T. E. Mlsna, S. Cemalovic, M. Warburton, S. T. Hobson, D. A. Mlsna and S. V. Patel, Chemicapacitive microsensors for chemical warfare agent and toxic industrial chemical detection, *Sensors and Actuators B: Chemical*, 2006, **116**, 192-201.

138. K. Scholten, X. Fan and E. T. Zellers, A microfabricated optofluidic ring resonator for sensitive, high-speed detection of volatile organic compounds, *Lab on a Chip*, 2014, **14**, 3873-3880.

139. K. Scholten, W. Collin, X. Fan and E. Zellers, Nanoparticle-coated micro-optofluidic ring resonator as a detector for microscale gas chromatographic vapor analysis, *Nanoscale*, 2015, **7**, 9282-9289.

140. Ted Zellers, Junqi Wang, N. Nunovero, Z. Lin, J. Bryant, C. Zhan, W. Collin, K. Scholten, R. Nidetz, S. Buggaveeti, K. Kurabayashi, W. Steinecker, Microscale Gas Chromatography (μGC) with Microsensor Array Detection: Challenges and Prospects

141. R.-S. Jian, Y.-S. Huang, S.-L. Lai, L.-Y. Sung and C.-J. Lu, Compact instrumentation of a μ-GC for real time analysis of sub-ppb VOC mixtures, *Microchemical Journal*, 2013, **108**, 161-167.

142. K. Reddy, Y. Guo, J. Liu, W. Lee, M. K. K. Oo and X. Fan, On-chip Fabry–Pérot interferometric sensors for micro-gas chromatography detection, *Sensors and Actuators B: Chemical*, 2011, **159**, 60-65.

143. K. Reddy, Y. Guo, J. Liu, W. Lee, M. K. K. Oo and X. Fan, Rapid, sensitive, and multiplexed on-chip optical sensors for micro-gas chromatography, *Lab on a Chip*, 2012, **12**, 901-905.

144. J. Hatfield, P. Neaves, P. Hicks, K. Persaud and P. Travers, Towards an integrated electronic nose using conducting polymer sensors, *Sensors and Actuators B: Chemical*, 1994, **18**, 221-228.

145. M.-C. Tseng and Y.-H. Chu, Chemoselective gas sensing ionic liquids, *Chemical Communications*, 2010, **46**, 2983-2985.

146. F. Hernandez-Ramirez, J. D. Prades, R. Jimenez-Diaz, T. Fischer, A. Romano-Rodriguez, S. Mathur and J. R. Morante, On the role of individual metal oxide nanowires in the scaling down of chemical sensors, *Physical Chemistry Chemical Physics*, 2009, **11**, 7105-7110.

147. A. Kolmakov, Y. Zhang, G. Cheng and M. Moskovits, Detection of CO and O2 using tin oxide nanowire sensors, *Advanced materials*, 2003, **15**, 997-1000.

148. D. C. Meier, S. Semancik, B. Button, E. Strelcov and A. Kolmakov, Coupling nanowire chemiresistors with MEMS microhotplate gas sensing platforms, *Applied Physics Letters*, 2007, **91**, 063118.

149. G. Sberveglieri, C. Baratto, E. Comini, G. Faglia, M. Ferroni, M. Pardo, A. Ponzoni and A. Vomiero, Semiconducting tin oxide nanowires and thin films for chemical warfare agents detection, *Thin Solid Films*, 2009, **517**, 6156-6160.

150. W. H. Steinecker, M. P. Rowe and E. T. Zellers, Model of vapor-induced resistivity changes in gold− thiolate monolayer-protected nanoparticle sensor films, *Analytical chemistry*, 2007, **79**, 4977-4986.

151. S. J. Patrash and E. T. Zellers, Characterization of polymeric surface acoustic wave sensor coatings and semiempirical models of sensor responses to organic vapors, *Analytical chemistry*, 1993, **65**, 2055-2066.

152. C. Jin, P. Kurzawski, A. Hierlemann and E. T. Zellers, Evaluation of multitransducer arrays for the determination of organic vapor mixtures, *Analytical chemistry*, 2008, **80**, 227-236.

153. C. Jin and E. T. Zellers, Limits of recognition for binary and ternary vapor mixtures determined with multitransducer arrays, *Analytical chemistry*, 2008, **80**, 7283-7293.

154. M. Haug, K. Schierbaum, G. Gauglitz and W. Göpel, Chemical sensors based upon polysiloxanes: comparison between optical, quartz microbalance, calorimetric, and capacitance sensors, *Sensors and Actuators B: Chemical*, 1993, **11**, 383-391.

155. J. Mitrovics, H. Ulmer, U. Weimar and W. Göpel, Modular sensor systems for gas sensing and odor monitoring: the MOSES concept, *Accounts of chemical research*, 1998, **31**, 307-315.

156. K. Schierbaum, A. Gerlach, M. Haug and W. Göpel, Selective detection of organic molecules with polymers and supramolecular compounds: application of capacitance, quartz microbalance and calorimetric transducers, *Sensors and Actuators A: Physical*, 1992, **31**, 130-137.

157. A. J. Ricco, R. M. Crooks and G. C. Osbourn, Surface acoustic wave chemical sensor arrays: new chemically sensitive interfaces combined with novel cluster analysis to detect volatile organic compounds and mixtures, *Accounts of Chemical Research*, 1998, **31**, 289-296.

158. B. J. Doleman, M. C. Lonergan, E. J. Severin, T. P. Vaid and N. S. Lewis, Quantitative study of the resolving power of arrays of carbon black− polymer composites in various vapor-sensing tasks, *Analytical Chemistry*, 1998, **70**, 4177-4190.

159. J. Park, W. A. Groves and E. T. Zellers, Vapor recognition with small arrays of polymer-coated microsensors. A comprehensive analysis, *Analytical chemistry*, 1999, **71**, 3877-3886.

160. L. Han, X. Shi, W. Wu, F. L. Kirk, J. Luo, L. Wang, D. Mott, L. Cousineau, I. Stephanie and I. Lim, Nanoparticle-structured sensing array materials and pattern recognition for VOC detection, *Sensors and Actuators B: Chemical*, 2005, **106**, 431-441.

161. M.-D. Hsieh and E. T. Zellers, Limits of recognition for simple vapor mixtures determined with a microsensor array, *Analytical chemistry*, 2004, **76**, 1885-1895.

162. E. T. Zellers, S. A. Batterman, M. Han and S. J. Patrash, Optimal coating selection for the analysis of organic vapor mixtures with polymer-coated surface acoustic wave sensor arrays, *Analytical chemistry*, 1995, **67**, 1092-1106.

163. M. Pardo, L. Kwong, G. Sberveglieri, K. Brubaker, J. Schneider, W. Penrose and J. Stetter, Data analysis for a hybrid sensor array, *Sensors and Actuators B: Chemical*, 2005, **106**, 136-143.

164. H. Ulmer, J. Mitrovics, G. Noetzel, U. Weimar and W. Göpel, Odours and flavours identified with hybrid modular sensor systems, *Sensors and Actuators B: Chemical*, 1997, **43**, 24-33.

165. R. Zhou, A. Hierlemann, U. Weimar and W. Göpel, Gravimetric, dielectric and calorimetric methods for the detection of organic solvent vapours using poly (ether urethane) coatings, *Sensors and Actuators B: Chemical*, 1996, **34**, 356-360.

166. R. A. Potyrailo and W. G. Morris, Multianalyte chemical identification and quantitation using a single radio frequency identification sensor, *Analytical chemistry*, 2007, **79**, 45-51.

167. F. Battiston, J.-P. Ramseyer, H. Lang, M. Baller, C. Gerber, J. Gimzewski, E. Meyer and H.-J. Güntherodt, A chemical sensor based on a microfabricated cantilever array with simultaneous resonance-frequency and bending readout, *Sensors and Actuators B: Chemical*, 2001, **77**, 122-131.

168. R. A. Potyrailo, M. Larsen and O. Riccobono, Detection of Individual Vapors and Their Mixtures Using a Selectivity-Tunable Three-Dimensional Network of Plasmonic Nanoparticles, *Angewandte Chemie International Edition*, 2013, **52**, 10360-10364.

169. H. Chen, L. Shao, Q. Li and J. Wang, Gold nanorods and their plasmonic properties, *Chemical Society Reviews*, 2013, **42**, 2679-2724.

170. K. A. Willets and R. P. Van Duyne, Localized surface plasmon resonance spectroscopy and sensing, *Annu. Rev. Phys. Chem.*, 2007, **58**, 267-297.

171. K. M. Mayer and J. H. Hafner, Localized surface plasmon resonance sensors, *Chemical reviews*, 2011, **111**, 3828-3857.

172. K.-J. Chen and C.-J. Lu, A vapor sensor array using multiple localized surface plasmon resonance bands in a single UV–vis spectrum, *Talanta*, 2010, **81**, 1670-1675.

173. C.-S. Cheng, Y.-Q. Chen and C.-J. Lu, Organic vapour sensing using localized surface plasmon resonance spectrum of metallic nanoparticles self assemble monolayer, *Talanta*, 2007, **73**, 358-365.

174. M. C. Dalfovo, R. C. Salvarezza and F. J. Ibañez, Improved vapor selectivity and stability of localized surface plasmon resonance with a surfactant-coated au nanoparticles film, *Analytical chemistry*, 2012, **84**, 4886-4892.

175. T. Karakouz, A. Vaskevich and I. Rubinstein, Polymer-coated gold island films as localized plasmon transducers for gas sensing, *The Journal of Physical Chemistry B*, 2008, **112**, 14530-14538.

176. A. Monkawa, T. Nakagawa, H. Sugimori, E. Kazawa, K. Sibamoto, T. Takei and M. Haruta, With high sensitivity and with wide-dynamic-range localized surface-plasmon resonance sensor for volatile organic compounds, *Sensors and Actuators B: Chemical*, 2014, **196**, 1-9.

177. K. Kosuda, J. Bingham, K. Wustholz and R. Van Duyne, in *Comprehensive Nanoscience and Nanotechnology*, Elsevier, Dutch, Second Edition, 2016, 4.06, 117-152.

178. E. T. Zellers, T.-S. Pan, S. J. Patrash, M. Han and S. A. Batterman, Extended disjoint principal-components regression analysis of SAW vapor sensor-array responses, *Sensors and Actuators B: Chemical*, 1993, **12**, 123-133.

179. S. M. Scott, D. James and Z. Ali, Data analysis for electronic nose systems, *Microchimica Acta*, 2006, **156**, 183-207.

180. R. E. Shaffer, S. L. Rose-Pehrsson and R. A. McGill, A comparison study of chemical sensor array pattern recognition algorithms, *Analytica Chimica Acta*, 1999, **384**, 305-317.

181. E. Llobet, E. L. Hines, J. W. Gardner and S. Franco, Non-destructive banana ripeness determination using a neural network-based electronic nose, *Measurement Science and Technology*, 1999, **10**, 538.

182. T. P. Vaid, M. C. Burl and N. S. Lewis, Comparison of the performance of different discriminant algorithms in analyte discrimination tasks using an array of carbon black− polymer composite vapor detectors, *Analytical Chemistry*, 2001, **73**, 321-331.

183. M. Bicego, G. Tessari, G. Tecchiolli and M. Bettinelli, A comparative analysis of basic pattern recognition techniques for the development of small size electronic nose, *Sensors and Actuators B: Chemical*, 2002, **85**, 137-144.

184. R. Dutta, E. L. Hines, J. W. Gardner, D. D. Udrea and P. Boilot, Non-destructive egg freshness determination: an electronic nose based approach, *Measurement Science and Technology*, 2003, **14**, 190.

185. M. Kuske, R. Rubio, A.-C. Romain, J. Nicolas and S. Marco, Fuzzy k-NN applied to moulds detection, *Sensors and Actuators B: Chemical*, 2005, **106**, 52-60.

186. J. W. Grate, D. A. Nelson and R. Skaggs, Sorptive behavior of monolayer-protected gold nanoparticle films: implications for chemical vapor sensing, *Analytical chemistry*, 2003, **75**, 1868-1879.

187. M. A. Sharaf, D. L. Illman and B. R. Kowalski, *Chemometrics*, John Wiley & Sons, USA, 1986.

188. J. Wang, N. Nuñovero, R. Nidetz, S. J. Peterson, B. M. Brookover, W. H. Steinecker and E. T. Zellers, Belt-Mounted Micro-Gas-Chromatograph Prototype for Determining Personal Exposures to Volatile-Organic-Compound Mixture Components, *Analytical chemistry*, 2019, **91**, 4747-4754.

189. Y. Sun, S. I. Shopova, G. Frye-Mason and X. Fan, Rapid chemical-vapor sensing using optofluidic ring resonators, *Optics letters*, 2008, **33**, 788-790.

190. Y. Sun and X. Fan, Analysis of ring resonators for chemical vapor sensor development, *Optics express*, 2008, **16**, 10254-10268.

191. Y. Sun, J. Liu, D. J. Howard, G. Frye-Mason, A. K. Thompson, S.-j. Ja and X. Fan, Rapid tandem-column micro-gas chromatography based on optofluidic ring resonators with multi-point on-column detection, *Analyst*, 2010, **135**, 165-171.

192. M. D. Baaske, M. R. Foreman and F. Vollmer, Single-molecule nucleic acid interactions monitored on a label-free microcavity biosensor platform, *Nature nanotechnology*, 2014, **9**, 933.

193. V. R. Dantham, S. Holler, C. Barbre, D. Keng, V. Kolchenko and S. Arnold, Label-free detection of single protein using a nanoplasmonic-photonic hybrid microcavity, *Nano letters*, 2013, **13**, 3347-3351.

194. S. Shopova, R. Rajmangal, S. Holler and S. Arnold, Plasmonic enhancement of a whispering-gallery-mode biosensor for single nanoparticle detection, *Applied Physics Letters*, 2011, **98**, 243104.

Chapter 2

A Nanomaterial-coated Micro-optofluidic Ring Resonator for Vapor Detection

2.1 Introduction

Currently available portable (wearable) instruments for VOCs are generally too large and expensive for personal exposure monitoring, many lack sufficient sensitivity, and most lack the capability for the quantitative determinations (i.e., identification and quantification).[1] Addressing this technology gap, significant advances have been made in the development of miniaturized VOC-monitoring instrumentation using MEMS techniques.[2-7] Prof. Zellers' group has been at the forefront of such efforts,[2,5-12] and has developed the first-ever wearable μGC, referred to as a Personal Exposure Monitoring Microsystem (PEMM).[13] Figure 2.1 shows a block diagram of the analytical subsystem and photographs of the microcomponents and the fully packaged PEMM field prototype. In the PEMM prototype, the detector comprises an array of chemiresistors (CR) with thin films of functionalized monolayer-protected gold nanoparticles (MPNs) as interface layers that interact with vapors by reversible sorption, which produces transient resistance changes in the MPN films.

Arrays of 3-10 such CRs are broadly responsive, yet partially selective; the collective response pattern derived from sensors in the array, which have complementary interface layers, can be used to differentiate one vapor from another individual vapor.[14] But the quantitative analysis

of ternary or higher mixtures is not possible, regardless of the number of sensors in the array. This is a problem for μGC systems with inherently short separation columns, since the likelihood of overlapping peaks is significant.[5] Thus, such array detectors are limited by their low response diversity.[15]

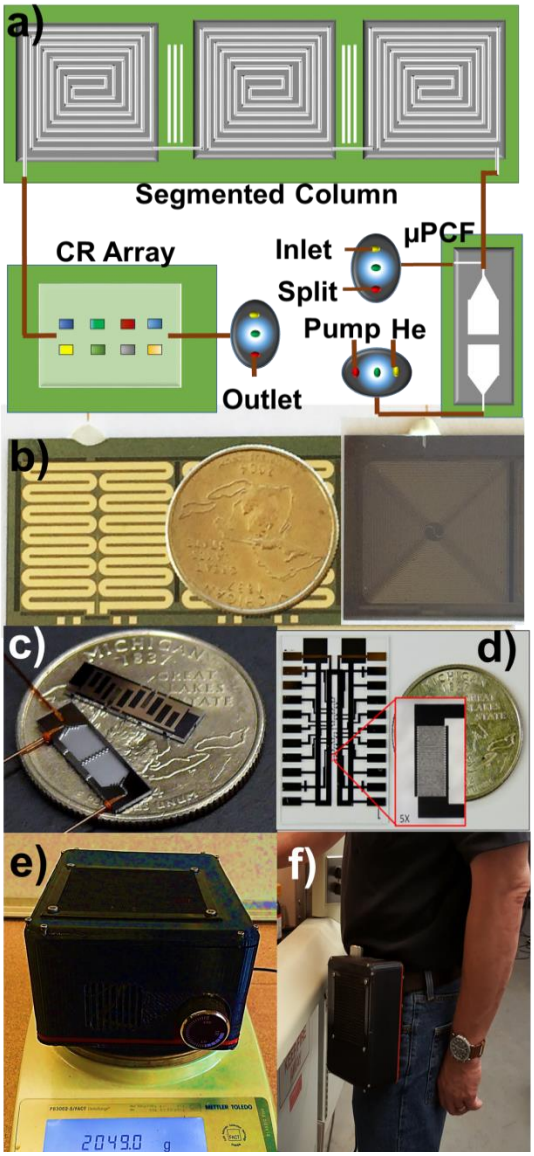

Figure 2.1 (a) Fluidic layout of PEMM analytical subsystem and photos of (b) segmented μcolumn, (c) microfabricated preconcentrator-focuser (μPCF), (d) μCR array. The PEMM is 7×3.7×2.3"and (f) light enough to (e) wear on the belt.

The modular design of the microsystem in this instrument platform facilitates testing of alternate sensing technologies. In a parallel project, we have been exploiting the optical properties of MPNs instead of their electrical properties for vapor sensing. The absorbance of visible light by MPN films is influenced by the localized surface plasmon resonance (LSPR) arising from the interaction of incident light with free electrons on the surfaces of the gold nanoparticle cores. Sorption of VOCs into the organic monolayers comprising the inter-core matrix of MPN films can change the thickness, inter-core spacing, and refractive index (RI). The resulting absorbance changes can be related to the gas-phase VOC concentration.[16,17] This approach to increasing diversity and improving vapor discrimination has been called multi-variable (MV) sensing, since several ostensibly independent parameters are measured from each sensor. MV

sensing shows considerable promise because of the ability to probe multiple wavelengths and increase response diversity as discussed in Chapter 1.[17] Our group has recently shown that we can discriminate among 6 different individual VOCs with a single MPN film probed at 3 wavelengths flanking the LSPR maximum via optical transmission measurements with a spectrophotometer (unpublished results). Thus, a single film can achieve optically what it requires an array of 3-10 MPN-coated CR sensors to achieve electrically. A microsensor suitable for integration with a μGC that can capitalize on this optical sensing diversity is needed.

The optofluidic ring resonator (OFRR) is a unique optical sensing platform in which vapor sensing and fluidic transport functions are combined.[18,19] Whispering gallery modes (WGMs) are generated in the wall of a glass capillary by a proximal optical fiber taper, and the evanescent component of the WGM probes the inner surface of the OFRR capillary. By scanning the laser wavelength and monitoring the output intensity across the waveguide a resonant wavelength (λ_{WGM}) can be identified. Any change in optical properties (e.g., RI) near the surface causes a shift in λ_{WGM}, which serves as a sensor response. Figure 2.2.(a) summarizes the sensing concept.

Scholten et al., (Zellers group) recently introduced a microfabricated optofluidic ring resonator (μOFRR) and characterized its performance, with a PDMS wall coating, as a detector downstream from conventional and μGC separation columns.[12,20,21] Figure 2.2.(b)-(d) show images of one of our first devices, the configuration of the packaged chip and the 3-D printed fixture we used for collecting measurements. Resonator structures are SiO_x cylinders ~80 μm tall with 50-250 μm i.d. $\leq$ 2 μm thick walls after partial release from the Si substrate on which they are grown. WGMs could be excited in the wall by coupling a modulated laser signal via a proximal optical fiber taper, and λ_{WGM} could be identified as the minimum in output intensity across the fiber. High sensitivities and rapid responses to VOCs were obtained with a PDMS-coated

μOFRR,[20,21] and it was of interest to explore whether an MPN-coated device might afford similar performance, with the added prospect of (eventually) imparting selectivity by virtue of the wavelength dependence of VOC responses afforded by such plasmonic interface films. They recently succeeded in coating with a TEG MPN (Fig. 2.3) film and probing with an infrared laser.[21] It remains to demonstrate that it can work with lasers in the visible range where advantage can be taken of the LSPR.

The use of μOFRRs with MPN interface layers represents a new approach to vapor sensor design suitable for integration into a μGC platform. The diversity of responses afforded by an optimized individual μOFRR (and, ultimately, perhaps a μOFRR array) should enhance capabilities for analyte recognition/discrimination, particularly if only partly chromatographically resolved. This would represent a significant advancement in personal monitoring μGC instrumentation.

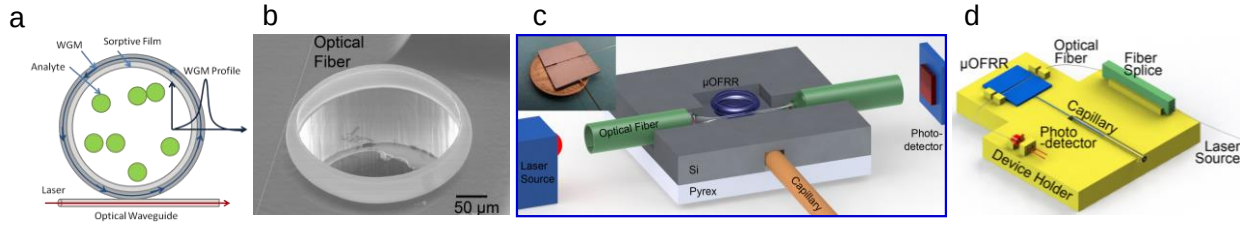

Figure 2.2 (a) Basic operation of the OFRR; (b) SEM image of the μOFRR (250 μm i.d.); (c) cartoon depicting the μOFRR with capillary and optical fiber connections (inset: photo of a fully packaged 2×2 cm μOFRR device on a US penny); (d) diagram of the 3-D printed jig onto which the μOFRR was mounted and fitted with optical/fluidic interconnections for facile interfacing with a GC or μGC.[12,19]

The ultimate goal of the study described here was to enhance the capabilities of emerging microscale gas chromatographic (μGC) instrumentation designed for the quantitative analysis of complex VOC mixtures of arbitrary composition. The ultimate deliverable would have been a

prototype version of a belt-mountable exposure monitor that provides the identity and quantity of VOCs at occupationally-relevant air concentrations every 10 min for 8 hr. This study builds on recent advances made in Prof. Zellers' group on such a small, battery-powered μGC prototype and on a novel optical microsensor technology that shows promise as an improved μGC detector. By attempting to bridge the gap between these two related projects, the current study sought to generate 'proof-of-principle' results that would show the feasibility of this approach to personal direct-reading instrumentation for workplace exposure monitoring.

The first aim (Aim 1) was to identify the best MPN films to use as potential μOFRR interface films and to characterize the diversity of their optical responses to VOCs by use of conventional optical (visible) transmission measurements on ordinary glass substrates. Our MPN film deposition technique was to be refined to improve response reproducibility. Aim 2 was to install an MPN-coated μOFRR as a bench scale GC detector and verify reliable performance under dynamic exposure conditions. Aim 3 was to demonstrate the MPN-μOFRR as a μGC detector using our latest laboratory μGC prototype or belt-mountable field μGC prototype. Progress was made toward Aims 1 and 2. Unfortunately, Aim 3 was not attempted prior to the conclusion of this project.

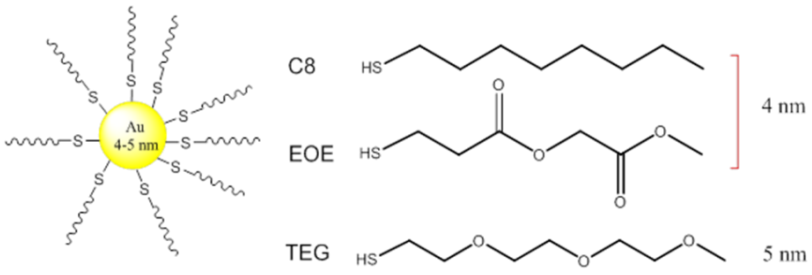

Figure 2.3 Structures of the thiols used to make the MPNs tested as optical MV sensing films for VOCs. Acronyms are used through the report to designate the different MPNs.

2.2 Experimental Methods

2.2.1 Materials

Most test compounds, tetrachloroethylene (PCE), toluene (TOL), n-octane (OCT), butyl acetate (BAC), 2-butanone (MEK), and isopropanol (IPA), were purchased from Sigma-Aldrich (Milwaukee, WI) in >98% purity and were used as received. The grafting reagents including ctadecyltrichlorosilane (OTS), hexamethyldisilazane (HMDS), and mercaptopropyltrimethoxysilane (MPTS) were obtained from EMD (Billerica, MA) and Sigma-Aldrich (Milwaulkee, WI). PDMS was purchased from the Ohio Valley Specialty Company (OV-1, Marietta, OH). TEG-MPNs were obtained from Sigma Aldrich (St. Louis, MO). Cetyl trimethylammonium bromide (CTAB) functionalized nanorods (NR) was purchased from Nanopartz (Loveland, CO). The TFA gold etchant solution was purchased from Transene Company, Inc. (Danvers, MA).

2.2.2 Testing

To achieve Aim 1 we performed screening tests on pre-treated glass substrates to try to identify the best MPNs to use as μOFRR interface films and to characterize/quantify their optical responses to VOCs at three visible wavelengths. All testing used existing stocks of MPNs, the thiolate monolayers of which are shown in Figure 2.3. These were selected for this study to span a wide range of polarity such that there would be a wide range of interaction forces governing sorptive vapor-ligand affinities, as reflected in the well-known Linear Solvation Energy Relationships (LSER) model.[22] The MPNs had either 4 or 5 nm diameter core sizes.

Since previous replicate films of MPNs solvent cast onto glass substrates provided responses to VOCs that varied considerably from film to film, we endeavored to refine our coating

methodology to improve reproducibility. We constrained our approach to solvent casting, rather than, say, spin-coating or ink-jet printing, because the latter are not amenable to μOFRR film deposition due to its unique vertical wall orientation. Different surface modifications were explored in an attempt improve the anchoring/ordering of the MPNs on glass substrates, all of which entailed grafting a monolayer on the glass with the appropriate terminal functional group.[23] For example, terminal alkyl groups render the surface hydrophobic, and should enhance uniformity/density/adhesion of MPNs with alkyl or aromatic ligands. On the other hand, thiol terminal groups on the graft permit Au-S coordination with the first layer of MPNs and thereby should enhance film uniformity/density/adhesion for all types of MPNs. Since we require multi-layered films (~100-300 nm thick, i.e., 3-60 layers), we would rely on establishing a uniform base layer upon which subsequent MPNs will pack/align.[24]

Structures of the grafting reagents used in this study are presented in Figure 2.4. The chloro- or alkoxy-silane groups hydrolyze and form an Si-O-Si bond to the glass surface, leaving the terminal groups to interact with the MPNs.[23] Tests were performed with C8-MPN. Diced glass chips were cleaned with Piranha solution (H_2SO_4 (98%):H_2O_2 (30%) = 1:5, v/v) prior to grafting (caution: Piranha self-heats to about 100 °C upon mixing the two reagents, and it is a voracious oxidizing agent). The surface pre-treatments of the cleaned glass substrates with OTS, HMDS, and MPTS were performed according to reported methods.[25] Briefly, each glass chip was placed in MPTS (70 μM, in methanol), OTS (70 μM, in chloroform: hexane = 1:4, v/v), or HMDS (70 μM, in chloroform) for 1h and washed with corresponding solvent three times to remove the free grafting agent, then dried using N_2 prior to use.

Approximately 5μL of a C8-MPN solution (5mg/mL in toluene) was drop casted via a microliter syringe on the OTS, HMDS, MPTS pre-treated glass substrates, as well as on a Piranha-

washed glass. The uniformity of the C8-MPN films was examined by optical microscopy after solvent evaporation.

In addition to surface pretreatments, we explored different casting solvents. C8-MPNs were dispersed in toluene/ethanol (v:v = 1:1), neat hexane, and hexane/ethanol (v:v = 1:1) separately to yield 5 mg/mL solutions. The C8-MPNs were then drop cast onto HMDS-treated substrates using a microliter syringe as above. Films were then inspected by microscopy.

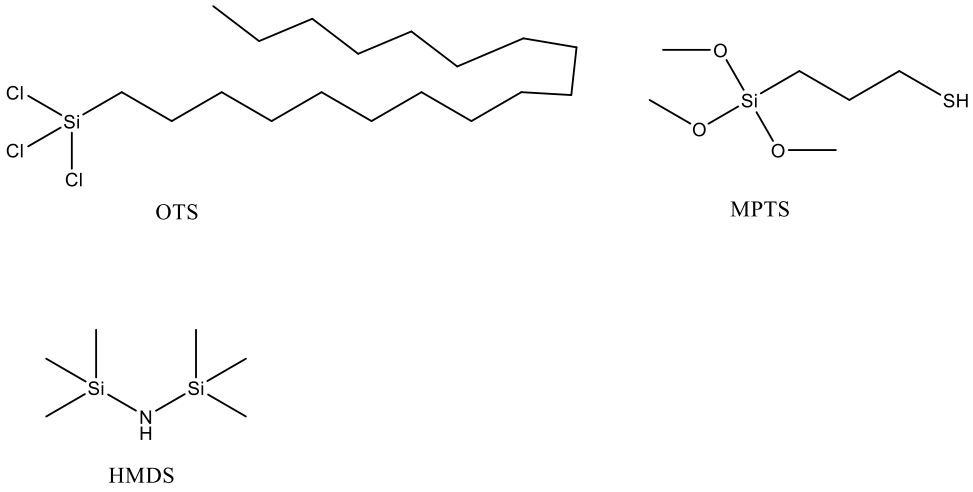

Figure 2.4 Structure of grafting reagents used to modify the surface of diced glass.

To screen and rank the best MPN film for vapor recognition, 5 µL of 5 mg/mL solutions (C8-MPN, EOE-MPN in toluene; TEG-MPN in ethanol) were drop cast on both sides of separate HMDS pre-treated glass substrates. Coated substrates were placed in a standard glass cuvette fitted with gas flow ports for vapor exposure, and the shifts in the absorbance from 400-800 nm were recorded upon steady-state exposures to individual test VOCs at 50% of the saturation concentrations, C_{sat}.

Test vapors were generated using a home-built vapor generating system in which scrubbed house air was passed through a fritted bubbler of the liquid analyte, followed by dilution in a dry,

scrubbed air stream maintained at 2 L/min. A small fraction of this contaminated air stream (i.e., ~30 mL/min) was directed through deactivated fused silica capillary to the septum-sealed cuvette via a press-tight connection. Switching from vapor-laden air to clean air was performed manually. Vapor concentrations were confirmed by periodically directing a fraction of the flow through a 250 μL sample loop and injecting via a 6-port valve through a 6-m capillary column to a flame ionization detector (FID). Pre- and post-exposure baseline spectra were collected for 5 min each. Triplicate exposures conducted for a subset of vapors over the course of the study gave relative standard deviations of < 5% around the average shifts in absorbance.

To assess film-to-film reproducibility, two HMDS-modified substrates were drop cast with 5 μL of C8-MPN solution and their visible transmission spectra recorded before and during exposure to PCE and OCT, in sequence. To assess within-film reproducibility, spectra of the C8 MPN film exposed to PCE and OCT were recorded after changing the position of the substrate within the cuvette so that the light beam passed through different regions of the film. Chemometric analyses of the data sets entailed principal components analysis (PCA) to map response vectors in 3-D space onto a two-dimensional surface, and to estimate Euclidean distances to quantify diversity among the responses corresponding to each vapor.

For Aim 2 we initially characterized a newly fabricated μOFRR device with a coating film of a rubbery polymer, PDMS, and then with films of TEG-MPN, and then with a CTAB functionalized Au nanorod material (which was not part of the original proposal). Our last fabrication run yielded 12 μOFRR devices. Wall thickness, primary cylinder internal diameter, effective height, and expansion section diameter of the μOFRR device were the same as those for a previous fabrication run using the same processing steps:[20] 1.2 μm, 250 μm, 85 μm, and 280 μm

respectively. SEM images confirmed all but the wall thickness, which could not be measured precisely.

A 20-min immersion of the chip in Piranha etch was used to remove organic residues from the surface of each device prior to coating. If a specific device had been coated previously with an MPN film, then it was immersed for 15 min in a gold etchant solution (Transene TFA Gold etchant) to ensure removal of any MPN residue. In any case, immediately before depositing a new coating, the device was rinsed with acetone and then IPA, and then dried in air.

Coating was performed as in previous work[20,21] by filling the μOFRR cavity with a solution of the interface material and allowing the solvent to evaporate under gentle vacuum. More specifically, the chip was inverted and gently pressed into a rubber septum to seal the top of μOFRR cavity. For initial tests with PDMS, 10 μL of a PDMS solution in toluene (~2.3 mg/mL) was deposited over the device aperture on the backside of the chip. Then the device was placed in a vacuum desiccator overnight under house vacuum to draw the solution into the cavity and to evaporate the solvent. Based on the PDMS solution concentration and the estimated volume and surface area of the cavity, a ~300 nm layer of PDMS film formed on the inner wall of the ring structure, assuming a uniform film.

A tapered fiber, ~2 μm diameter at its narrowest point, was temporarily placed near the equator of the ring resonator to confirm the ability to generate and measure a WGM resonance. The fiber positioning and alignment apparatus includes two motion control stages and a microscope camera to precisely adjust the position of the fiber in proximity to the expansion region of the resonator cavity. The μOFRR was then removed and a 2×2 cm Pyrex cover plate was affixed on the backside of the chip with UV curable adhesive. Then a short segment of deactivated fused-

silica capillary (250 μm i.d.) was inserted into the fluidic channel (cross section = 380 × 380 μm) etched along the backside of the chip (between the center aperture and the edge of the chip) and sealed by epoxy.

The same tapered optical fiber was then positioned in the etched fiber-alignment channel on the top surface of the device (Figure 2.2.(c)) in close proximity to the ring resonator expansion section to stimulate the WGM. It was secured with UV-curable adhesive. The laser source was a tunable 1550-nm distributed feedback (DFB) laser diode (CQF935/208, JDS Uniphase, Milpitas, Ca). The photodetector was a large-area IR photodetector (2033, New Focus, Irvine CA). The optical fiber was drawn to a very narrow diameter that improved coupling to the ring resonator. The WGM resonance and its shifts were monitored by the photodetector and recorded by custom LabVIEW program. We had planned to use lasers with center wavelengths near 400, 500, and 600 nm but our initial budgeting was incorrect as to the cost of such lasers and we could not afford them on the budget allowed. Thus, for these initial tests with PDMS and for all testing in this study we used the 1550-nm near-IR laser.

Although the C8-MPN film showed the greatest diversity in the tests performed for Aim 1, it had already been shown to be difficult to coat on the μOFRR.[21] In contrast, the TEG-MPN material formed more uniform films, and so it was chosen as the inaugural MPN for this study. Preliminary experiments were performed to evaluate the effect of the coating film thickness on the establishment of a detectable WGM signal. Three concentrations of TEG-MPN in ethanol were prepared: 0.005 mg/mL, 0.05 mg/mL, 0.5 mg/mL. Then we used the same coating method as for PDMS coating to screen for the effect of MPN concentration (and resulting films thickness) on performance. As discussed below, the film formed from the 0.05 mg/mL solution gave the best results. This corresponds to a nominal thickness of 6.5 nm assuming uniform deposition. We also

we explored a spin coating method to improve the uniformity of the film, but the procedure was not well documented and results were mixed.

The device coated with the optimal amount of TEG-MPN was then fitted with a Pyrex plate to seal the backside of the chip. This time, instead of using UV-curable adhesive, we used double-sided tape to secure the plate. The interconnecting capillary was inserted and sealed with epoxy (Duraseal 1531, Cotronics Corp., Brooklyn, NY), as before.

For exposure testing, the interconnecting capillary was connected via a standard press-fit connector to a 10-m long, 250 μm i.d., capillary "guard column", which was installed in a bench scale GC (3800 Varian GC, Varian, Inc., Palo Alto, CA). The flow rate of helium carrier gas was 1.2 mL/min at the end of the column, and the injection split ratio was 80:1. Manual injections of headspace vapor samples from vials containing test compounds, including 3-heptanone, were made.

In an unplanned set of experiments we explored the use of a CTAB functionalized Au NR material as a μOFRR coating. The MPN coatings exhibit LSPR maxima near 570 nm. However, single- frequency, tunable laser sources at this wavelength are very expensive, as it turns out (in contrast to our previous understanding). The LSPR maximum of certain Au NRs is within the near infrared region where less expensive lasers have their emission lines, and in a study of a so-called "plasmonic-photonic microcavity" with Au NRs coating, an LSPR maximum near 980 nm was observed.[26] Thus, we decided to explore NRs comprising CTAB functionalized NRs with a 40 nm diameter and a 134 nm length.

The method of coating CTAB-nanorods (CTAB-NR) onto the interior wall of the μOFRR cavity used was similar with that of MPN coating. First, a proper concentration of CTAB-NR

solution was explored. The volume of the aqueous solution applied to the device was kept constant at 6 µL. We deposited solutions with different CTAB-NR concentrations, i.e., 0.0005 µg/mL, 0.005 µg/mL, 0.05 µg/mL, 0.5 µg/mL, and 5 µg/mL. All were dried overnight prior to testing. After each attempt at coating, the device roughly tested for vapor response by exposing to headspace vapors of benzene, acetone and toluene extracted from septum-sealed vials by a syringe and passed over the device while monitoring the WGM resonance using the tunable 1550-nm laser.

For Aim 3 we had proposed to integrate an MPN-µOFRR sensor into our PEMM µGC lab or field prototype and test the combined system with various target analyte mixtures. Unfortunately, our testing with the bench scale GC did not progress far enough to establish the baseline data needed to proceed with this last phase of the study.

As for the data acquisition and analysis of µOFRR, the photodiode and laser were connected to a DAQ card and controlled by a custom Labview program (Ver. 2019, National Instruments, Austin, TX). The laser wavelength was swept over 330 pm. The resonant wavelength, i.e. the wavelength at the photodiode output minimum, was determined and recorded by a peak finding algorithm in the Labview program. OriginPro 9.1(OriginLab, Northampton, MA) was used for the analysis of chromatographic data.

2.3 Results and Discussion

2.3.1 Film Morphology/Uniformity

Figure 2.5 presents photomicrographs of several C8-MPN films. As shown we were not able to create uniform C8-MPN films on either the Piranha-cleaned glass or the pre-treated glass. Figure 2.5 (a) is the C8 MPN film deposited on Piranha-cleaned surface, and Figures 2.5.(b)-(d) are the C8-MPN films deposited on pretreated glass. Based on visual observation, there is no

improvement in term of uniformity of C8 MPN film after treatment; the films still exhibited the classical “coffee ring” pattern due to solvent evaporation.

Figure 2.6 shows results obtained by modifying the solvents used to deposit C8 MPN films on HMDS pre-treated substrates. The “coffee ring” pattern of C8 MPN films did not disappear when using toluene/ethanol (v:v = 1:1) (Figure 2.6.(b)) or hexane (Figure 2.6.(d)). Interestingly, the pattern did disappear when hexane/ethanol (v:v = 1:1) (Figure 2.6.(f)) was used, and the film appears quite uniform. However, this film did not respond to ~50% C_{sat} octane vapor in optical measurement experiments, which could be due precipitation losses of the MPN from solution prior to coating, leading to a very thin film.

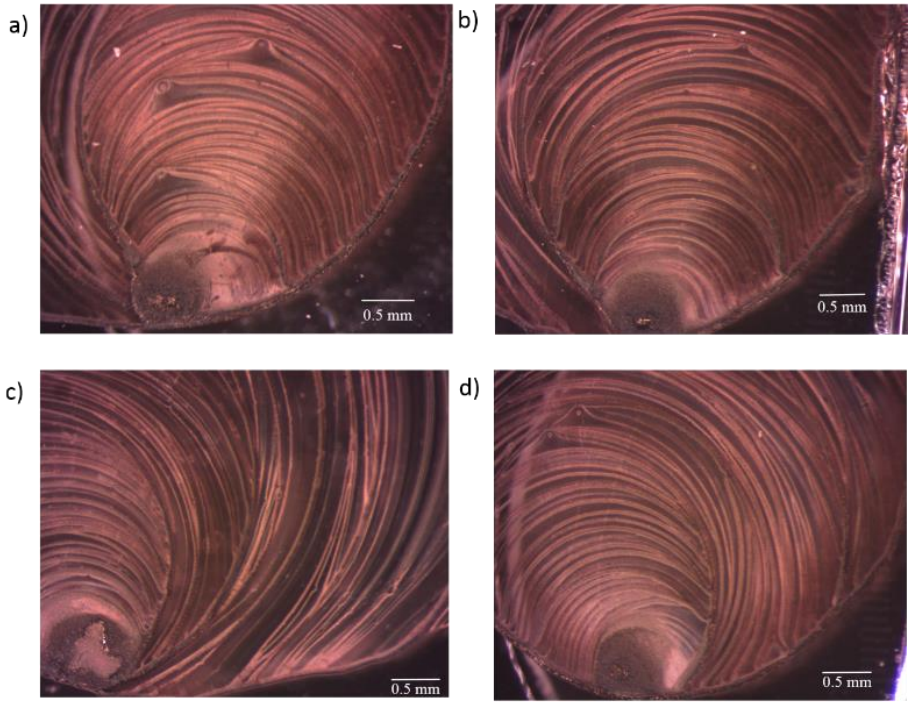

Figure 2.5 Morphology of C8-MPN films cast on: (a) Piranha-washed glass; (b) HMDS-treated glass; (c) OTS-treated glass; (d) MPTS-treated glass.

2.3.2 Screening of Response Diversity

Despite the inability to find a surface pretreatment or solvent formulation that improved film uniformity, we proceeded to screen and rank MPN films for vapor recognition using films of C8-, EOE-, and TEG-MPNs solvent cast onto both sides of separate HMDS pre-treated glass substrates and exposed sequentially to the six test VOCs at 50% C_{sat}. On the basis of our previous study, the shifts in absorbance at 405, 532, and 630 nm were selected to assess diversity. To generate a response pattern, the three shifts for a given vapor were divided by the largest shift among the three wavelengths. The resulting normalized responses are presented as bar charts in Figure 2.7.

It is evident merely from visual inspection that C8-MPN gives the greatest response diversity among the three MPN films. Responses are both positive and negative at the longer wavelengths and the relative magnitudes vary significantly among the different vapors. The patterns for PCE and TOL look quite similar to each other, while those for the other vapors differ significantly from those of PCE and TOL as well as from each other.

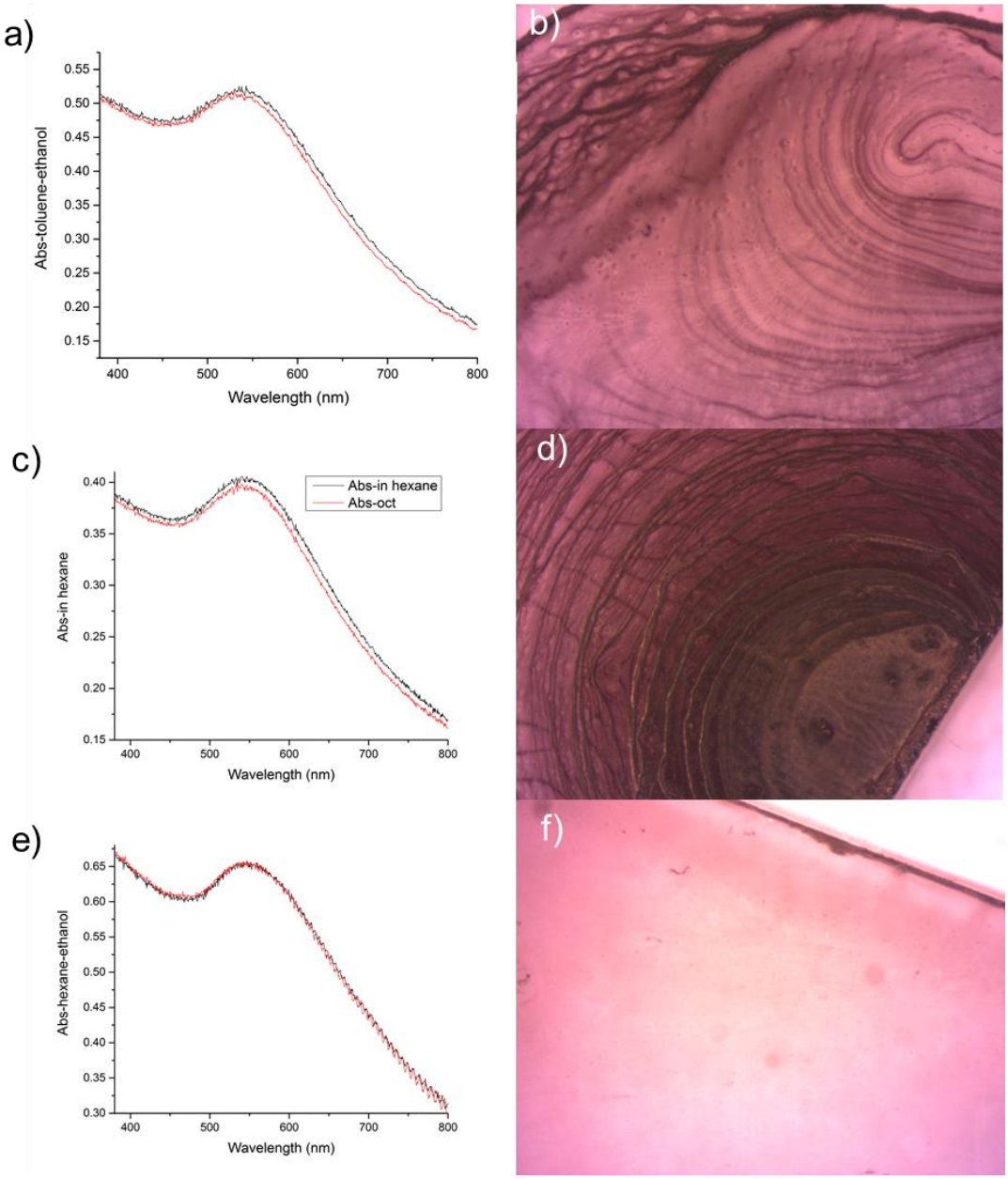

Figure 2.6 Visible transmission measurements of three plasmonic C8-MPN films casted on the glass with different solvents and their response to ~50% C_{sat} octane vapor. A: C8-MPNs in toluene/ethanol (v: v = 1: 1) and C8-MPN film morphology under microscope; B: C8-MPNs in hexane and C8-MPN film morphology under microscope; C: C8-MPNs in hexane/ethanol (v: v = 1: 1) and C8-MPN film morphology under microscope; (Black spectrum is absorption of C8-MPNs film, red spectrum is the absorption of C8-MPNs film exposed to ~50% C_{sat} octane vapor).

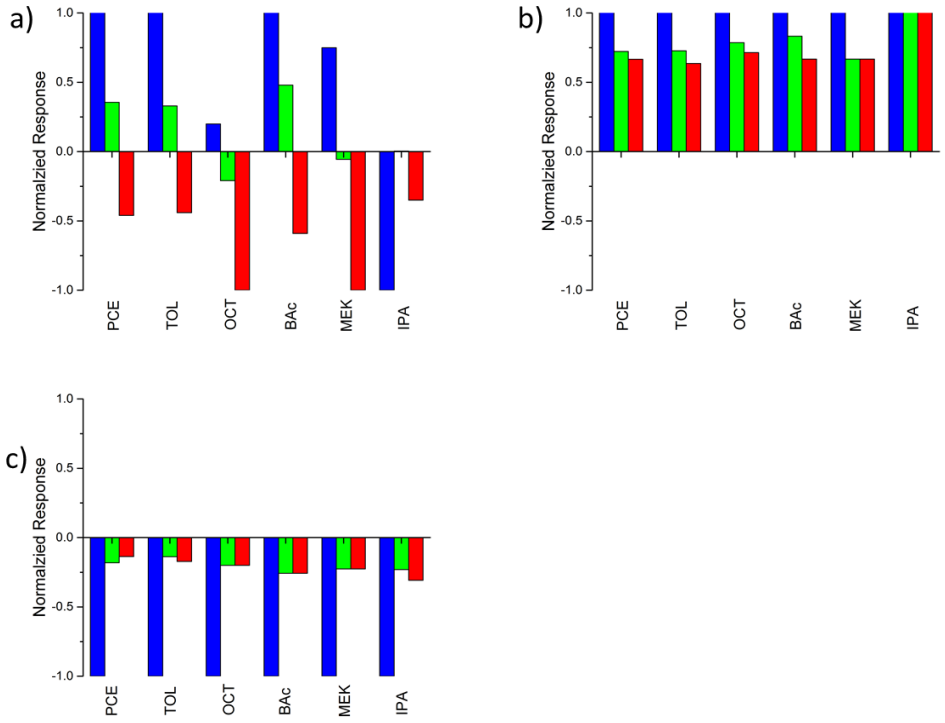

Figure 2.7 Response patterns from optical transmission measurements of three plasmonic MPN films exposed to each of six vapors at 50% C_{sat}. Each 3-wavelength pattern is normalized to the largest response for (a) C8; (b) EOE (c) TEG. Wavelengths: from left to right: blue = 405 nm; green = 532 nm; red = 630 nm. Acronyms refer toVOCs: perchloroethylene (PCE), toluene (TOL), n-octane (OCT), butyl acetate (BAC), methyl ethyl ketone (MEK), isopropanol (IPA).

Indeed, the PCA plot of the data obtained with the C8-MPN film shown in Figure 2.8 confirms the preceding observations: PCE and TOL cluster in a similar region and the other VOCs are widely separated. Although the response patterns of C8-MPN differ from those obtained in prior testing (performed by other group members prior to this study; unpublished), which is likely due to the un-uniformity of between films, the diversity of the response patterns is comparable, indicating that the C8-MPN material is promising for selectively recognizing vapors.

Figure 2.9 presents the response patterns obtained for exposure to PCE or OCT vapor (50% C_{sat}) from two separate C8-MPN films deposited on different substrates or from a single C8-MPN film probed at different locations within the same film/substrate. Glass substrate #1 and #2 were

exposed to the same concentrations of PCE or OCT. As shown in Figure 2.9.(a) for PCE, the absorbance intensity increased at 532 nm for substrate #1,but decreased for substrate #2. The normalized responses at 405, 532, and 630 nm differed between substrates #1 and #2, reflecting significant inter-film response characteristics. Similar variations in response patterns were observed for exposure to OCT vapor (~50% C_{sat}) as shown in Figure 2.9.(b) among the patterns for OCT-glass #1, OCT-glass #2 region 1, and OCT-glass #3 region 1.

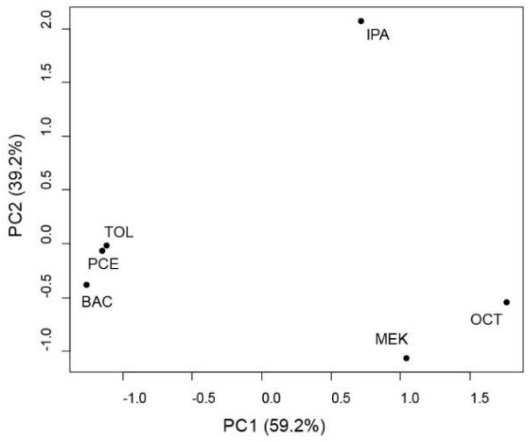

Figure 2.8 Principal components (PCA) score plot for individual vapor responses from the C8-MPN film measured by optical transmission – from Figure 2.7.(a).

In addition, the response patterns also differed for the same film probed at different regions. For example, the absorbance at 405 nm increased in the presence of PCE at region 1 (Figure 2.9.(a), glass #2-Region1) but decreased at region 2 (Figure 2.9.(a), glass #2-Region1). The same phenomenon was observed for a series of OCT exposure measurements (Figure 2.9.(b)). The combination of results shown in Figures 2.8 and 2.9 confirm previous findings of a lack of reproducibility in responses, owing mostly likely to differences in scattering losses, which must be extremely sensitive to surface morphology.

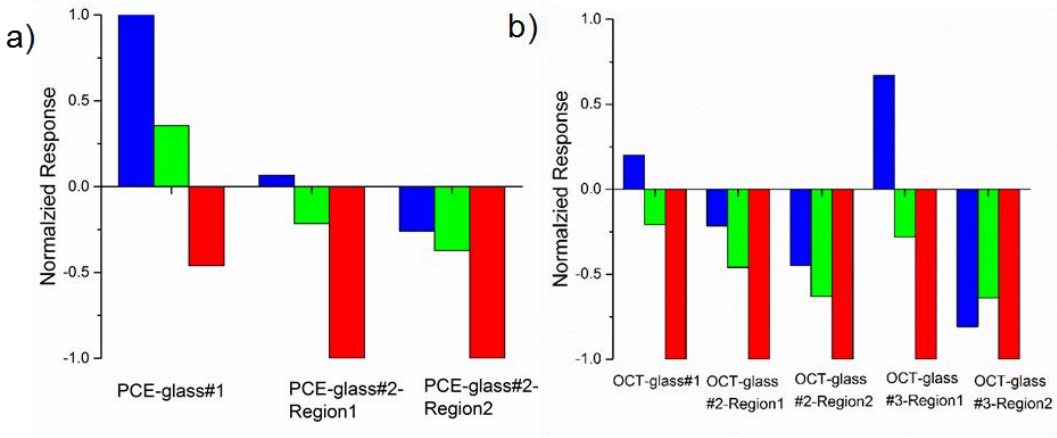

Figure 2.9 Response patterns of C8 MPN films to (a) PCE for different glass substrates or regions within a given substrate and (b) OCT for different glass substrates or regions within the same substrate. From left to right: blue = 405 nm; green = 532 nm; red = 630 nm. Concentrations of vapors were ~50% Csat.

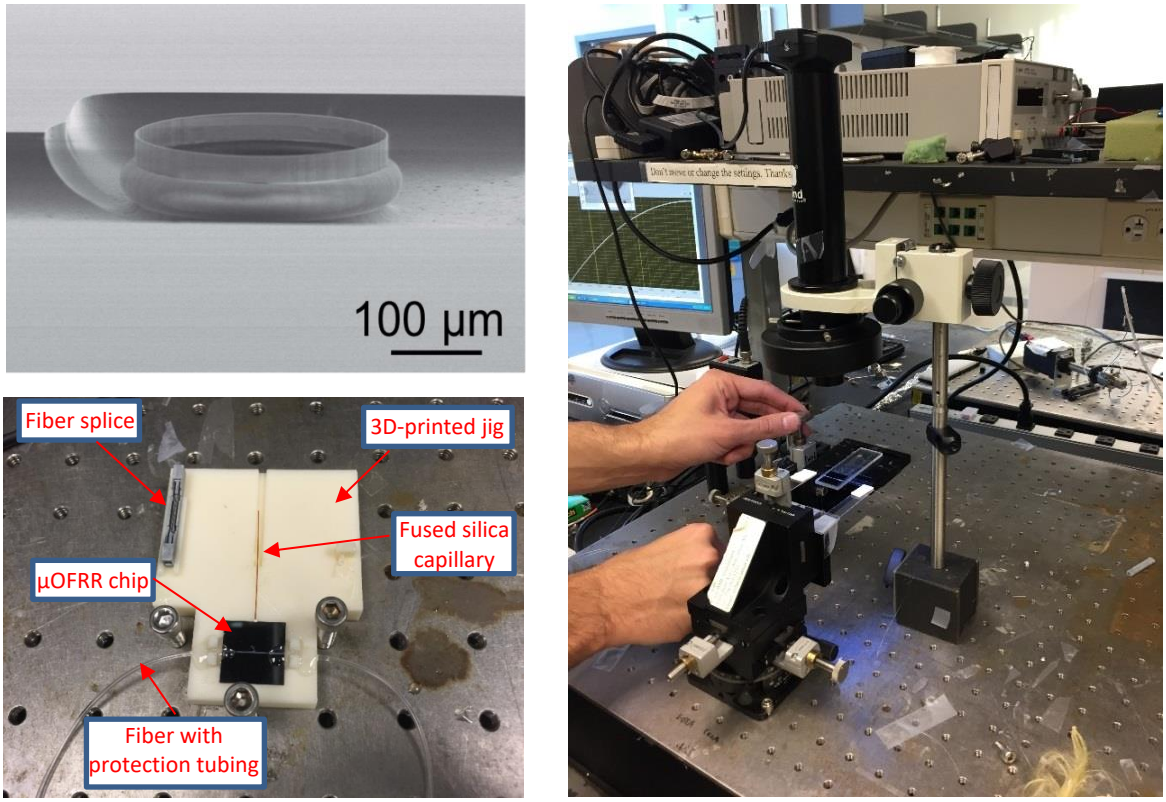

Figure 2.10 (a) SEM image of one of our new µOFRR device structures with embedded optical fiber alignment channel; (b) PDMS-coated µOFRR mounted on a 3-D printed fixture; (c) the apparatus used to position and align the optical fiber in the top-side channel running alongside the µOFRR cavity.

2.3.3 PDMS-Coated µOFRR

Figure 2.10.(a) shows an SEM image of one of our new µOFRR devices. The PDMS-coated device mounted on a 3-D printed plastic jig is shown in Figure 2.10.(b). The apparatus used to position and secure the drawn optical fiber in the µOFRR device is shown in Figure 2.10.(c). The WGM resonance was monitored by the photodetector and recorded by an in-house LabVIEW program. Although quantitative results were not collected, the quality factor (Q-factor) achieved was about 20,000 which is more than twice the Q-factor we have achieved with previous devices (~8,000). This may be the result of using a rigorous surface pretreatment/cleaning before coating or from improved coating uniformity. Improved coupling efficiency was also realized and is attributed to the developed fiber pulling technology which can achieve thinner and straighter tapered fiber.

When the device was exposed to the headspace concentrations of acetone, benzene and toluene, obvious resonance shifts (WGM spectral shifts) were observed. An example of resonance wavelength shift in a PDMS-coated µOFRR sensor during exposure to toluene is shown in Figure 2.11.

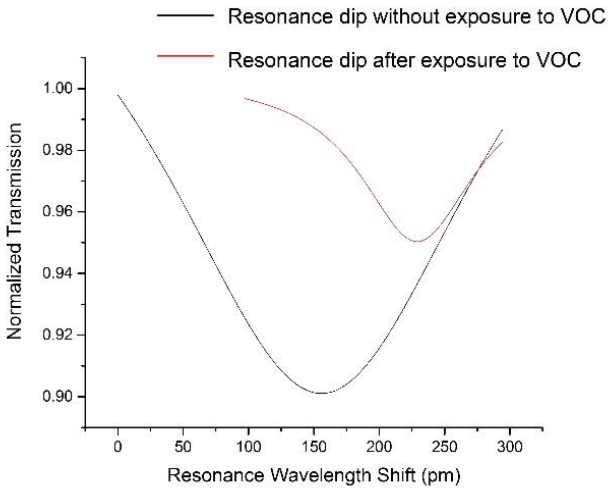

Figure 2.11 WGM resonance shift from PDMS-coated µOFRR sensor during exposure to a high (unknown) concentration of toluene vapor.

2.3.4 TEG-MPN coated μOFRR

After the evaporation of solvent in vacuum, we found that we could not detect a WGM resonance with the device coated with 0.5 mg/mL of the TEG-MPN. We could detect a resonance with the device coated with 0.005 mg/mL TEG-MPN but upon exposure to brief pulses of benzene, acetone, and toluene (i.e., samples of the headspace above vials of benzene, acetone, and toluene were collected in 10-mL gas tight syringe and then passed over the device), we did not detect any shift. The device coated with 0.05 mg/mL TEG-MPN not only yielded a WGM resonance but it also showed a shift in maximum wavelength upon similar vapor exposure.

Thus we found that if the MPN layer thickness (or number of MPNs) is too small, the vapor sensing response will not be observed even though we can observe the WGM resonance. This may result from the fact that the number of adsorbed vapor molecules is too small to change the RI or to swell the film sufficiently to generate an observable resonance wavelength shift.

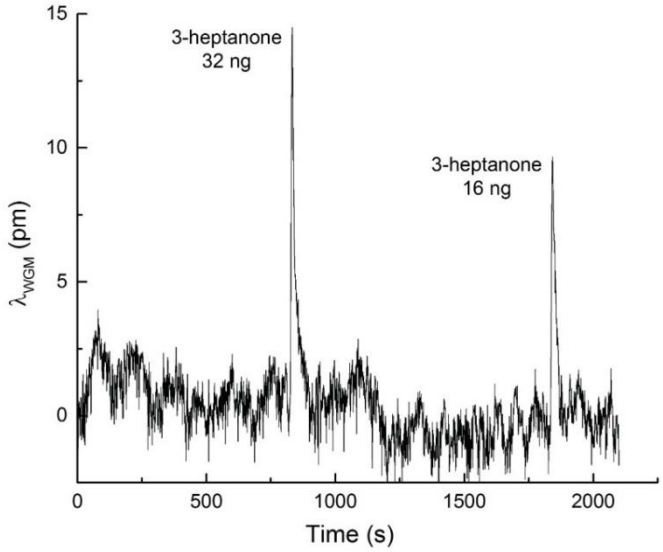

Figure 2.12 Responses to the test vapor 3-heptanone from the TEG-MPN coated μOFRR sensor as a GC detector. Helium at 1.2 mL/min was used as carrier gas. The 100-μL gas tight syringe injection split ratio was 80:1. Masses injected were determined on the basis of headspace concentrations assuming a vapor pressure of 0.56 kPa for 3-heptanone.

The TEG coated μOFRR was tested as a GC detector. The results are shown in Figure 2.12. Since the flow rate was so low and the separation was performed at ambient temperature, the peak widths were quite broad: full width at half height values were ~11sec. Unfortunately, there was no time to study the effect of flow rate on responses to explore whether sorption dynamics into the TEG-MPN film would affect peak shape and peak area, as observed previously.[21] The sensitivity was about 0.45 pm/ng and the single-point estimate of the limit of detection (LOD) from the first peak in Figure 2.12, yielded a conservative value of ~ 6 ng, which is excellent. In fact, it is consistent with LOD values we reported previously for more volatile, less polar vapors in the first TEG-coated μOFRR experiments.[21] Since TEG is a polar moiety and 3-heptanone is both less volatile and more polar than other tested vapors, it should (and did) give a larger response. Additional sensitivity can be ascribed to improvements in coupling efficiency we realized by use of thinner optical fiber.

2.3.5 CTAB-NR tests

From the experiments directed at determining the effect of different concentrations of the CTAB-NR deposited on the device interior walls, we found that we could observe WGM resonances when the concentration of the solution was 0.0005 μg/mL, 0.005 μg/mL, 0.05 μg/mL, and 0.5 μg/mL. However, only when the concentration was 0.5 μg/mL, did the μOFRR respond to exposure to vapors. The response signal was recorded by video camera, but could not be imported for presentation. Resonance wavelength shifts were observed when the device was exposed to benzene, acetone, and toluene. Further work is needed to evaluate sensitivity, but we are optimistic that this material, or a similarly sized NR with a non-water-soluble ligand, will be useful because its LSPR maximum is expected to be in a spectral range where inexpensive tunable lasers are available. This bodes well for incorporating the μOFRR into a portable or wearable μGC.

2.4 Conclusions

On the basis of the results of this study, we conclude that the MPN-coated μOFRR sensor technology continues to show great promise as a μGC detector, but that further work is needed to resolve some critical questions and challenges. Optical transmission measurements on treated glass substrates revealed that the changes in absorbance accompanying vapor sorption in the vicinity of the LSPR maximum for a given MPN film differed greatly among most of the test vapor for one material (C8-MPN) but not for the other two (TEG-MPN and EOE-MPN). However, problems with obtaining reproducible results from different films of the same material or different regions of the same film were encountered, suggesting that reflectance variations arising from morphological non-uniformities represent a significant impediment to reliability. Sensitivity was low by this method as well. Both of these findings are consistent with what had been shown in previous studies in our lab. These confirmatory experiments thus were valuable but our attempts to resolve these problems were unsuccessful. We would point out that it is not clear to what extent these problems would translate to the μOFRR platform, but skepticism seems warranted.

We showed that the MPN-coated μOFRR sensor we assembled here could provide rapid and reversible responses to VOCs. In addition, the sensitivity was consistent with previously reported values, which indicates that the fabrication, handling, and system integration techniques we have developed are reliable. The incorporation of on-chip fluidic channels minimizes the dead space along the flow path and would facilitate the integration into GC/μGC systems. Even though vapor sensing was demonstrated with the NR-coated μOFRR, no quantitative data were collected. Further characterization of MPN-coated and NR-coated μOFRR sensors for VOC sensing with 1550- and 780-nm tunable laser systems is warranted and shows promise for demonstrating selective, single-sensor, multi-variable detection.

2.5 References

1. J. L. Perkins, *Modern Industrial Hygiene, Recognition and Evaluation of Chemical Agents*, Wiley, USA, 1997.
2. C.-J. Lu, W. H. Steinecker, W.-C. Tian, M. C. Oborny, J. M. Nichols, M. Agah, J. A. Potkay, H. K. Chan, J. Driscoll and R. D. Sacks, First-generation hybrid MEMS gas chromatograph, *Lab on a Chip*, 2005, **5**, 1123-1131.
3. P. R. Lewis, P. Manginell, D. R. Adkins, R. J. Kottenstette, D. R. Wheeler, S. S. Sokolowski, D. E. Trudell, J. E. Byrnes, M. Okandan and J. M. Bauer, Recent advancements in the gas-phase MicroChemLab, *IEEE Sensors Journal*, 2006, **6**, 784-795.
4. S. Zampolli, I. Elmi, F. Mancarella, P. Betti, E. Dalcanale, G. Cardinali and M. Severi, Real-time monitoring of sub-ppb concentrations of aromatic volatiles with a MEMS-enabled miniaturized gas-chromatograph, *Sensors and Actuators B: Chemical*, 2009, **141**, 322-328.
5. S. K. Kim, D. R. Burris, H. Chang, J. Bryant-Genevier and E. T. Zellers, Microfabricated gas chromatograph for on-site determination of trichloroethylene in indoor air arising from vapor intrusion. 1. Field evaluation, *Environmental science & technology*, 2012, **46**, 6065-6072.
6. W. R. Collin, G. Serrano, L. K. Wright, H. Chang, N. s. Nuñovero and E. T. Zellers, Microfabricated gas chromatograph for rapid, trace-level determinations of gas-phase explosive marker compounds, *Analytical chemistry*, 2013, **86**, 655-663.
7. J. Wang, J. Bryant-Genevier, N. Nuñovero, C. Zhang, B. Kraay, C. Zhan, K. Scholten, R. Nidetz, S. Buggaveeti and E. T. Zellers, Compact prototype microfabricated gas chromatographic analyzer for autonomous determinations of VOC mixtures at typical workplace concentrations, *Microsystems & Nanoengineering*, 2018, **4**, 17101.
8. S. K. Kim, H. Chang and E. T. Zellers, Microfabricated gas chromatograph for the selective determination of trichloroethylene vapor at sub-parts-per-billion concentrations in complex mixtures, *Analytical chemistry*, 2011, **83**, 7198-7206.
9. G. Serrano, D. Paul, S.-J. Kim, K. Kurabayashi and E. T. Zellers, Comprehensive two-dimensional gas chromatographic separations with a microfabricated thermal modulator, *Analytical chemistry*, 2012, **84**, 6973-6980.
10. W. R. Collin, A. Bondy, D. Paul, K. Kurabayashi and E. T. Zellers, μGC× μGC: comprehensive two-dimensional gas chromatographic separations with microfabricated components, *Analytical chemistry*, 2015, **87**, 1630-1637.
11. L. Wright and E. Zellers, A nanoparticle-coated chemiresistor array as a microscale gas chromatograph detector for explosive marker compounds: flow rate and temperature effects, *Analyst*, 2013, **138**, 6860-6868.

12. K. Scholten, X. Fan and E. T. Zellers, A microfabricated optofluidic ring resonator for sensitive, high-speed detection of volatile organic compounds, *Lab on a Chip*, 2014, **14**, 3873-3880.

13. J. Wang, N. Nuñovero, R. Nidetz, S. J. Peterson, B. M. Brookover, W. H. Steinecker and E. T. Zellers, Belt-Mounted Micro-Gas-Chromatograph Prototype for Determining Personal Exposures to Volatile-Organic-Compound Mixture Components, *Analytical chemistry*, 2019, **91**, 4747-4754.

14. K. Scholten, L. K. Wright and E. T. Zellers, Vapor discrimination with single-and multitransducer arrays of nanoparticle-coated chemiresistors and resonators, *IEEE Sensors Journal*, 2013, **13**, 2146-2154.

15. J. Bryant-Genevier, K. Scholten, S. K. Kim and E. T. Zellers, Multivariate curve resolution of co-eluting vapors from a gas chromatograph with microsensor array detector, *Sensors and Actuators B: Chemical*, 2014, **202**, 167-176.

16. F.-Y. Chen, W.-C. Chang, R.-S. Jian and C.-J. Lu, Novel gas chromatographic detector utilizing the localized surface plasmon resonance of a gold nanoparticle monolayer inside a glass capillary, *Analytical chemistry*, 2014, **86**, 5257-5264.

17. R. A. Potyrailo, M. Larsen and O. Riccobono, Detection of Individual Vapors and Their Mixtures Using a Selectivity-Tunable Three-Dimensional Network of Plasmonic Nanoparticles, *Angewandte Chemie International Edition*, 2013, **52**, 10360-10364.

18. Y. Sun and X. Fan, Analysis of ring resonators for chemical vapor sensor development, *Optics express*, 2008, **16**, 10254-10268.

19. Y. Sun, S. I. Shopova, G. Frye-Mason and X. Fan, Rapid chemical-vapor sensing using optofluidic ring resonators, *Optics letters*, 2008, **33**, 788-790.

20. K. Scholten, X. Fan and E. T. Zellers, Microfabricated optofluidic ring resonator structures, *Applied physics letters*, 2011, **99**, 141108.

21. K. Scholten, W. Collin, X. Fan and E. Zellers, Nanoparticle-coated micro-optofluidic ring resonator as a detector for microscale gas chromatographic vapor analysis, *Nanoscale*, 2015, **7**, 9282-9289.

22. A. Hierlemann, E. T. Zellers and A. J. Ricco, Use of linear solvation energy relationships for modeling responses from polymer-coated acoustic-wave vapor sensors, *Analytical chemistry*, 2001, **73**, 3458-3466.

23. K. C. Grabar, K. J. Allison, B. E. Baker, R. M. Bright, K. R. Brown, R. G. Freeman, A. P. Fox, C. D. Keating, M. D. Musick and M. J. Natan, Two-dimensional arrays of colloidal gold particles: a flexible approach to macroscopic metal surfaces, *Langmuir*, 1996, **12**, 2353-2361.

24. S. Liu, T. Zhu, R. Hu and Z. Liu, Evaporation-induced self-assembly of gold nanoparticles into a highly organized two-dimensional array, *Physical Chemistry Chemical Physics*, 2002, **4**, 6059-6062.

25. Y. Sun and Y. Xia, Increased sensitivity of surface plasmon resonance of gold nanoshells compared to that of gold solid colloids in response to environmental changes, *Analytical Chemistry*, 2002, **74**, 5297-5305.

26. M. D. Baaske, M. R. Foreman and F. Vollmer, Single-molecule nucleic acid interactions monitored on a label-free microcavity biosensor platform, *Nature nanotechnology*, 2014, **9**, 933.

Chapter 3

Microfabricated Passive Preconcentrator for μGC

3.1 Introduction

Gas chromatographic instrumentation employing Si-microfabricated analytical components (μGC) show great promise for near-real-time measurement of the composition of airborne mixtures of volatile and semi-volatile organic compounds (S/VOCs) at low power and in small packages. Such technology would facilitate worker exposure measurements, distributed process and pollution monitoring networks, point-of-care medical diagnostics, and numerous applications of interest to the intelligence community and the military. Reports of μGCs containing microfabricated devices for sample capture, injection, separation, and detection have appeared over the last decade or so,[1-12] and a resurgence of commercialization efforts related to such technologies is also apparent.[13-16]

Since preconcentration is necessary to detect the low concentrations of target vapors demanded in many applications, μGCs often incorporate (μ)preconcentrators containing one or more adsorbent material and an integrated heater and temperature sensor.[1-4,7-11,12] In such devices, the vapors in an air sample drawn through the device with a small pump are retained on the solid adsorbent(s) by non-bonding, physisorption interactions and subsequently thermally desorbed into a smaller volume of carrier gas, thereby increasing vapor concentrations and narrowing the injection band width prior to downstream separation and detection.[17-22]

Among the factors affecting performance are the adsorption capacities for the target vapors during sampling and the desorption rates, efficiencies, and band widths during transfer. All of these factors depend on the concentrations, volatilities, and functionalities of the S/VOC(s); the mass, functionality, porosity, and specific surface area of the adsorbent; and the flow rate of the air or carrier gas being drawn through the device during sampling or desorption/injection, respectively. Desorption is also affected by the heating rate and maximum temperature of the device.

Power efficiency is often integral to device design and operation. In most reported μGC prototypes, commercial diaphragm mini-pumps are used to capture air samples.[1,2,4-11] A typical average power consumed by such pumps is ~300 mW. For short-duration sampling, the energy consumed by the pump (i.e., 18 J/min) is a small fraction of the total energy per analysis (e.g., 2.2 kJ per 6-min analytical cycle for the belt-mounted μGC described in ref. 11). But, for sampling periods >0.5 hr, pumping starts to dominate the energy budget, and for battery-powered systems this may preclude applications requiring longer sampling times.

In a previous published study, my advisor led an effort to develop a so-called microfabricated passive preconcentrator-injector (μPPI) that collects vapors at known rates by molecular diffusion.[23] The μPPI chip had a top layer with a rectangular grid of vertical microchannels (apertures) through which vapors would diffuse, and a bottom layer with an adsorbent packed chamber, fluidic ports, and an integrated heater for desorbing vapors following a pre-set sampling period. Packed with < 1 mg of the graphitized carbon adsorbent, Carbopack X (C-X), the μPPI exhibited an effective diffusional sampling rate for toluene of ~9 mL/min, a high thermal desorption efficiency, and stable reliable heating over thousands of cycles.

Yet, the μPPI had several drawbacks. First, the sampling rate began to decline after only

30 min (i.e., above 1 µg of accumulated mass) of exposure to toluene at 1 ppm because of the limited adsorption capacity. In addition, an extremely high desorption flow rate of 50 mL/min was required to avoid losing part of the vapor sample to back diffusion through the aperture grid during thermal desorption. This desorption flow rate is much too high for µGC separations and most mini pumps. Furthermore, regardless of the flow rate, it was not possible to generate a narrow injection band with the µPPI due to its relatively large internal volume and large required sweep volume, and limitations on the heating rate that could be applied. Lastly, the fabrication process was rather cumbersome and device yields were low. Subsequent testing of the µPPI confirmed its low capacity and the inability to achieve sharp injections, such that downstream GC separations were severely compromised.[24]

The research described here is part of a larger project concerned with developing a so-called microfabricated collector-injector (µCOIN) that could serve as a front-end of any µGC for S/VOC mixture analysis. As conceived, the µCOIN would consist of two integrated devices, a *micro passive preconcentrator* (µPP) and a *micro progressively heated injector* (µPHI). The µPP, essentially a refinement of the µPPI, would passively collect vapors from the atmosphere and trap them onto one of two judiciously chosen internal adsorbents. It then would desorb them thermally and pass them as a broad, semi-concentrated bolus to the µPHI device in a 'few-mL' transfer volume under active flow provided by a downstream mini-pump. The µPHI device, in turn, would capture the vapors in the transferred sample and then inject the entire vapor mixture as a sharply focused (i.e., 'few µL') band to a downstream separation (micro)column at a low flow rate, thereby enabling efficient chromatographic resolution of mixture components and detection/identification by a downstream detector. Preliminary results on the µPP and µPHI have been presented in two conference proceedings papers.[25,26] Here we report only on the µPP.

The goals of this effort were defined in terms of several performance criteria described in the solicitation for the program funding.[27] Among the applications for which the μCOIN-μGC system was considered were monitoring for markers or 'signatures' of illicit activities (e.g., terrorist threats) as well as for environmental pollutants. Sampling periods of 0.5 to 24 hr, detectable concentrations as low as 0.05 mg/m^3, and deployment for several months of unattended operation on battery power, were among the goals.

For the purposes of this inaugural effort to design and characterize the first-generation μPP we focused on a relatively small set of target compounds of moderately low vapor pressure and tested them individually and in simple mixtures over time periods and concentration ranges that permitted the assessment of performance and factors affecting that performance.

Following descriptions of the materials and experimental methods employed, including device fabrication, we present the rationale for the design of the first-generation μPP device examined here in the context of the performance criteria listed above and others that were added. The results of initial thermogravimetric analyses (TGA) of the adsorbent materials are presented, followed by results of exposing the μPP to individual vapors and simple mixtures over a range of concentrations and time periods, and desorbing/transferring captured vapors. An emphasis is placed on documenting the sampling rates, capacities, and desorption (injection) efficiencies. Improvements over the predecessor μPPI device are discussed and then the implications of the results for the design of a second-generation μPP device are considered.

3.2 Background

The effective diffusional sampling rate of a passive sampling device, S_e (cm^3/s), by analogy with an actively pumped sampler flow rate, is the volume of contaminated air drawn into the device

per unit time. From Fick's first law:[28-30] $S_e = DA/L = m/(C_a t)$, where D is the vapor diffusion coefficient in air (cm^2/s), A is the cross-sectional area (cm^2) and L is the length (cm) of the diffusion path within the device, C_a is the air concentration of the ambient vapor ($\mu g/cm^3$), and m is the mass of vapor captured (µg) over time, t (s). It is assumed that the concentration of vapor at the surface of the adsorbent placed at the end of the diffusion path is zero, such that there is a linear concentration gradient from the ambient to the adsorbent. Since m is proportional to Ca, S_e is independent of C_a. By keeping $L/d > 2.5$, where d is the diameter of the inlet aperture, the effect of ambient air turbulence is minimized,[29] Fickian diffusion dominates mass transfer, and S_e should be independent of size for any given value of A/L.

The amount of vapor retained on the surface of a porous solid adsorbent at equilibrium determines the adsorption capacity, W_e, which is the ratio of the mass of adsorbed vapor to the mass of adsorbent at a given air concentration.[30,31] At concentrations where coverage is much less than a monolayer there is an excess of adsorption sites available, vapors with sufficient affinity for the adsorbent will be well-retained on the adsorbent surface, and the assumption of negligible vapor concentration at the surface of the adsorbent should be valid. Although W_e increases with concentration, the dependence of W_e on C_a is invariably a steadily decreasing function of C_a, consistent with a classical Type II (e.g., Langmuir) isotherm. [32,33] With further increases in C_a, W_e will reach a maximum, corresponding to monolayer coverage (occupancy) of adsorption sites on the solid.

Even at sub-monolayer coverage, weakly adsorbed vapors may partially desorb spontaneously. In the context of a passive vapor sampler such as the µPP, this could result in a reduction in the concentration gradient, redistribution across the adsorbent bed(s), or off-gassing following an initial exposure, any of which would cause a decrease in S_e. In practice, this might

occur as a function of time for a fixed vapor concentration, as a function concentration for a fixed sampling time, or as a function of competition for exposure to a mixture of vapors. Although some reduction in S_e may be tolerable, at some point quantitative analysis would be undermined.

At the conclusion of a given sampling period, thermal desorption and transfer of the captured vapors downstream (e.g., to the µPHI of the µCOIN in this case) requires active suction flow through the device. During this step, the temperature must be high enough to overcome the heat of adsorption for the vapor(s), and the transfer flow rate must be sufficient to overcome the back-diffusion caused by the heating process to avoid loss of the vapors back through the inlet aperture.

Table 3.1 Results of short-term performance tests of the µPP with 15 individual compounds.

Compound[a]	p_v (kPa)[b]	D (cm^2/s)[c]	C_o (mg/m^3)	S_e (mL/min)			0.5-hr uptake (ng)[g]
				Model[e]	Exper.	Ratio	
m-xylene	1.1	0.068	44	0.61	0.65	1.1	0.98
o-xylene	0.89	0.072	40	0.65	0.66	1.0	0.99
isoamyl acetate	0.75	0.068	15	0.61	0.57	0.93	0.86
cyclohexanone	0.58	0.078	23	0.70	0.64	0.91	0.96
CEES	0.45	0.074	36	0.67	0.67	1.0	1.0
DMMP	0.13	0.050	49	0.45	0.44	0.98	0.66
cyclohexanol	0.088	0.076	42	0.69	0.62	0.90	0.93
PFTBA	0.074	0.033	47	0.30	0.33	1.1	0.50
nitrobenzene	0.033	0.079	28	0.71	0.78	1.1	1.2
DIMP	0.037	0.028	17	0.25	0.21	0.84	0.32
DEMP	0.039	0.036	42	0.32	0.26	0.81	0.39
NMP	0.047	0.087	48	0.79	0.34[d]	0.43	0.51
DMSO	0.080	0.098	52	0.88	0.16[d]	0.18	0.29
1-butanol	0.93	0.087	198	0.49[f]	0.31	0.63	0.47
DMF	0.52	0.10	110	0.56[f]	0.41	0.73	0.62

[a] acronyms are defined as follows: CEES, chloroethylethyl sulfide; DMMP, dimethylmethylphosphonate; PFTBA, perfluorotributyl amine; NBZ, nitrobenzene; DIMP, diisopropylmethylphosphonate; DEMP, dimethylmethylphosphonate; NMP, N-methyl-2-pyrrolidione; DMSO, dimethylsulfoxide;,DMF, N,N-dimethylformamide; [b] at 25 °C from ref. 34; [c] at 25 °C from refs. 35-38 but for DEMP and DIMP please refer to Section A.8 of the Appendix; [d] thermal decomposition suspected – see text; [e] all values are initial S_e values assuming no penetration into the C-B bed except for n-butanol and DMF; [f] model was run assuming no trapping on C-B bed; [g] uptake mass for 0.5 hr exposure extrapolated to 0.05 mg/m^3 using experimental S_e values in this table.

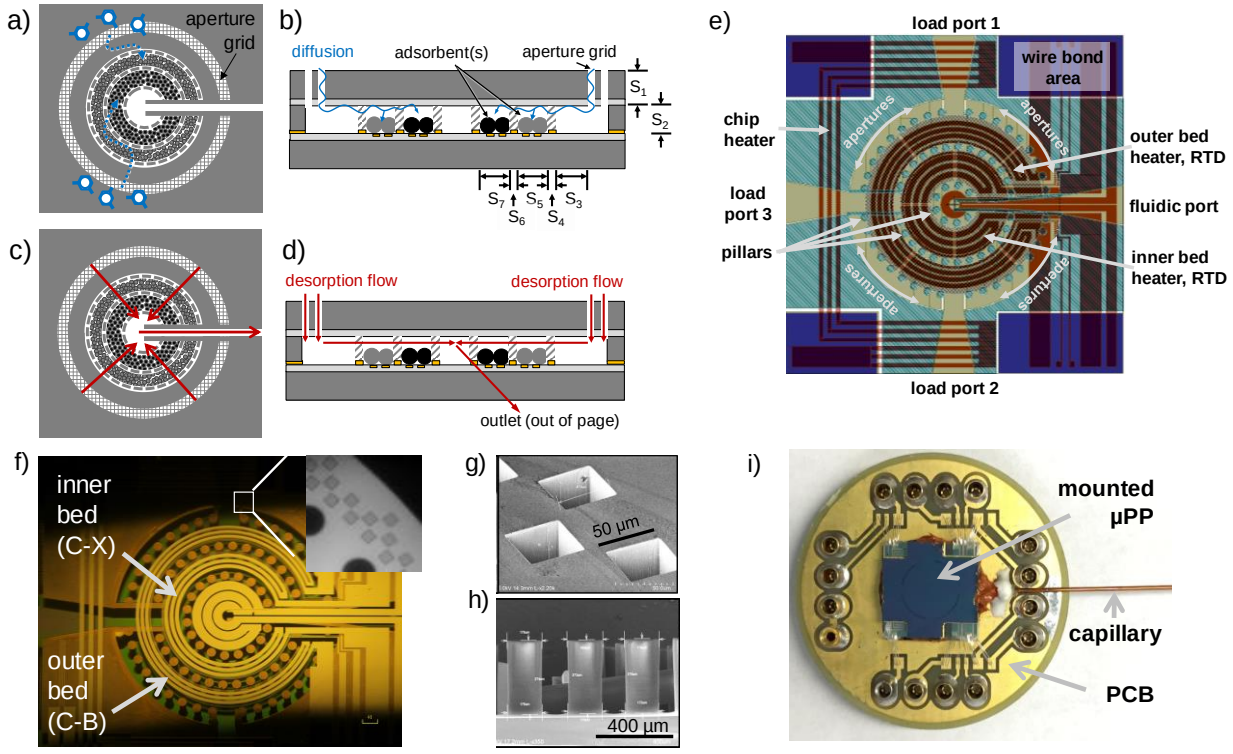

Figure 3.1 (a)-(d) Top and side view conceptual drawings of the µPP illustrating key features of the design and operation; A_i and L_i are the cross-sectional area and length of the formalized diffusion path segments (i = 1, 2, 3)used for modeling; (e) CAD layout for the µPP with key components labeled; (f) bottom view microscopic image of completed µPP -- inset is an IR image of a section of the periphery showing the apertures and bonding locations of the pillars; (g) SEM of a section of apertures; (h) SEM (side view) of adsorbent retention pillars; (i) PCB-mounted µPP chip (8 mm × 8 mm) with interconnecting capillary. Images and diagrams courtesy of R. Hower and J. Potkay (except for 3.1i).

3.3 Experimental

3.3.1 Materials

Test compounds and solvents were purchased from Acros/Fisher (Pittsburgh, PA) or Sigma–Aldrich/Fluka (Milwaulkee, WI) in > 90% purity (most >99%) and used as received. Table 3.1 lists the compounds tested, which span a p_v range of 0.033 (nitrobenzene) to 1.1 kPa (m-xylene). The graphitized carbon adsorbents, C-X and Carbopack B (C-B), were obtained from Supelco (Bellefonte, PA) and were manually sieved to isolate granules with nominal diameters

ranging from 224-250 µm. Silicon-on-insulator (SOI) wafers (4" diam.) with a 180 µm (Si) device layer, a 1.5µm buried oxide layer, and a 380 µm (Si) handle layer were obtained from University Wafer, Boston, MA, as were borofloat glass wafers (4" diam., 200 µm thick).

3.3.2 µPP description and fabrication summary

Figures 3.1a-d show top- and side-view conceptual diagrams of the µPP device during diffusional sampling (Figure 3.1a,b) and pumped/heated desorption/transfer (Figure 3.1c,d). Figure 3.1e shows the CAD layout drawing specifying the critical components/features. Each device was made from a top and bottom substrate. Deep reactive ion etching (DRIE) of the top silicon-on-insulator (SOI) substrate was used to form the critical features, including the aperture grid, adsorbent-retention pillars, adsorbent loading ports, and the fluidic transfer channel. Thin metal resistive heater films and co-located resistive temperature detectors (RTD) for thermal desorption of captured vapors were deposited on the bottom glass substrate. Section A.1 of the Appendix describes the details of the fabrication procedure, along with supporting images and diagrams (Figures A1-A3).

Each device chip measures ~ 8 mm × 8 mm (Figure 3.1e). Figure 3.1f is a photomicrograph of the µPP viewed from the glass underside. The inset is an IR image of a section of the periphery showing the apertures and the pillar locations. SEMs of the pillars and apertures are presented in Figure 3.1g and h, respectively. Figure 3.1i shows the µPP, with interconnecting capillary, mounted and wire-bonded to its PCB.

The µPP contains an array of apertures at the periphery of its circular outer boundary through which vapors diffuse to the interior of the device. Although designed to have dimensions of 50 × 50 µm, due to under-etching, the actual dimensions were 47 × 47 µm. Just within this ring

of apertures is the first annular adsorbent cavity, the boundaries of which are defined by cylindrical pillars (~180 µm o.d., spaced by 130 µm) that retain the adsorbent. This cavity was loaded with the lower-surface-area C-B. The two outer-bed fill ports are located at opposite sides of the annular cavity and comprise straight channels with tapered inlets formed in the top substrate. Concentrically internal to the C-B cavity is the inner cavity, the inner boundary of which is defined by a third ring of pillars. This cavity was filled with C-X. A single fill port for this cavity is located at 90 ° from the C-B fill ports. At the center of the device is an empty cavity (2 mm diameter) from which the fluidic port emanates and through which air is drawn during thermal desorption and transfer of preconcentrated vapor samples.

Lining the floor of each cavity are Ti/Pt thin-film resistive heaters and RTDs the origins and terminations of which are located at one of the four wire-bonding areas at the corners of the chip. The heater in the center of the chip and along the fluidic transfer channel were not used. An additional chip heater and RTD encircling µPP structure and intended for heating the chip outside of the active device area was also found to be unnecessary due to conductive heat transfer through the substrates.

3.3.3 µPCF

To perform analyses by GC-FID it was necessary for most tests to use a surrogate focuser device that could accept desorbed samples transferred from the µPP under suction flow provided by a mini-pump and inject them directly into the GC column under a positive pressure of carrier gas. For this purpose we used our previously developed µpreconcentrator-focuser (µPCF) which has been extensively characterized and used reliably in prototype µGC instruments.[11,20]

Details of the fabrication of the µPCF can be found elsewhere.[20] A photograph of the device

is provided in Figure A4. It has tandem adsorbent cavities containing ~2.3 mg each of C-X and C-B separated and retained within the chambers by pillars. An etched tee-junction at one end of the μPCF chip allows for vapor loading in one flow direction and desorption/injection in the other (i.e., with backflushing) by use of an integrated, thin-film heater on the backside operated under closed-loop control (see below).

The capture and desorption efficiencies of the μPCF were checked by a series of challenges with m-xylene and DEMP at various concentrations and at transfer flow rates of 5 and 10 mL/min. No evidence of breakthrough or residual vapor was detected.

3.3.4 Device filling, sealing, mounting

A ~25-cm segment of deactivated fused silica capillary (250 μm i.d.,) was inserted into the tapered outlet channel of the μPP and sealed with Duraseal (Cotronics Corp., New York, NY). The inner and outer cavities were loaded sequentially with ~780 μg of C-X and ~830 μg of C-B, respectively, by applying gentle suction to the outlet capillary and drawing the granules of each material in through the fill ports (Figure 3.1e and f). The device was weighed (±10 μg) before and after each adsorbent was loaded, and the extent of filling was also monitored visually. After filling and weighing each cavity, the corresponding fill port(s) was sealed with Duraseal and allowed to cure at room temperature overnight. As a check, the published packing densities of C-X and C-B (i.e., 0.58 and 0.43 g/cm^3, respectively, were multiplied by the respective adsorbent cavity areas and the average particle size. The resulting bed mass for C-B was nearly identical to what was measured, whereas the calculated C-X was 20% lower than what was measured.

The μPP was then anchored with epoxy (Hysol 1C, Henkel Corporation, Rocky Hill, CT) onto a custom printed circuit board (PCB) which had a square hole beneath the device for thermal

isolation from the PCB substrate. The capillary was also anchored with Hysol to the PCB to relieve stress on the junction with the device. The PCB surface was coated with a thin gold layer by the supplier to minimize adsorption of vapors during subsequent testing in the exposure chamber (described below). The bonding pads on the μPP device were electrically connected to the corresponding pads on the PCB by Al wire bonds.

The μPCF was filled, sealed, mounted and wirebonded on a separate custom PCB in a manner similar to that for the μPP using the same adsorbent materials.[11] The μPCF used three segments of ~15-cm deactivated fused silica capillary (250 μm i.d.,) to connect to the μPP and the mini-pump during sample transfer, and to a tank of compressed He carrier gas and the GC inlet during injection; a 6-port valve allowed loading in one direction and then desorption/injection with backflushing (see below). The voltage outputs from the RTDs of the μPP and μPCF were calibrated from 30 to 70 °C in the GC oven, and extrapolated to higher temperatures for purposes of controlling heating rates and maximum temperatures (see below).

3.3.5 Test system and exposure chamber

The system used to generate and confirm test atmosphere concentrations, expose the μPP, and collect and analyze the samples transferred from the μPP is described in Section A.2 and shown schematically in Figure A5 of the Appendix. House air, purified and dried with scrubbers, was passed through mass flow controllers to generate the dilution air flow. A portion of the same source of air was diverted and passed through a fritted bubbler containing the liquid test compound to generate a quasi-saturated stream of vapor and that was directed into the dilution air stream and through a downstream mixing chamber. A three-way solenoid valve was placed just upstream of the exposure chamber with one path leading to the chamber and the other back to the hood for venting. Upstream from the valve there was a tee to allow switching from test atmosphere to N_2

purge. The fraction of the test atmosphere directed to the stainless steel chamber housing the μPP (Figure A6, Appendix) was controlled to ~1 L/min, as measured downstream.

After passing through the exposure chamber, a portion of the atmosphere was collected by a sampling loop and injected into the GC-FID by a positive flow of N_2 for concentration confirmation. All downstream stainless-steel tubing or deactivated fused-silica capillary and connectors were wrapped with coil heaters, heater-embedded polymer pads (Omega Engineering, Norwalk, CT) or custom coil reinforced tubing (MicroLumen, Oldsmar, FL). Thermocouples were also installed at several points in the flow path. Lines were heated to 70 °C for tests with compounds where adsorption to surfaces was of concern.

Two 6-port valves (VICI-Valco, Houston, TX) in an ovenized enclosure were used to direct flow as needed for each step of the process. Analyses of test atmosphere concentrations and μPP samples transferred to (and injected from) the μPCF were performed with a bench scale GC-FID (6890, Agilent Technologies, Palo Alto, CA) that had been calibrated with liquid solutions of the S/VOCs tested.

3.3.6 Testing procedures

In a typical sampling test, the exposure chamber was purged with N_2 (or clean air) and a background sample was taken and injected via sampling loop into the GC-FID to ensure no residual vapor was present. Then, a blank was transferred from the heated μPP to the μPCF and analyzed (see below for conditions). This procedure was repeated as needed to obtain a clean blank chromatogram. Note: a persistent amount of background contamination was observed and is attributable to off-gassing from the Duraseal. Leak testing was conducted periodically with a helium leak detector and any leaks were sealed prior to testing.

Every few minutes, a portion of the test atmosphere collected by sampling loop was injected into the GC-FID for concentration confirmation. Once the exposure period was over, the chamber was purged with N_2 for at least 4 minutes to remove any vapor, and the mini-pump was activated to draw flow through the µPP transfer line at 5 mL/min through the µPCF. The µPP heaters were then activated and the µPP heated to 250 °C (or higher, see below) for 60 sec. Then the pump was turned off, and the µPP allowed to cool down without flow passing through it. Note: during sampling the transfer line emanating from the µPP was blocked using a termination in place of the mini-pump connection to the 6-port valve to avoid any inadvertent advective flow through the device.

Following the sample transfer, the 2nd 6-port valve was switched to pass carrier gas through the µPCF while it was heated to 250 °C for 60 sec to inject the transferred sample with backflushing into the GC inlet. For most tests, a series of three transfer/desorption cycles was sufficient to achieve complete transfer (peaks barely or not detectable).

Sampling rate calculations were based on the total mass detected from all transfers and injections. Assuming all of the collected sample was released/transferred ultimately, the desorption efficiency (*DE*) was calculated as the ratio of the first injected mass over the total injected mass.

For one series of tests with o-xylene a mini-photoionization detector (PID) was installed in line between the pump and µPP to examine the transferred peak width. A metering valve placed between the pump and PID (NovaPID, Nanova, Columbia, MO) was used to control the flow rate to 3 or 5 mL/min.

3.3.7 Thermogravimetric analysis (TGA)

A thermogravimetric analyzer (TGA, Pyris 1, Perkin Elmer, Waltham, MA) was used to measure vapor uptake, retention, and thermal desorption by C-X or C-B using samples loaded into the weighing pan of the TGA, suspended from the balance, and preconditioned at 250 °C under a flow of N_2 for >30 min. Details of the set-up and procedures are given in Section S3 of the Appendix.

3.3.8 Heater control, parameter adjustment, data acquisition, data analysis

A laptop computer running custom LabVIEW (Ver. 14.0, National Instruments, Austin, TX) programs was used to control the µPP and µPCF heaters. Operating parameter settings and control functions for each device were entered through a graphical user interface (GUI). Independent proportional-integral-derivative (PID) feedback loops were designed to control heating rates and temperatures via solid-state relays and the pulse-width modulation (PWM) settings of the generated signals. For each device, a separate 16-bit DAQ card (NI USB-6216 OEM and NI USB-6212, National Instruments) was used to record the PWM voltage applied to each heater at a sampling rate of 250 Hz.

The temperature profiles of the µPP heaters were characterized with the loaded µPP. Figure A7 (Section A.4, Appendix) shows a set of profiles for one heating sequence from the RTDs located adjacent to the heaters in the inner and outer adsorbent-bed cavities, as well as on the chip outside of the device. The heating rate was intentionally set at a modest value of ~ 50 °C/sec to reduce the likelihood of losses due to back diffusion through the aperture grid. The cavity heaters tracked each other closely and reached their maximum (T_{max}) of 250 °C within ~5 sec. The chip temperature increased at a lower rate and rose to a lower maximum temperature of 210 °C because

of conduction through the substrate (note: the chip heater was not used). This heating profile was highly reproducible and the device was heated hundreds of times without failure. Subsequent experiments using a maximum temperature of 275 °C were run to improve the *DE* of DEMP.

For heating the μPCF, an initial fast ramp of 400 °C s^{-1} was used to heat from ambient temperature to 100 °C, followed by a PWM ramp of 150 °C s^{-1} to 250 °C, which was maintained for 60 s to ensure that even the least volatile test compounds would be completely desorbed.[4,20,39] Injected samples were passed via a section of capillary to the FID or to the head of a capillary column for separation (where necessary) and then to the FID. For compounds with vapor pressures < 1 kPa, the transfer capillary was heated to 70 °C to avoid adsorptive broadening or losses.

The 6-port valves, interconnect heaters, and 3-way solenoid valve upstream of the chamber were actuated (switched on and off) manually. Chemstation® software controlled GC flow rates, temperatures, and oven temperature programming. Raw chromatogram traces were stored as text files and analyzed using OriginPro (Ver. 9.1, OriginLab, Northampton, MA) for peak integrations. Additional analyses and modeling were performed with Excel (Office 365, Microsoft, Redmond, WA).

The power and energy consumed by the μPP per analysis were estimated by taking the product of the voltage and current waveforms. For a typical 60-sec desorption at 250 °C these were 2 W and 120 J, respectively.

3.4 Results and Discussion

3.4.1 Design and operation

To rationalize the μPP design and operation, several factors were considered related to both the sampling function and desorption/transfer function, which were dependent on the S/VOCs.

Per above, for this initial study we limited the S/VOCs we pursued for quantitative sampling and transfer to those falling in the p_v range of 0.04 to 1.11 kPa to avoid problems with capture efficiency for more volatile compounds and desorption efficiency for less volatile compounds. Accordingly, we selected C-X and C-B adsorbent materials based on results from previous studies we had performed showing that they exhibited the right balance of capacity and desorption efficiency for compounds in this vapor pressure range to expect good performance. The C-B in the outer cavity, which is "upstream" with respect to the direction of diffusion during sampling, combines high capacity with high desorption efficiency for less volatile compounds. The inner cavity, which is "downstream", contains the higher-surface-area C-X which is better suited for trapping/desorbing more volatile compounds.[4,40] Both C-X and C-B are hydrophobic and stable in air at high temperatures, and have been used successfully in a number of μGC systems on which we have reported, including one tailored for explosive marker compounds.[4,10,11,20,40]

Based on results from the predecessor μPPI device,[23] we designed the cavities to hold roughly 800 μg each of C-X and C-B, assuming a packing density of ~0.4 g/cm^3.[41] Given that m-xylene is the most volatile compound we tested, and that capacity ideally varies inversely with vapor pressure, we expected the capacity of C-X for m-xylene to be ≥4 μg at 1 ppm (i.e., ~4 mg/m^3), based on results with toluene for the μPPI, and that it would vary directly with concentration. The capacity of C-B for m-xylene was expected to be less than that of C-X because of its 2.4-fold lower surface area, but would further increase the overall device capacity. Assuming capacity varies in proportion to specific surface area, then an equivalent mass of C-B would increase the capacity to 5.7 μg at 4 mg/m^3. Less volatile compounds would, in general, be expected to have even higher capacities, notwithstanding the countervailing influence of polarity for these non-polar adsorbents.

The number and size of the apertures were selected to give a nominal initial sampling rate, S_e, of ~0.66 mL/min for m-xylene (see below for further discussion). This value of S_e would allow collection of ~ 1 ng in 30 min at 50 µg/m^3, which was the sponsor-stipulated minimum sampling time and concentration for this project. A minimum mass of 0.5 ng was chosen as likely to be detectable by a downstream detector, such as a PID,[42] a MS[43] or a sensor array.[11] Furthermore, this would result in the collection of <50 ng in 24 hr at the same minimum concentration, which is well below the expected adsorption capacity for m-xylene and, thus, allows for the presence of other co-adsorbed compounds. Although no specific upper limit on concentration was established, we note that at the relatively high concentration of 10 mg/m^3 about 9.5 µg would be collected in 24 hr, which we speculated would not exceed the capacity of dual-adsorbent device (see below for discussion of capacity as a function of concentration).

The µPP was designed to address some of the shortcomings of the predecessor µPPI device. The radial µPP topology with the grid of sampling apertures at the periphery and two concentric adsorbent bed regions (C-B and C-X) offset inwardly (Figure 3.1) was adopted for several reasons. First, as mentioned above, during sampling the vapors would pass over the lower surface area C-B bed and then over the higher surface area C-X bed to expand the range of vapors efficiently sampled and transferred. Second, during desorption/transfer a more uniform distribution of swept flow would be generated laterally across the adsorbent beds to enhance capture efficiency and reduce the flow rate (see below) required to avoid losses from back diffusion. The offset of the aperture grid also addresses this factor. In the previous µPPI device the transfer flow was drawn predominantly from one side of the device through apertures located directly above the adsorbent bed, resulting in a highly non-uniform sweep flow. Another design change entailed reducing the sampling rate by reducing the number of apertures to allow longer

term sampling prior to exceeding the adsorption capacity, while still being able to collect sufficient mass over shorter time periods to address this goal. The 2-fold increase in total adsorbent mass over the predecessor μPPI device would increase capacity and/or the maximum duration of sampling at a constant rate. In addition, the simpler fabrication process and structure promised higher yield and manufacturability.

For the μPP, the diffusion path can be formally divided into a series of seven segments (Figure 3.1b): 1) vertically through the grid of apertures, 2) vertically beneath the apertures, 3) laterally to the first set of pillars, 4) laterally through the spaces between pillars, 5) laterally through the outer adsorbent bed, 6) laterally through the second set of pillars, and 7) laterally through the inner adsorbent bed. Each of these can be considered to have separate values of A_i and L_i, and, therefore separate segmental sampling rates, S_i. At steady state, they can be summed in a manner analogous to a series of electrical conductances. Further imposing the constraints of mass balance and constant D yields the following expression:[23]

$$S_e = \frac{D}{\sum \frac{L_i}{A_i}} = \frac{1}{\sum \frac{1}{S_i}} \qquad \text{Eq. 3.1}$$

Modeling various design variations showed that the net value of S_e is initially limited by the aperture grid geometry (i.e., S_1 has the lowest value among the segments) but that S_5 (and S_7, if applicable) decreases with time as the adsorbent becomes saturated and vapors must diffuse further (laterally) toward the center of the μPP. Depending on the sampling period and the adsorption capacity for the vapor, this may lead to a reduction in S_e over time. The model developed to describe this and the impact of this factor on S_e are addressed further below.

Power and energy efficiency were considered in the design but were deemed secondary to the fluidic factors. In fact, exploratory devices fabricated with the adsorbent heaters located on suspended membranes cracked upon heating and so were not pursued further. The average power and energy consumption values presented in Experimental Section (2 W and 120 J), assuming a 60-sec desorption/transfer period and a maximum temperature of 300 °C are quite low, which would facilitate battery-powered operation of any portable system in which the µPP were incorporated.

Table 3.2 provides some of the modeled dimensions and expected operating features of the µPP. We used m-xylene as the basis for initial modeling. It has a p_v value of 1.1 kPa, and so was the most volatile member of our test set. DEMP (p_v = 0.039 kPa), was also modeled as one of the least volatile test compounds. As shown in Table 3.1, their diffusion coefficients, 0.068 and 0.036 cm^2/s, respectively, differ by a factor of 1.9. The number and size of the apertures, along with the other diffusion path dimensions, gave modeled initial S_e values of 0.66 and 0.35 mL/min. respectively, so as to collect ≥ 0.5 ng at 50 µg/m^3 in 30 min at 25 °C.

The required desorption flow rates shown in Table 3.2 were calculated in a manner similar to the sampling rates, assuming that D increases as $(T_2/T_1)^{2.44}$ A temperature of 300 °C was assumed and the flow rate required to exceed that due to the 'reverse diffusion' of vapors driven off the adsorbent was calculated [$(573/298)^2 = 3.7$]. As shown, for the µPP this corresponds to 2.4 mL/min for m-xylene and 1.3 mL/min for DEMP. To account for advective flow and to add a safety factor, we settled on a desorption flow rate of 5 mL/min, which is easily achieved with a diaphragm mini-pump due to the low pressure drop (< 0.23 kPa). This corresponds to a time to sweep the cavity of < 240 ms. In fact, the highest T_2 value we used was 275 °C. Normally, one would prefer to back flush from higher to lower surface area adsorbent during desorption to avoid

band broadening, but this was not possible here and was also considered less critical because of the use of the μPHI.

Table 3.2 μPP design parameters and estimated operating parameters.

Inner bed od/id[a]	2.92/2.00 mm
Outer bed od/id[a]	4.50/3.28 mm
Aperture #/ dimensions[b]	237/50×50 μm
L1/L2/L3/L4/L5/L6/L7[c]	0.18/0.38/0.13/0.18/0.61/0.18/0.46 mm
A1/A2/A3/A4/A5/A6/A7[c]	0.59/2.4/3.7/1.5/2.9/0.99/1.8 mm^2
Response time: m-xylene/DEMP[d]	32/60 ms
Expected S_e: m-xylene/DEMP	0.66/0.35 mL/min
Min. desorp. flow: m-xylene/DEMP	2.4/1.3 mL/min

[a] *outer and inner diameters of the adsorbent bed cavities;* [b] *total number and lateral dimensions of grid of apertures (depth = 180 um);* [c] *refer to Figure 3.1b (A5 and A7 are the average values across the adsorbent cavities assuming diffusion occur through the adsorbent beds);* [d] *this is the time to reach steady state concentration at the start of the outer adsorbent cavity (i.e., the time to diffuse through segments S1-S4).*

3.4.2 TGA Mass Uptake, Offgassing, and Desorption Efficiency

Section A.6 of the Appendix presents the initial TGA results. Figure A8 shows the adsorption isotherm of m-xylene with C-X, which we could fit quite well to a Langmuir model; W_e increases with concentration but at a steadily decreasing rate. Values of W_e ranged from ~2,400 μg/g at 0.9 mg/m^3 to ~61,000 μg/g at 1,300 mg/m^3. Additional tests with C-X for other aromatic and aliphatic hydrocarbons (i.e., toluene, m-xylene, 1,2,4-trimethylbenzene and n-decane) at single concentrations of 4-6 mg/m^3 gave the expected linear dependence of W_e on p_v^{-1} as depicted in Figure A9. The corresponding data for C-B were not collected.

In a separate study of C-B adsorption capacity, conventional breakthrough tests were run with C-B or C-X packed in a metal tube continuously exposed to each of several individual test vapors at a single concentration.[45] Measured breakthrough masses, which should be proportional

to W_e according to the Wheeler Model, gave the following relative values: 1.0, 0.33, 0.92, 1.3, and 2.0 for m-xylene, DMMP, DEMP, DIMP, and NBZ, respectively. For DMMP, the breakthrough mass with C-X was also measured, and the ratio of breakthrough masses on C-X and C-B was 2.9 at the same concentration. Applying this ratio to the W_e values of m-xylene on C-X determined by TGA afforded estimates of W_e on C-B for m-xylene. Combining this with the ratios listed above, it was possible to estimate W_e on C-B for the other vapors. Similarly, tests of n-butanol with C-B showed immediate breakthrough, whereas with C-X the breakthrough mass was short but measurable, thereby permitting an estimate of W_e. The estimates of W_e were used in the modeling discussed further below.

Figure 3.2 shows the results of separate TGA tests involving exposure of C-X (2.9 mg, Figure 3.2a) and C-B (2.9 mg, Figure 3.2b) to m-xylene vapor. For C-X, exposure to 65 mg/m^3 for 100 min resulted in a mass uptake of 24 µg (8,300 µg/g). The linear uptake over time was consistent with (unrestricted) adsorption well below the W_e value of ~38,000 µg/g at this concentration (see Figure A8). The TGA sample was then purged with N_2 for 120 min at ambient temperature and there was no evidence of any off-gassing, as expected. Heating to 250 °C resulted in desorption of the m-xylene and recovery of the baseline with only minor drift.

The same test with C-B at a slightly higher concentration of m-xylene (i.e., 78 mg/m^3) gave a similar linear uptake of mass over the shorter exposure period of 50 min and an uptake of ~15 µg (5,200 µg/g), which is also below the W_e value of ~14,000 µg/g at this concentration extrapolated from the previous measurement at a lower concentration. In this case, however, the subsequent N_2 purge at ambient temperature resulted in a loss of 2.5 µg (17%) over 120 min from off-gassing. This portended a potential loss of vapor from the µPP during periods of non-exposure. Thermal desorption led to recovery of the baseline.

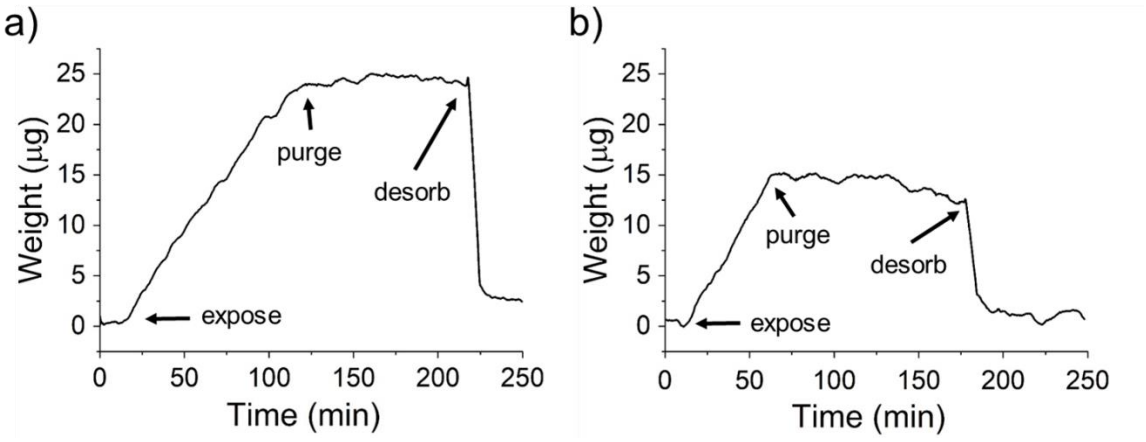

Figure 3.2 Results of TGA(exposure, purge, and desorption): (a) 2.9 mg C-X was exposed to 60 mg/m^3 of m-xylene for 100 min and N_2 for 120 min, followed by thermal desorption at 250 °C; (b) 2.9 mg C-B was exposed to 78 mg/m^3 of m-xylene for 60 min and N_2 for 120 min, followed by thermal desorption at 250 °C. Note the loss of mass during ambient-temperature purge of C-B.

3.4.3 µPP desorption/transfer conditions

To establish baseline operating conditions, exposure of the µPP to m-xylene in the test chamber at modest concentrations (~ 44 mg/m^3) over 0.25 hr was followed by desorption at 5 and 10 mL/min at 250 °C for 60 sec. These conditions were based on previous studies with the µPCF.[20] Following the initial desorption/transfer, two additional desorption/transfer steps were run to check for residual vapor. Desorption efficiency (DE) values were > 96% in all cases and were consistent among replicate tests (RSD = 4%).

For one series of tests a mini-PID inserted between the µPP and the mini-pump. As shown in Figure A10 (Section A.7, Appendix) for transferred masses of 23-25 ng (i.e., 12 mg/m^3 exposure), the desorption profile was asymmetric, but all of the m-xylene was transferred within ~30 sec at 250 °C at both 3 and 5 mL/min.

Desorption/transfer tests were then run with DMMP and DEMP, which are less volatile than m-xylene but also more polar. Results for DMMP, for different flow rates and transfer times,

showed that for captured masses of 160-200 ng (0.25-hr exposure to 24-30 mg/m^3) the DE was 99% at 5 mL/min for a T_{max} of 250 °C for 60 sec (see Table A2, Appendix). For DEMP, under the same conditions the DE value was only 85%. Increasing T_{max} to 275 °C improved the DE to 94%. (see Table A3, Appendix). Regardless, the effective sampling rate did not change.

To explore the potential loss of capture vapors during periods of non-exposure, tests were run with o-xylene, DMMP, and DEMP involving an initial exposure followed by either a 4-min or 60-min purge at ambient temperature prior to desorption and transfer. The experimental S_e value was used as the evaluation metric. For o-xylene, consistent with the TGA results for C-B, there was a 6% reduction in S_e. For DMMP there was a 19% reduction, and for DEMP there was no reduction. Results are compiled in Table A4 (Appendix). Surprisingly, the DMMP had the greatest apparent loss of mass from off-gassing despite its vapor pressure being much lower than that of o-xylene. Clearly, the DMMP and, to a lesser extent, o-xylene, are only weakly adsorbed on the C-B, and can spontaneously desorb at room temperature to a small but significant extent, and be lost from the sample.

3.4.4 Sampling rate stability: concentration

The next series of experiments explored the consistency of S_e values for o-xylene over a range of concentrations for a fixed, short exposure period of 0.25 hr. As shown in Figure 3.3, the experimental S_e values remained within 8% of the starting value over a concentration range of 0.6 to 1,500 mg/m^3, and a corresponding mass uptake range of 6 to 14,000 ng. As discussed further below, modeling suggests that at 1500 mg/m^3 the C-B bed becomes saturated within ~23 min and the o-xylene penetrates into the C-X bed. Remarkably, the DE values remained high throughout (i.e., > 96%).

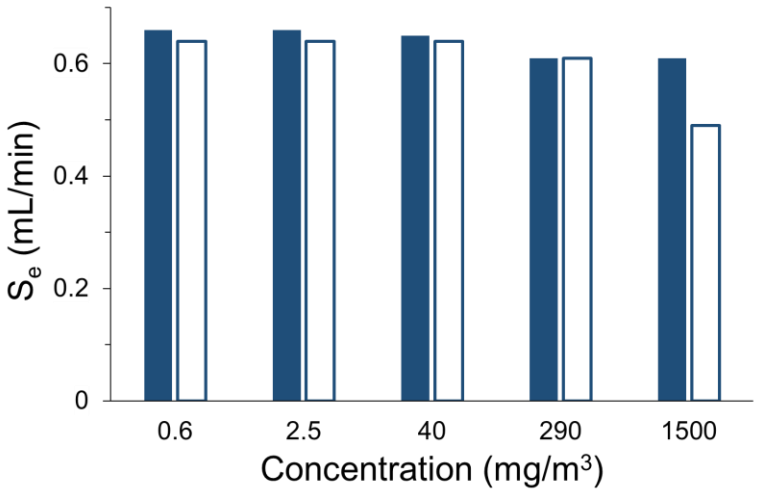

Figure 3.3 Plot of measured (filled) and modeled (unfilled) S_e values for o-xylene as a function of concentration (0.25-hr samples). The collected mass ranged from 6.1 to 14 µg and DE values were > 96%. There is < 8% reduction in sampling rate over a 2,500-fold concentration range. Agreement between experimental and modeled S_e values is within 3%, except at 1500 mg/m^3 where the modeled underestimates the observed S_e by 19%.

Over the course of the study, other vapors were tested over more modest concentration ranges with no apparent change in S_e values. For example, the S_e value of 0.25 mL/min for DEMP did not change between 1.4 and 87 mg/m^3, and that of DMMP (i.e., 0.44 mL/min) did not change between 3.2 and 49 mg/m^3.

3.4.5 Sampling rate stability: duration

Two series of experiments were run to assess the consistency of S_e over discrete time periods ranging from 0.25 to 24 hr. Results are summarized in Figures 3.4 and 3.5 for DEMP and o-xylene, respectively. For exposure to 1.4 mg/m^3 of DEMP (except for 0.25-hr sample at 55 mg/m^3), S_e remained constant up to 4 hr, decreased by 8% for the 12-hr sample, and decreased by 23% for the 24-hr sampling period (both relative to the initial 0.25-hr sample). The range of

collected (transferred) masses was 25 to 400 ng (i.e., 16-fold), and DE values were > 83% at 250 °C in all cases and did not vary with the uptake mass.

For o-xylene, S_e decreased steadily over time: within the first 4 hr it decreased by up to 15% and for the 24-hr sample it decreased by 30% (relative to the initial 0.25-hr sample). Note that the data shown in Figure 3.5 for the 0.5- and 1-hr samples were collected after the other data were collected and entailed exposures at much higher concentrations (124 mg/m^3 in both cases). Despite this, the *Se* values were consistent with those collected that the lower average concentration of ~3.5 mg/m^3 used in the other tests. The range of collected masses was from 25 to 4300 ng (i.e., 172-fold). DE values were > 97% in all cases. This shows that 24 hr sampling is feasible with the μPP with only a small reduction in S_e. The modeling presented in the next section accounts for this reduction.

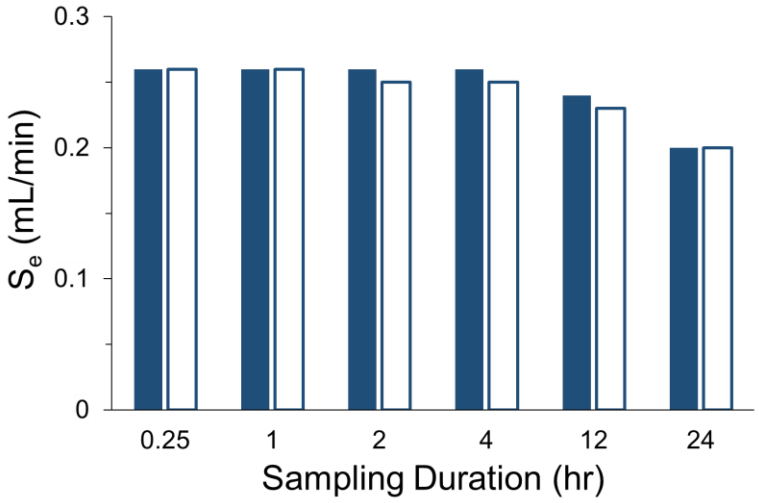

Figure 3.4 Plot of measured (filled) and modeled (unfilled) S_e values for DEMP as a function of sample duration. The challenge concentration was 1.4 mg/m^3 except for the 0.25-hr test (55 mg/ m^3). Note that S_e is constant out to 4 hr, decreases by 8% for the 12-hr sample, and by 23% for the 24-hr sample. The range of transferred masses was from 25 ng to 400 ng, and DE values were > 83% in all cases. Agreement between modeled and experimental values is within 4%.

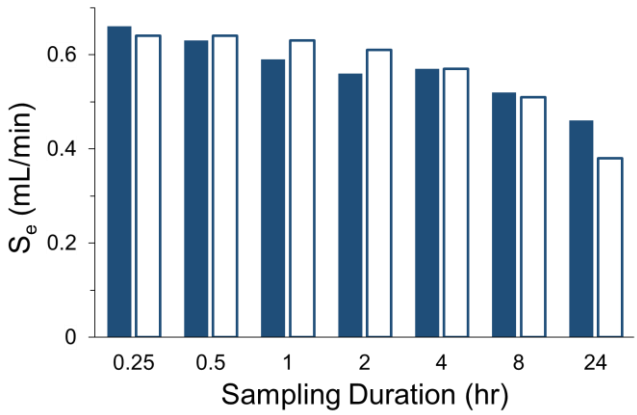

Figure 3.5 Plot of measured (filled) and modeled (unfilled) S_e values for o-xylene as a function of sample duration. The challenge concentration was 3.5 mg/m^3 except for the 0.5-hr and 1-hr tests (124 mg/m^3). Note that S_e decreases by 21% for the 8-hr sample, and by 30% for the 24-hr sample. The range of transferred masses was from 25 ng to 4,300 ng, and DE values were > 97% in all cases. Agreement between modeled and experimental values is within 8%, except for the 24-hr test where the modeled value is 18% too low.

3.4.6 Modeling of S_e

As stated above, to model S_e for a given compound, we formally divided the diffusion path into a series of segments as shown in Figure 3.1b. Table 3.2 gives the diffusional path length, L_i, and cross section area, A_i, for each segment i. Detailed descriptions of the segments are provided in Section A.7 of the Appendix. Note that A_1 in Table 3.2 assumed apertures with lateral dimensions of 50 × 50 μm. In the fabricated devices, these dimensions were actually 47 ×47 μm, and A_1 is therefore 0.52 mm^2. Here we summarize the salient features of the model we have developed and then compare modeled Se values to the experimental values shown in Figures 3.3-3.5. Details are presented in Section A.7 of the Appendix.

Eq. 3.1 expresses S_e as a function of the sampling rates, S_1-S_7, in each of the respective segments, S1-S7. The response time, which we define as the time required to establish steady-state conditions at the outer edge of the outer adsorbent bed, was estimated by first dividing the volume of each segment S1-S4 by its modeled S_i value (= DA_i/L_i), and then summing the resulting time

values. Response times will differ for every compound; for o-xylene and DEMP, they are 30 and 60 msec, respectively, and the largest value among the tested compounds is 77 msec (DIMP) (see Table A5, Appendix). Given how rapidly steady-state is established, we refer to this as the "time 0" S_e value in the next section below.

Implicit assumptions in Eq. 3.1 are that, once steady state is established, all of the S_i values are constant and that all of the vapor mass transferred into the device is conserved. If S_i in any segment changes, then it will have a commensurate effect on S_e. Importantly, Eq.3.1 gives the *instantaneous* S_e at a certain point in time. If S_e changes with time, then a time-averaged S_e value over the duration of the sampling period would be observed experimentally. Accordingly, the corresponding modeled value must also be averaged over time.

For the μPP, the sampling rate can change in S5 and S7; as sampling progresses the vapor gradually penetrates S5 first and then (possibly) S7. Focusing on S5, the model accounts for the changes in the radial length and cross-sectional area over a defined sampling period due to gradual saturation of the adsorbent over time. Mass transport through the adsorbent bed is impeded by diffusion of the vapor into the pores of adsorbent particles and by adsorption (retention) of the vapor on the adsorbent. The latter can be expressed as a function of the adsorption capacity, W_e, and the former by a D value that accounts for the contribution of Knudsen-like transport within the porous solid. That is, the D_5 value in S5 (and D_7 in S7) should be lower than that in other segments where Fickian diffusion through air occurs.

Section A.7 of the Appendix provides the steps involved in the approach we have taken to such modeling. Changes in the radial length and cross-sectional area in S5 (and S7) over time are portrayed in terms of the device dimensions and the degree of saturation of the adsorbent bed(s), which is a function of the mass uptake over time, the challenge concentration, and the applicable

value of W_e for the compound (and adsorbent) under consideration. Values of D_5 must be determined empirically, in this case by use of the experimental data presented in Figures 3.4 and 3.5.

The model was developed and applied first to the data in Figures 3.4 and 3.5 concerned with the change in S_e over time. The gradual reduction in S_e for DEMP and o-xylene were successfully modeled. For DEMP, the *D* value presented in Table 3.1 led to an initial modeled value of *Se* that was about 20% higher than observed, but the trend in the modeled Se values over time, which relies on the value of D_5 determined empirically, were consistent with trends in the experimental values. For the modeled values in Figure 3.4, we adjusted the initial (time-zero) S_e value to match the experimental t=0 Se value, so the agreement between modeled and experimental trends was more evident.

As shown, the agreement between modeled and experimental values is generally good; i.e., within 4% for DEMP and within 8% for o-xylene, with the exception of the 24-hr sample for o-xylene, where the model underestimates S_e by 18%. This negative error may be attributable, in part, to an underestimate in the assumed value of W_e for which there is considerable uncertainty at this high concentration (see Figure A8, Appendix). The fact that the model overestimates slightly the S_e values for o-xylene from 0.5-2 hr is attributed to weak adsorption leading to either a finite vapor concentration at the adsorbent surface and consequent reduction in the concentration gradient that drives the sampling rate or to off-gassing (i.e., loss). This would tend to subside with further penetration into the device.

For both compounds, the model indicates penetration into the C-X bed; for DEMP at 1.4 mg/m^3, this occurs after 1426 min and for o-xylene at 3.5 mg/m^3 it occurs after 820 min (i.e., ~14 hr). For o-xylene at 1500 mg/m^3 there is no penetration into the C-X bed over the 0.25 hr time

period. Subsequent penetration into the C-X bed was modeled assuming the same values of D5 as in the C-B, but using different values of *We* (Table A1, Appendix). In no cases were these vapors expected to penetrate through the C-X bed.

In summary, this model has a good foundation in the physicochemical processes occurring within the μPP. To model S_e values over time for untested compounds requires the Fickian D value, the vapor concentration, and the W_e value on C-B/C-X at the exposure concentration. Estimates of D_5 and D_7 are also required. For the latter, we assume that the ratio of D_5 value to Fickian D value for the untested compound is the same as the ratio of optimized D_5 value to Fickian D value for o-xylene (discussed in Section A.7 of the Appendix).

3.4.7 Sampling rates for other compounds

The μPP device was exposed to additional compounds individually for 0.25 hr at modest concentrations of 15 to 200 mg/m^3 to evaluate their S_e values. Results, summarized in Table 3.1, show that the range of experimental sampling rates spans from 0.16 mL/min (DMSO) to 0.78 mL/min (NBZ); a 4.9-fold range. The reported values are representative of replicate determinations; for all but one compound (i.e., NMP), the S_e values were quite reproducible among separate tests. For example, replicate samples of m-xylene (300 mg/m^3, n = 3) had an average S_e of 0.65 mL/min with a relative standard deviation (RSD) of 4%. For DIMP, S_e values were all determined from mixtures with other compounds, but were consistent across three runs (RSD < 3%). DE values for most compounds were > 90% with the exceptions of DEMP and NMP whose DE values were 85% and 87%, respectively.

The modeled values listed in Table 3.1 were calculated assuming no penetration into the C-B bed (i.e., at t = 0 min). As a check on comparability, those compounds for which estimates

We on C-B could be made were modeled at t = 0 and t = 0.25 hr. This included m-xylene, o-xylene, DMMP, DEMP, DIMP, and NBZ. In all cases the *Se* values at the two time points differed by < 2%. Hence, only the former values are reported in Table 3.1. For n-butanol, evidence was available to indicate no significant adsorption on C-B,[45] so the modeled S_e value assumes that steady state was established at the outer edge of the C-X bed (segment 7). Although similar evidence was not available for DMF, the experimental S_e value would suggest similar behavior, so the same assumption was made in calculating the modeled *Se* value for DMF.

Comparing experimental to modeled S_e values, there was generally good agreement. For the first nine compounds listed in Table 3.1 (i.e., m-xylene to NBZ), the ratio of modeled to experimental S_e values ranged from 0.90 to 1.1. For the remaining six compounds, the modeled values overestimated the experimental values by > 15%. For DEMP and DIMP, we suspect that the *D* values may be in error, since they were calculated using an expression/approach that has not been validated. For NMP and DMSO there is evidence in the literature to suggest that thermal decomposition occurs at > 260 and 190 °C, respectively, and thus could be occurring either in the μPP or μPCF.[46,47] Interestingly, however, the DMSO results were quite reproducible among four replicate trials (RSD < 6%).

Examination of the GC traces from the tests with these compounds did not reveal any residual peaks that might have been decomposition products. We conclude that DMSO can be sampled and transferred reliably, despite the apparent partial decomposition, but that NMP cannot.

The modeled S_e values for n-butanol and DMF also overestimated the experimental values by considerable margins. The most likely explanation is that both of these compounds penetrate the C-X bed to some extent even over the short exposure period tested. For n-butanol, this is supported by the study cited above, which showed a relatively small breakthrough mass with a C-

X packed adsorbent tube, and the rather low value of W_e we derived from that data. Therefore, the S_e value could be reduced by penetration into the C-X bed. The initial modeled S_e value (i.e., at t = 0 min) of n-butanol is 0.49 mL/min. Applying our model, the n-butanol is expected to saturate the C-X bed within 10 min of exposure at the challenge concentration of 198 mg/m^3. Assuming no further uptake over the ensuing 5 min, and no loss due to off-gassing, the modeled S_e value would be 0.28 mL/min. This is within 10% of the experimental S_e of 0.31 mL/min reported in Table 3.1. Although no data on DMF capacity of C-X could be found, it is reasonable to speculate that a similar phenomenon could explain its low experimental *Se* value.

The last column in Table 3.1 presents the mass of each compound that would be collected from a 0.5-hr sample at a concentration of 0.05 mg/m^3, assuming that the experimental S_e value shown would apply to this low concentration. Recall, that we designed the μPP to collect ≥ 0.5 ng under this scenario. As shown, for 11 of the 15 compounds, this criterion is met. Exceptions would require just an additional 2 to 26 min to collect the stipulated mass (note: per above, NMP could not be reliably sampled and transferred due to thermal decomposition).

3.4.8 Mixtures

Tests with mixtures of vapors were performed to explore whether competitive adsorption among different compounds might lead to displacement of one compound by another. o-Xylene and DEMP, which are both captured in the C-B bed but differ significantly in volatility and polarity, were chosen for these experiments. Observed S_e values were used as an indirect measure of any loss of vapor. Individual exposures were 0.25 hr and mixture exposures were 0.5 hr in duration. Results are summarized in Figure 3.6 and 3.7 (and Tables A6 and A7, Appendix).

Individual exposures to ~ 45 mg/m^3 each of o-xylene and DEMP resulted in uptake masses of 440 and 190 ng, respectively, and yielded S_e values of 0.69 and 0.26 mL/min, respectively, in close agreement with the values in Table 3.1. Exposure to a binary mixture of o-xylene (360 mg/m^3) and DEMP (87 mg/m^3) resulted in uptake masses of 7,500 and 660 ng, respectively, with virtually no change in the S_e values. A follow-up test with three additional compounds added to a mixture of these two compounds, also had no effect on the S_e values obtained for o-xylene and DEMP. For the latter mixture, all DE values were > 88%. Finally, exposure to a mixture of eight compounds yielded the S_e values shown in the chromatogram presented in Figure 3.7, all eight of which agree closely with the values in Table 3.1 (and Figure 3.6).

This confirms that the μPP has sufficient capacity to avoid losses due to displacement among competing vapors. However, if any displacement were to have occurred it could merely have caused vapors to diffuse further into the device where they would be trapped on the higher surface area C-X adsorbent. Some evidence for this is found in the fact that the DE values for the DEMP and DIMP in the latter experiment were reduced somewhat (80-90%) compared to individual or less complex mixture exposures.

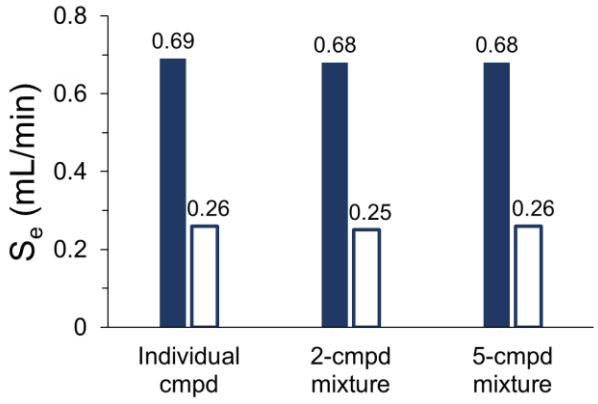

Figure 3.6 S_e values of o-xylene (filled) and DEMP (unfilled) exposed for 0.5 hr individually, as a binary mixture (see text for concentrations), and as a mixture with DMSO (140 mg/m^3), DIMP (19 mg/m^3), and NMP (8 mg/m^3). For the latter, the o-xylene and DEMP concentrations were 110 and 14 mg/m^3, respectively. Analysis was by GC-FID.

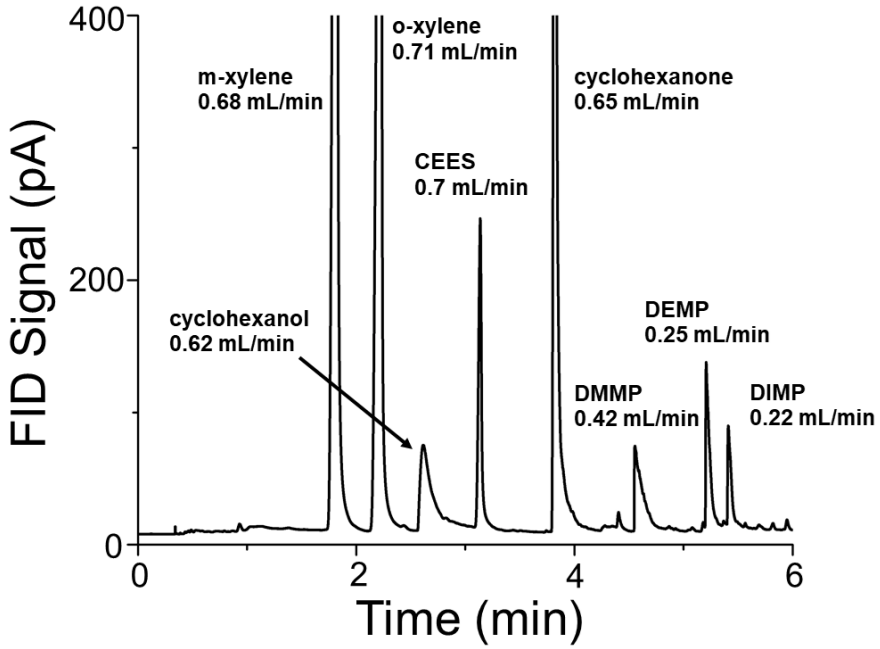

Figure 3.7 GC-FID chromatogram of 8-vapor mixture passively sampled with the μPP, transferred to the μPCF and injected. Separation used a 15 m RTX-200 column at 30 °C for 2.5 min, followed by 30 °C/min to 125 °C, then hold. The concentrations of the 8 vapors ranged from 2 mg/m^3 (cyclohexanol) to 12 mg/m^3(cyclohexanone) and injected masses from 37 to 250 ng. DE values were > 95% except for DEMP and DIMP (~80%).

3.5 Conclusions and Outlook

We conclude that the μPP we have presented here has numerous positive attributes that favor its use as part of the micro Collector-Injector (μCOIN) we are developing for μGC analysis of S/VOC mixtures. Prominent among these are its ability to sample S/VOCs at predictable rates with zero expended energy. This feature is particularly enabling for applications involving sampling for longer time periods where pumping would dominate the energy consumption for the μGC system as a whole. The modeled and experimental S_e values for the 15 compounds tested agree sufficiently well to verify the design strategy applied to the μPP and the model assumptions (exceptions noted and explained). Mixtures of up to eight compounds were sampled (and transferred) at rates matching those of the individual compounds, indicating no problems with

competitive displacement of one mixture component by another.

Advantages of the μPP over the predecessor passive micro-preconcentrator developed in our group include the radial topology, higher capacity, larger analyte range, lower desorption flow rate, longer sampling duration, and more robust fabrication process. A more comprehensive series of characterization tests was performed with the μPP as well.

Although the observed (diffusional) μPP sampling rates of ~0.16 to 0.78 mL/min are quite low, they are independent of concentration and are sufficiently high to collect ~ng quantities in sampling periods of 15-60 min for most compounds; adequate to serve the needs of numerous practical applications. The use of dual adsorbents enabled efficient sampling, thermal desorption, and transfer of most of the (predominantly polar) test compounds, which had vapor pressures ranging from 0.033 to 1.1 kPa, but some exceptional behavior was found. For example, NMP and DMSO suffered thermal decomposition upon desorption, but the latter could still be sampled reliably, albeit at a reduced rate. Off-gassing during extended post-exposure time periods was observed with o-xylene and DMMP due to weak adsorption on the C-B. The fractional loss was acceptably low for o-xylene, but was significant for DMMP. For the latter, this indicates that desorption/transfer cycle times would need to be constrained. More generally, it suggests that certain moderately volatile compounds may exhibit similar losses. Breakthrough of the polar and relatively volatile n-butanol and DMF occurred at high concentrations even over short exposure periods, highlighting the inherent shortcoming of using adsorbents with limited specific surface areas. This problem was anticipated, and design revisions intended to address it are discussed below.

o-Xylene and DEMP were selected to examine the effects of time and concentration on the

sampling rate of the μPP, which declined by < 10% at high concentrations (ie., 1,500 mg/m^3) over the short term for o-xylene (DEMP was not tested over such a wide concentration range) and by 20-30% over a 24-hr sampling period for both o-xylene and DEMP at low concentrations (i.e., 1-4 mg/m^3). We view these as decidedly positive results that indicate sampling rates should be stable enough to afford sufficiently accurate estimates of air concentrations by downstream μGC detectors for such exposure scenarios (exceptions cited above notwithstanding).

The semi-empirical model developed to describe the changes in the sampling rate with time and concentration accounts for the physicochemical processes governing the dynamics of vapor transport and uptake within the μPP. Implementation requires the Fickian *D* value, the vapor concentration, and the W_e value for one or both adsorbents at the exposure concentration. In addition, the reduced *D* value applicable to transport through the porous adsorbent bed(s) is needed. For the latter it may be possible to assume that it is a set fraction of the Fickian *D* value, but this has yet to be verified. Thus, additional measurements or data are needed to apply this model. Notably, although Fickian *D* values of many compounds in air can be found in the literature or calculated by the classical Fuller model, *D* values for organophosphonates are virtually absent from the literature we searched and cannot be calculated by known models.

Among the limitations of this study were the lack of TGA-derived W_e values for most of the compounds tested. Our use of breakthrough data from a parallel study to obtain rough or extrapolated estimates of W_e was cumbersome and approximate; far from ideal. Adsorption isotherms measured by TGA over a sufficiently wide concentration range for the compounds of interest with both C-X and C-B would provide more reliable W_e values and would be of great value in modeling. Furthermore, collecting sampling rates as a function of time and concentration for more compounds, together with such W_e values, would allow a more thorough assessment model

performance.

With respect to next-generation µPP designs, we plan to add a third adsorbent bed, packed with a higher-surface-area adsorbent, near the center of the device to enable the capture of more volatile and polar compounds. Several carbon molecular sieves are under consideration. Although this should impart some capacity for more volatile compounds, it would require that they diffuse further into the device to be trapped. This would lead to lower sampling rates, but the higher D values exhibited by smaller (i.e., more volatile) molecules would at least partially offset the longer pathlength. Capture of water vapor would also be of concern.

We are also considering µPP designs with higher sampling rates so that lower concentrations of target S/VOCs could be measured in similar sampling time periods. This demands a larger device with more apertures, more adsorbent mass, and potentially longer diffusion paths, such that decreases in sampling rates over time may be more significant. Alternative configurations are being considered to address this and other challenges accompanying such a change.

A companion publication is being prepared describing the µPHI that has been developed as part of the larger project concerned with the ultimate µCOIN. Integrating the µPP with the µPHI in a monolithic µCOIN device is also underway and will be followed by its inclusion and testing in one of several possible µGC prototype systems.

3.6 References

1. S. Zampolli, I. Elmi, F. Mancarella, P. Betti, E. Dalcanale, G. Cardinali and M. Severi, Real-time monitoring of sub-ppb concentrations of aromatic volatiles with a MEMS-enabled miniaturized gas-chromatograph, *Sens. Actuators, B*, 2009, **141**, 322-328.

2. S. K. Kim, H. Chang and E. T. Zellers, Microfabricated gas chromatograph for the selective determination of trichloroethylene vapor at sub-parts-per-billion concentrations in complex mixtures, *Anal. Chem.*, 2011, **83**, 7198-7206.

3. R. Manginell, J. Bauer, M. Moorman, L. Sanchez, J. Anderson, J. Whiting, D. Porter, D. Copic and K. Achyuthan, A monolithically-integrated μGC chemical sensor system, *Sensors*, 2011, **11**, 6517-6532.

4. W. R. Collin, G. Serrano, L. K. Wright, H. Chang, N. s. Nuñovero and E. T. Zellers, Microfabricated gas chromatograph for rapid, trace-level determinations of gas-phase explosive marker compounds, *Anal. Chem.*, 2013, **86**, 655-663.

5. A. Garg, M. Akbar, E. Vejerano, S. Narayanan, L. Nazhandali, L. C. Marr and M. Agah, Zebra GC: A mini gas chromatography system for trace-level determination of hazardous air pollutants, *Sens. Actuators, B*, 2015, **212**, 145-154.

6. M. Akbar, M. Restaino and M. Agah, Chip-scale gas chromatography: From injection through detection, *Microsyst. Nanoeng.*, 2015, **1**, 15039.

7. W. R. Collin, A. Bondy, D. Paul, K. Kurabayashi and E. T. Zellers, μGC× μGC: comprehensive two-dimensional gas chromatographic separations with microfabricated components, *Anal. Chem.*, 2015, **87**, 1630-1637.

8. Y. Qin and Y. B. Gianchandani, A fully electronic microfabricated gas chromatograph with complementary capacitive detectors for indoor pollutants, *Microsyst. Nanoeng.*, 2016, **2**, 15049.

9. M. Zhou, J. Lee, H. Zhu, R. Nidetz, K. Kurabayashi and X. Fan, A fully automated portable gas chromatography system for sensitive and rapid quantification of volatile organic compounds in water, *RSC Adv.*, 2016, **6**, 49416-49424.

10. J. Wang, J. Bryant-Genevier, N. Nuñovero, C. Zhang, B. Kraay, C. Zhan, K. Scholten, R. Nidetz, S. Buggaveeti and E. T. Zellers, Compact prototype microfabricated gas chromatographic analyzer for autonomous determinations of VOC mixtures at typical workplace concentrations, *Microsyst. Nanoeng.*, 2018, **4**, 17101.

11. J. Wang, N. Nuñovero, R. Nidetz, S. J. Peterson, B. M. Brookover, W. H. Steinecker and E. T. Zellers, Belt-Mounted Micro-Gas-Chromatograph Prototype for Determining Personal Exposures to Volatile-Organic-Compound Mixture Components, *Anal. Chem.*, 2019, **91**, 4747-4754.

12. J. J. Whiting, E. Myers, R. P. Manginell, M. W. Moorman, J. Anderson, C. S. Fix, C. Washburn, A. Staton, D. Porter and D. Graf, A high-speed, high-performance, microfabricated comprehensive two-dimensional gas chromatograph, *Lab Chip*, 2019, **19**, 1633-1643.

13. APIX ANALYTICS, https://www.apixanalytics.com/, (accessed October 2019).

14. zebra ANALYTIX, https://zebraanalytix.com/technology/, (accessed October 2019).

15. TCM Global, https://www.tcmglobalinc.com/, (accessed October 2019).

16. Omniscent, https://omniscent.com/, (accessed October 2019).

17. W.-C. Tian, H. K. Chan, C.-J. Lu, S. W. Pang and E. T. Zellers, Multiple-stage microfabricated preconcentrator-focuser for micro gas chromatography system, *J. Microelectromech. Syst.*, 2005, **14**, 498-507.

18. E. H. M. Camara, P. Breuil, D. Briand, N. F. de Rooij, C. Pijolat, A micro gas preconcentrator with improved performance for pollution monitoring and explosives detection, *Anal. Chim. Acta*, 2011, **688**, 175-182.

19. T. Sukaew and E. T. Zellers, Evaluating the dynamic retention capacities of microfabricated vapor preconcentrators as a function of flow rate, *Sens. Actuators, B*, 2013, **183**, 163-171.

20. J. Bryant-Genevier and E. T. Zellers, Toward a microfabricated preconcentrator-focuser for a wearable micro-scale gas chromatograph, *J. Chromatogr. A*, 2015, **1422**, 299-309.

21. R. P. Manginell, D. R. Adkins, M. W. Moorman, R. Hadizadeh, D. Copic, D. A. Porter, J. M. Anderson, V. M. Hietala, J. R. Bryan and D. R. Wheeler, Mass-sensitive microfabricated chemical preconcentrator, *J. Microelectromech. Syst.*, 2008, **17**, 1396-1407.

22. R. P. Manginell, S. Radhakrishnan, M. Shariati, A. L. Robinson, J. A. Ellison and R. J. Simonson, Two-dimensional modeling and simulation of mass transport in microfabricated preconcentrators, *IEEE Sens. J.*, 2007, **7**, 1032-1041.

23. J. H. Seo, S. K. Kim, E. T. Zellers and K. Kurabayashi, Microfabricated passive vapor preconcentrator/injector designed for microscale gas chromatography, *Lab Chip*, 2012, **12**, 717-724.

24. J. H. Seo, J. Liu, X. Fan and K. Kurabayashi, Fabry-Pérot cavity sensor-based optofluidic gas chromatography using a microfabricated passive preconcentrator/injector, *Lab Chip*, 2013, **13**, 851-859.

25. M. Akbar, N. Nuñovero, R. Hower, C. Zhan, J. Potkay and E. Zellers, A micro collector injector (μCOIN) for μGC systems, *2018 Solid-State Sensors, Actuators & Microsystems Workshop*, Hilton Head Island, USA, 2018.

26. C. Zhan, M. Akbar, R. Hower, J. Wang, N. Nuñovero, J. A. Potkay and E. T. Zellers, Integrated multi-vapor micro collector-injector (μCOIN) for μGC, *the 20th International Conference on Solid-State Sensors*, Actuators and Microsystems, Berlin, Germany, 2019.

27. FEDBIZOPPS.GOV, https://www.fbo.gov/index?s=opportunity&mode=form&id=798e9f3ca493a790d5e5bb6f0922c41a&tab=core&_cview=1, (accessed October 2019).

28. E. Palmes and A. F. Gunnison, Personal monitoring device for gaseous contaminants, *Am. Ind. Hyg. Assoc. J.*, 1973, **34**, 78-81.

29. E. V. Kring and W. J. Lautenberger, US Pat., 4,235,097, 1980.

30. J. L. Perkins, Modern Industrial Hygiene: Recognition and Evaluation of Chemical Agents, ACGIH, Cincinnati, 2008.

31. G. O. Wood and E. S. Moyer, A review and comparison of adsorption isotherm equations used to correlate and predict organic vapor cartridge capacities, *Am. Ind. Hyg. Assoc. J.*, 1991, **52**, 235-242.

32. F. Rouquerol, J. Rouquerol, K. S. W. Sing, P. Llewellyn and G. Maurin, *Adsorption by powders and porous solids: principles, methodology and applications*, Academic press, New York, 2013.

33. A. Wheeler and A. Robell, Performance of fixed-bed catalytic reactors with poison in the feed, *J. Catal.*, 1969, **13**, 299-305.

34. U.S. National Library of Medicine, https://toxnet.nlm.nih.gov/cgi-bin/sis/htmlgen?HSDB, (accessed October 2019).

35. M. Tang, M. Shiraiwa, U. Pöschl, R. Cox and M. Kalberer, Compilation and evaluation of gas phase diffusion coefficients of reactive trace gases in the atmosphere: Volume 2. Diffusivities of organic compounds, pressure-normalised mean free paths, and average Knudsen numbers for gas uptake calculations, *Atmos. Chem. Phys.*, 2015, **15**, 5585-5598.

36. J. T. Hunter and N. L. Abbott, Dynamics of the chemo-optical response of supported films of nematic liquid crystals, *Sens. Actuators, B*, 2013, **183**, 71-80.

37. D. A. Trubitsyn and A. V. Vorontsov, Experimental study of dimethyl methylphosphonate decomposition over anatase TiO2, *J. Phys. Chem. B*, 2005, **109**, 21884-21892.

38. VEGA ZZ Manual, https://nova.disfarm.unimi.it/manual/pages/gl_index.htm, (accessed October 2019).

39. G. Serrano, T. Sukaew and E. T. Zellers, Hybrid preconcentrator/focuser module for determinations of explosive marker compounds with a micro-scale gas chromatograph, *J. Chromatogr. A*, 2013, **1279**, 76-85.

40. C. J. Lu and E. T. Zellers, Multi-adsorbent preconcentration/focusing module for portable-GC/microsensor-array analysis of complex vapor mixtures, *Analyst*, 2002, **127**, 1061-1068.

41. A Tool for Selecting an Adsorbent for Thermal Desorption Applications, https://www.sigmaaldrich.com/content/dam/sigma-aldrich/docs/Supelco/General_Information/t402025.pdf, (accessed October 2019).

42. H. Zhu, R. Nidetz, M. Zhou, J. Lee, S. Buggaveeti, K. Kurabayashi and X. Fan, Flow-through microfluidic photoionization detectors for rapid and highly sensitive vapor detection, *Lab Chip*, 2015, **15**, 3021-3029.

43. C. C. Mulligan, N. Talaty and R. G. Cooks, Desorption electrospray ionization with a portable mass spectrometer: in situ analysis of ambient surfaces, *Chem. Commun.*, 2006, 1709-1711.

44. G. O. Nelson, *Gas mixtures: preparation and control*, Routledge, New York, 2018.

45. J. Wang, J. Ma and E. T. Zellers, Room-temperature-ionic-liquid coated graphitized carbons for selective preconcentration of polar vapors, *J. Chromatogr. A*, in press.

46. M. Bollyn, DMSO Can Be More than a Solvent: Thermal Analysis of Its Chemical Interactions with Certain Chemicals at Different Process Stages, *Organic Process Research & Development*, 2006, **10**, 1299-1312.

47. A. M. White and B. M. Sankey, US Pat., 4,168,226, 1979.

Chapter 4

Conclusions and Future Work

4.1 Summary

The dissertation describes design, assembly, characterization of two critical components of a microfabricated gas chromatographic analyzer for airborne volatile and semi-volatile organic compounds: the preconcentrator and the detector. The board goals were 1) to further develop a novel extant GC/μGC detector called a μOFRR sensor for the enhancement of the selective responses to different VOCs by probing the nanomaterial-coated μOFRR at different wavelengths with tunable lasers; 2) to develop a microfabricated passive preconcentrator for the refinement of a device previously developed in the Zellers/Kurabayashi groups called a μPPI and for integration with a companion micro-focuser and, ultimately, into a μGC that would be deployed in the field for autonomous operation for extended time periods on battery power.

4.2 A Nanomaterial-Coated Micro-Optofluidic Ring Resonator for Vapor Detection

This research concerned the further development of a recently invented nano-enabled, optical microsensor technology and its integration into a recently developed (in-house) belt-mounted prototype instrument to enhance the capability for near-real-time determinations of worker exposures to complex mixtures of VOCs. Bridging a gap between two other projects, this research was intended to yield proof-of-principle results to support more extensive development activities, with potentially significant impacts on the way we monitor worker exposures to VOC

mixtures. In one project, we have produced a prototype μGC analyzer with a 'single-transducer' array of CRs as the detector. The CR array uses different functionalized MPNs as vapor sensitive interface materials to produce a response pattern for each VOC. In another project, we have shown that, when probed optically rather than electrically, films of such MPNs can yield much higher levels of response diversity and vapor selectivity. In parallel, we had developed (invented) a new optical microsensor called a μOFRR that could serve as the ideal transducer for integrating the enhanced selectivity accruing from optically probing MPNs into the wearable μGC prototype.

In the research described here, we sought to demonstrate the following: 1) MPNs having different monolayer functionalities and/or core size can serve as highly effective, diversely responsive interface films on the μOFRR; 2) an MPN-coated μOFRR, when probed at three visible wavelengths simultaneously (via compact laser sources), can provide unprecedented VOC selectivity; and 3) MPN-coated μOFRRs can be used as replacements for the current CR-array μGC detectors and thereby enhance the analytical dimensionality of the microsystem and the complexity of VOC mixtures analyzable per sample. This work addressed several priorities and strategic goals defined by NIOSH. One key challenge was the reproducibility of optical responses of MPNs. Attempts to improve reproducibility by different substrate functionalization pre-treatments and casting solvent formulation changes were largely unsuccessful. However, the degree of diversity in the responses to a set of VOCs obtained by optical transmission screening experiments at three wavelengths was high and qualitatively similar to that observed in a previous study. We succeeded in fabricating a supply of μOFRR devices of good quality and demonstrated that detection of high concentrations of several VOCs was possible by use of different μOFRR interface films. Initial successful tests with a PDMS film were followed by successful tests using one type of MPN film and then a film comprising a functionalized Au nanorod (NR).

Implementation of the latter two devices as GC detectors was also demonstrated, though quantitative results were obtained only with the MPN film. A very low detection limit was achieved. Implementation of the MPN- and nanorod-coated μOFRR as the detector for our wearable μGC is planned for the near future. In summary, we have generated results demonstrating a) the diversity of optical VOC sensing with MPN films and b) the performance of MPN-μOFRRs as sensitive VOC sensors with compact laser sources. We have created guidelines for operating MPN-μOFRRs as μGC detectors and have characterized such devices for future testing.

The future work could further characterize the MPN-coated and NR-coated μOFRR sensors for VOC sensing with 1550- and 780-nm tunable laser systems. Through such studies we hope to demonstrate highly selective, single-sensor, multi-variable detection.

4.3 Microfabricated Passive Preconcentrator for μGC

This study describes the development and characterization of a μPP device. The μPP servers as the collector part of 2-stage μCOIN system with unprecedented low-power operation and flexibility, which will be integrated into a μGC system as a collector/injector module for autonomous measurements of S/VOC concentrations at least once per day for two years on battery power.

The development of μPP was motivated by addressing the shortcomings of a device previously developed in the Zellers/Kurabayashi groups called a μPPI by redesigning and re-purposing the μPPI device. The μPPI was composed of two layers. The top layer of μPPI had a grid consisting of 1530 parallel 54×54×200 μm apertures which constituted a part of vapor diffusion path as well as reduced the effects of turbulence. The bottom layer of μPPI included an etched cavity packed with 750 μg of Carbopack X and an integrated Ti/Pt resistor for thermal

desorption. The μPPI presented a passive sampling rate of ~9 mL/min for toluene and achieved ~2000 times of thermal desorption cycles witbhout performance degradation. However, μPPI had shortcomings. First, μPPI device had sample loss through the inlet grid during thermal desorption unless an extremely high flow rate (> 50 mL/min) was employed. The flow rate is sub-optimal for μGC columns and pumps. Additionally, the μPPI device had a limited adsorption capacity. The sampling rate for toluene was quite high (9 mL/min) but even at only 1 ppm the rate started to decline after 30 min, corresponding to ~1 μg of accumulated mass.

Advantages of μPP over the previous device design include the radial topology, higher capacity, larger analyte range, lower desorption flow rate, longer sampling duration, larger sampling concentration range, more robust fabrication process, and less vulnerability to competition among compounds. A more comprehensive series of characterization tests was also performed.

A μPP device (8×8 mm) also has two layers. The top layer has a grid structure comprising an array of 237 square apertures (47×47×180 μm). The bottom layer has two concentric annular cavities which were separated by Si pillars. Each cavity was loaded with one adsorbent. The integrated heaters on the bottom layer are used to thermally desorb the collected samples from μPP to the downstream micro focuser. The two layers were bonded by the Si-Au eutectic bonding technique. The tested compounds included the common solvents, chemical warfare agent simulants, and other compounds of interest to the Intelligence Community whose volatility ranged from 0.033 to 1.1 kPa.

Zero power consumption sampling was achieved. Effective (diffusional) μPP sampling rates ranging from ~0.16 to 0.78 mL/min were observed among the test compounds, which were in close agreement with theory for the device design or explicable by various reasons. The

sampling rates for two representative compounds, DEMP and o-xylene, declined by only ~23% and ~30% from 0.25 to 24 hr of continuous exposure at fixed, low concentrations. As for a short-term sampling period, the effective sampling rate of o-xylene was constant over a ~2,500-fold concentration range (0.6 to 1,500 mg/m^3) with a maximum uptake mass of ~14,000 ng. A semi-empirical model was developed to describe the changes in the sampling rate with time and concentration, which accounted for the physicochemical processes governing the dynamics of vapor transport and uptake within the µPP.

Desorption/transfer efficiencies were > 85% in all cases (most > 95%) at 250 °C (50 °C/sec) in 60 sec at 5 mL/min. The heating profile was highly reproducible and the device was heated hundreds of times without failure. Compared to 50 mL/min required to eliminate sample loss through grid during desorption for µPPI, µPP only required 5 mL/min by virtue of the radial topology and reduced sampling rate, which is more optimal for µGC columns and pumps.

Effective sampling and desorption of mixtures were achieved. There was no evidence that mixture sampling can affect the sampling rate of each compound in the mixture, which facilitated the quantitative mixture analyses. Some bleed (off-gassing) was observed for DMMP and o-xylene while that was not observed for DEMP.

One limitation of this study is the lack of TGA-derived W_e values. Additional tasks include running the m-xylene isotherm for C-B and performing more TGA experiments to extend the range of vapors. The W_e values would be of great value in modeling.

Additional work could also explore the performance of a µPP with three adsorbent cavities. The three-cavity design would further expand the range of vapors that can be effectively captured and desorbed.

Current μPP has the problem of declining sampling rate over time due to the gradual saturation of the adsorbents. The saturation of adsorbents can increase the effective length of diffusion occurring in the Segment 5, thereby decreasing the effective sampling rate. The problem could get diminished by re-designing the Segment 5 with a smaller effective length. Assuming the μPP with the new design is packed with the same mass of adsorbents, the reduced effective length of the Segment 5 will increase the mass of adsorbent loaded per unit length, which will slow down the saturation of adsorbents, thereby mitigating the decline of the effective sampling rate.

Future work can also try to replace the C-B with C-X. This might be able to eliminate the off-gassing problem for relatively volatile compounds, e.g. DMMP and o-xylene, although this might reduce the desorption efficiency of less volatile compounds, like DEMP.

Appendix

Supporting Information for Chapter 3

A1. µPP fabrication

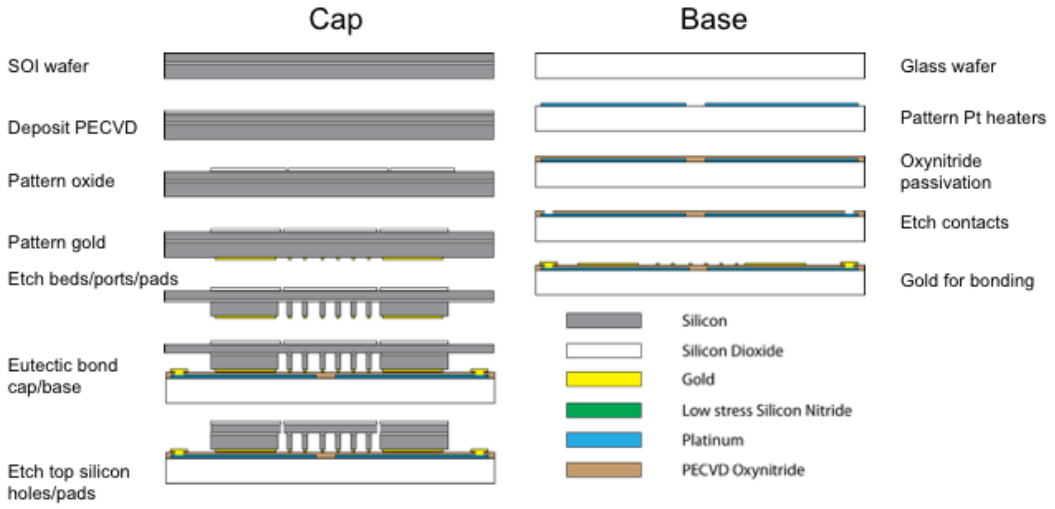

Figure A1. Summary of the fabrication process flow for the µPP device. Top SOI wafer layer thicknesses: device layer, 180µm; buried oxide layer, 1.5µm; handle layer, 380 µm. Bottom borofloat glass thickness was 200 µm.

The µPP fabrication process flow is summarized in Figure A1. The thicknesses of the three layers of the 4" silicon-on-insulator (SOI) wafer used to create the top substrate of the µPP are given in the caption of Figure A1. First, a 1-µm thick silicon dioxide layer was deposited onto the top of the device-layer side of the SOI wafer using plasma enhanced chemical vapor deposition (PECVD). Photoresist was then deposited and patterned (i.e., exposed) to define the circular array (i.e., ring) of sampling apertures at the periphery of the active device area (o.d. ≈ 4.3 mm). Each

aperture was defined as a 50 × 50 μm square spaced from laterally adjacent apertures by 75 μm. Two concentric rings of apertures (120 outer, 100 inner) were patterned, and then an additional 17 apertures were added, evenly distributed just outside the outer ring to bring the total to 237 apertures (see Figures 3.1f and g for micrographs of the apertures). In the same step, the rectangular regions at the corners of the chip, corresponding to where the wire-bonding areas are located on the bottom substrate, were patterned. All exposed regions of PECVD oxide were then removed by reactive ion etching (RIE).

Next, a seed layer of Au was deposited onto the back (i.e., handle layer) side of the SOI wafer, patterned with photoresist and electroplated to a thickness of ~2 μm using a standard plating bath in the exposed areas. The Au seed layer was then stripped. Next, photoresist was patterned to define the adsorbent-bed cavities, retention pillars, wire-bonding regions, fill ports, and fluidic channel (please refer to Figure 3.1e and f) and these features were formed by deep-reactive-ion etching (DRIE) down to the buried oxide layer. Finally, the exposed buried oxide was etched away with buffered HF to ensure that when the aperture grid was later etched from the top side that the apertures extend through the top substrate.

Figure A2 shows the top substrate of the chip after DRIE. The pillars are ~180 μm in diameter and spaced by ~130 μm. The three fill ports and the fluidic channel are 460 and 170 μm wide, respectively, at their narrowest points. The height of all features is 380 μm.

The first step in processing the bottom (glass) wafer entailed depositing photoresist, patterning (exposing) the locations for the heaters, RTDs, and electrical traces out to the wire-bonding areas on the top surface. Ti and Pt at thicknesses of 100Å and 1000Å, respectively, were deposited and a standard lift-off procedure was used to remove the unwanted metal. A 2-μm thick SiON (oxynitride) layer was then deposited by PECVD to serve as an electrical isolation layer.

Next, the contact holes were patterned using photoresist and the oxynitride was etched away with buffered HF to expose the Pt metal for eventual wire bonding. Finally, a thin Au film was deposited and patterned by lift-off at the locations matching those of the top substrate needed for eutectic bonding (see Figure A3 for a micrograph of a portion of the bottom substrate prior to bonding).

The top and bottom substrates were then aligned using a contact aligner and bonded using Au-Si eutectic bonding.[A1] The apertures and wire-bonding regions previously patterned in the oxide on the top surface of the top substrate were then etched by DRIE using the remaining oxide as the etch mask. Finally, the wafers were diced using a dicing saw, and thoroughly cleaned using organic solvents, yielding devices such as that shown in Figure 3.1f.

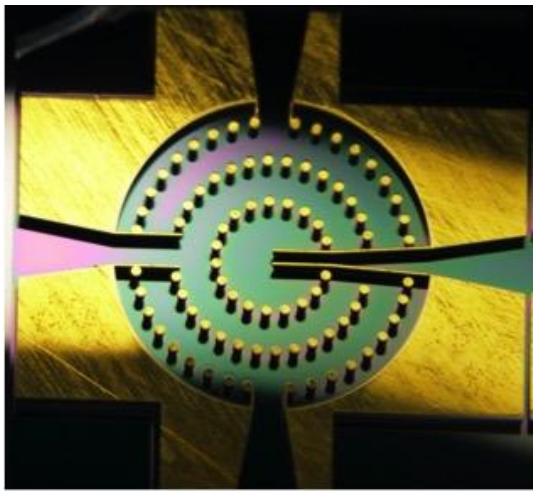

Figure A3. Top substrate prior to wafer bonding, showing adsorbent cavities, adsorbent retention pillars, fill ports (3), and fluidic channel (right side). Au layer is where eutectic bonding to the bottom substrate will occur.

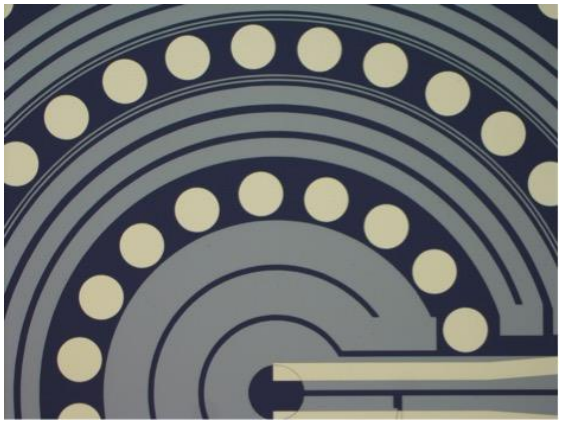

Figure A2. Borofloat glass bottom substrate with heaters shown in gray and Au layer at the bases of the pillars and fluidic port where eutectic bonds will occur in white.

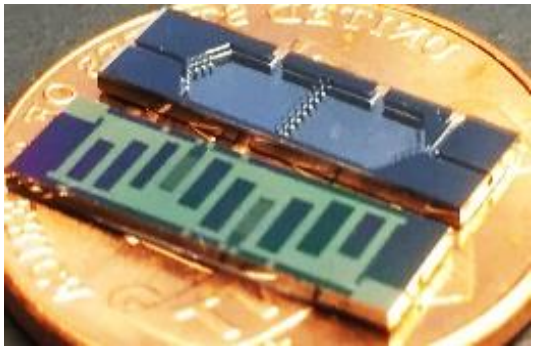

Figure A4. Photo of µPCF. Lower image is the backside heater and upper image shows the two adsorbent cavities, fill ports, and fluidic channels of the unfilled device. See ref. A2 for more details.

A2. Test system and exposure chamber

The test atmosphere generation system and associated components are shown schematically in Figure A5. The custom-made stainless-steel exposure chamber (12.7 × 7.6 × 3.9 cm; ~42 mL internal volume) used to house the µPP for performance tests is shown in Figure A6 with the cover plate (top layer) removed. The bottom plate has tapped inlet and outlet holes for gas flow, flanking a central 1”-diameter clearance hole for electrical interconnections between the PCB-mounted µPP and a routing PCB bolted to the underside of the bottom plate and sealed with a Teflon o-ring. The 11 contact pins on the routing PCB passing vertically through the central hole of the chamber floor plate serve as mechanical supports for the µPP carrier PCB “pedestal” and as the electrical interconnects.

The middle plate of the chamber was machined to create a chamfered diamond shaped cavity that defines the internal volume. A tapped hole in the side of the middle plate of the chamber accepts a PEEK fitting with a reverse ferrule that seals the (Microlumen-wrapped) µPP outlet capillary to the chamber wall. The outlet capillary extends through this fitting to one of the 6-port valve ports for directing the flow from the µPP to the µPCF during desorption and sample transfer.

Teflon gaskets are used to seal the top and bottom plates to the middle plate with compression provided by a set of nuts and bolts.

At a flow rate of 1 L/min, the atmospheric concentration in the chamber can reach 95% of the equilibrium concentration within ~2 min for m-xylene, as indicated by GC-FID measurements. The theoretical 95% mixing time is about 10 sec. The longer time required in practice maybe due to adsorption by the upstream 3-way solenoid valve. Consistent with this explanation, for less volatile test compounds, such as DEMP, the time to steady-state concentration was longer (i.e., ~4 min). After exposure, the testing chamber was purged with N_2 for 4 min at 1 L/min, which was sufficient to remove any trace of residual vapor.

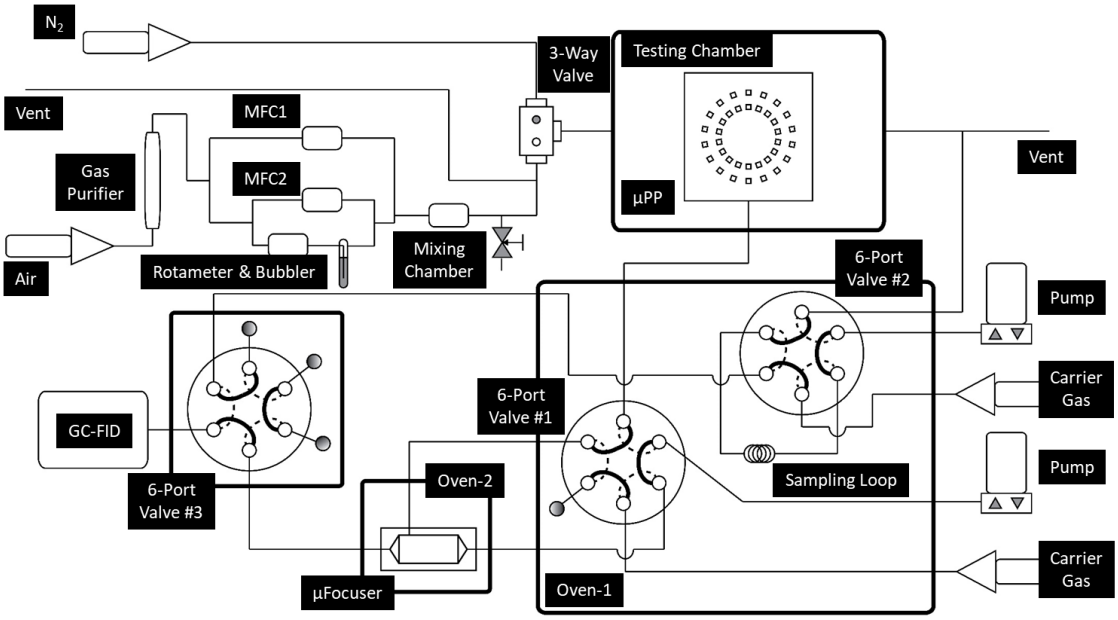

Figure A5. Diagram of the µPP test system. The three six-port valves can be switched to achieve the following three functions: 1) monitoring the concentration and composition of the test-chamber atmosphere; 2) transferring collected samples from the µPP to µPCF; 3) analyzing samples injected from µPCF by GC-FID.

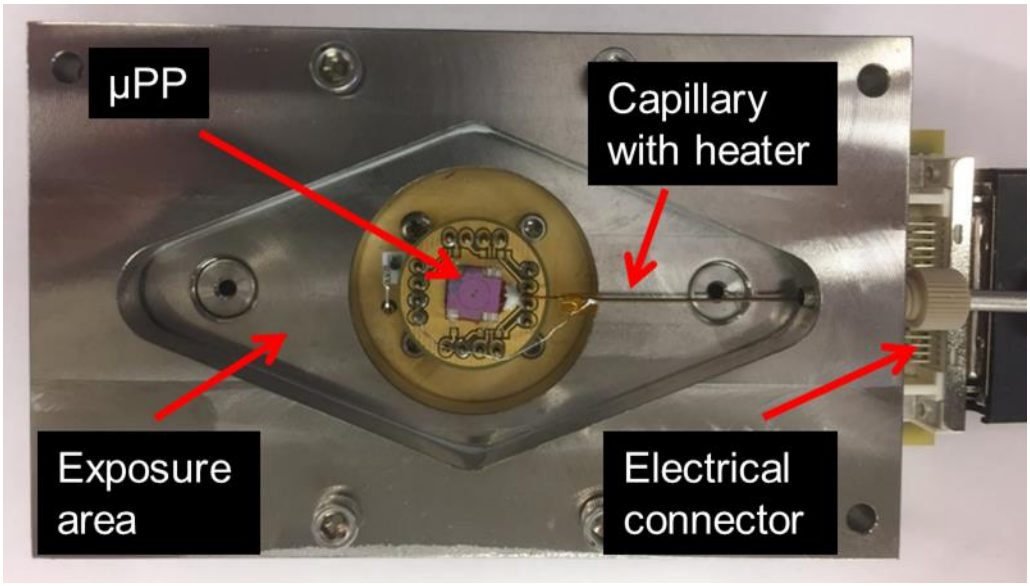

Figure A6. Photo of the exposure chamber with µPP mounted inside it.

A3. TGA set-up and procedure

The TGA was used to measure the equilibrium adsorption capacity, W_e, of selected vapors as a function of concentration for each adsorbent material. The test atmosphere generation system described above was adapted for these experiments by directing the flow through tubing connected to the sample chamber within the TGA to allow real-time mass measurements during exposure, N_2 purge, and then heating to desorb the vapors. For most tests, ~2.6-2.9 mg of the sieved adsorbent material (i.e., C-X or C-B) was loaded into the standard weighing pan of the TGA and suspended from the arm of the gravimetric mechanism. It was then heated to 250 °C under a flow of N_2 to precondition the sample for > 30 min.

The flow of test atmosphere was divided so that a portion would flood the chamber containing the sample and a portion was sent to a sampling loop connected to a 6-port valve mounted on the GC. Samples were periodically injected into the GC over the course of each exposure to confirm the magnitude and stability of the exposure concentration. Since testing

involved only individual compounds no column was used. Rather, a short segment of deactivated fused silica capillary (guard column) was used to connect the injection port to the FID.

For isotherm determinations, each concentration was tested individually and the mass uptake was monitored until a plateau was reached followed by thermal desorption to confirm recovery of the baseline. Then the next concentration was tested. Equilibration times were on the order a few hrs. For other tests, exposures were allowed to proceed for a certain time period, then an N_2 purge was used to remove the vapor so that any off-gassing could be detected, and then the sample was heated to confirm recovery of the baseline.

A4. Temperature profiles

A typical time-temperature profile for each of the three RTDs on the μPP is shown in Figure A7. Closed-loop control of the two cavity heaters allows precise control and coordination of the temperatures in both adsorbent beds. Modest heating rates were used so that it took about 6 sec to achieve the maximum temperature with no overshoot.

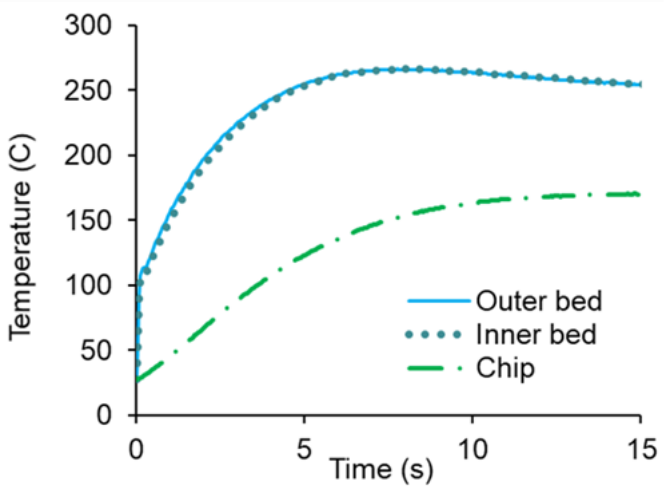

Figure A7. Profiles from the RTD readings for one heating sequence of the inner and outer adsorbent cavities, as well as the chip area (outside of the cavities) of the μPP device.

A5. TGA data and W_e values

Most studies of VOC adsorption on carbon adsorbents employ models based on the classical Langmuir adsorption isotherm: [A3-A8]

$$W_e = W_{e-max}\ \frac{b \times C}{1 + b \times C} \qquad \text{Eq. A.1}$$

where $W_{e\text{-}max}$ is the maximum monolayer coverage capacity (µg/g), b is the Langmuir isotherm constant (L/mg), and C is the VOC concentration (mg/m^3).

Figure A8 shows the adsorption isotherm for m-xylene on C-X over a concentration range of 0.9 to 1300 mg/m^3. The W_e value increased with the increasing m-xylene concentration at a steadily decreasing rate and the isotherm was fit to the following Langmuir model, represented by the curve in Figure A8 (r^2 = 0.936):

$$W_e\ (\mu g/g) = \frac{61000\ (\mu g/g) \times 25\ (L/mg) \times C\ (mg/m^3)}{1 + 25\ (L/mg) \times C\ (mg/m^3)} \qquad \text{Eq. A.2}$$

Figure A9 shows that W_e is inversely proportional to the vapor pressure among four vapors of similar polarity with C-X: toluene, m-xylene, 1,2,4-TMB and n-decane at similar concentrations (4-6 mg/m^3).

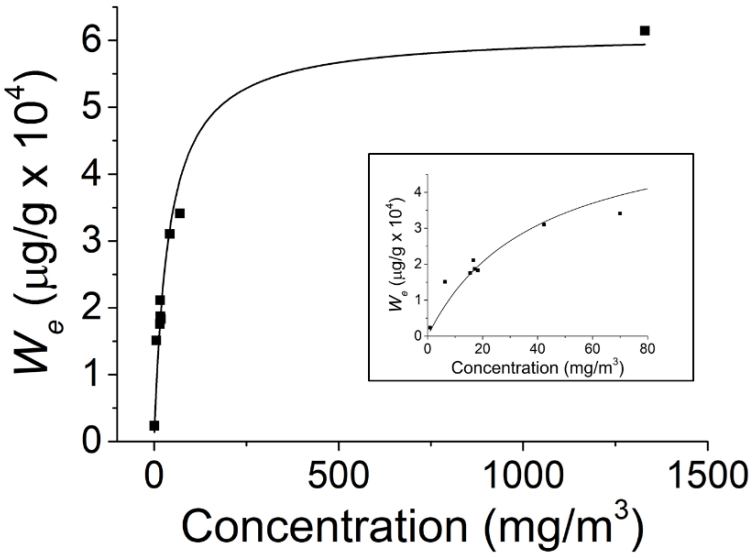

Figure A8. W_e values of C-X for exposure to different concentrations of m-xylene. The curve is the fitted to the Langmuir model in Eq. A.2 (R^2 = 0.96).

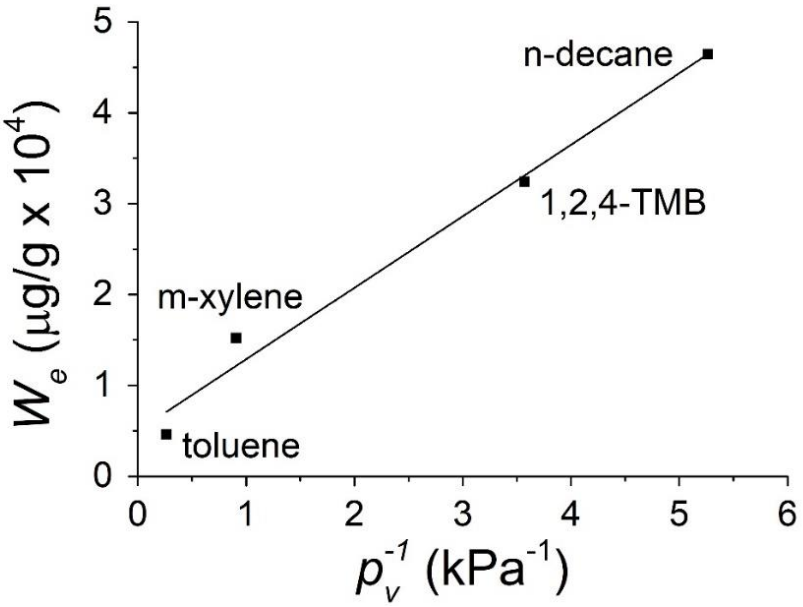

Figure A9. W_e values of several VOCs with C-X as a function of 1/(vapor pressure). Vapor pressures of toluene, m-xylene, 1,2,4-TMB, and n-decane are 3.8, 1.1, 0.28, and 0.19 kPa, respectively (R^2 = 0.98).

Table A1. Values of $M_{b\text{-}10}$ for several compounds obtained in published breakthrough tests with C-B and C-X, and the corresponding W_e values at 3.5 mg/m^3 derived therefrom. Also included are the estimates of maximum uptake masses on the C-B bed of the μPP at 3.5 mg/m^3 for the same compounds.

Compound	$M_{b\text{-}10}$[a] (μg)		W_e[b] (μg/g)		C-B Max. Uptake Mass (ng)
	C-B	C-X	C-B	C-X	
m-xylene	12		1700	4900	1000
o-xylene			2100	6100	1300
DMMP	3.9	11	550	1600	340
DEMP	11		1600	4500	950
DIMP	16		2300	6500	1400
NBZ	24		3400	9800	2100
n-butanol		1.3	—[c]	190	—[c]

[a] *$M_{b\text{-}10}$ values are the 10% breakthrough masses reported in ref. A9;* [b] *W_e value estimation processes are discussed in the text;* [c] *experimental testing reported in ref. A9 showed n-butanol to be unretained on C-B.*

TGA testing of the lower volatility compounds DMMP, DEMP, DIMP, and NBZ was not possible due to their adsorption on surfaces and persistence. Therefore, we used alternative methods to estimate W_e values.

In a separate study of vapor adsorption capacity, we conducted conventional breakthrough tests with packed tubes containing either C-B or C-X exposed continuously to each of several individual test compounds at a single vapor concentration.[A9] Most compounds were only tested with C-B. Measured 10% breakthrough volumes ($V_{b\text{-}10}$) were converted to the corresponding 10% breakthrough masses ($M_{b\text{-}10}$) to account for the different challenge concentrations used. Theoretically, $M_{b\text{-}10}$ which for a given compound should be proportional to W_e according to the Wheeler Model.[A9] Using m-xylene as the reference compound, the following values of relative $M_{b\text{-}10}$ values were found for breakthrough tests with C-B: 1.0, 0.33, 0.92, 1.3, and 2.0 for m-xylene, DMMP, DEMP, DIMP, and NBZ, respectively. For one of these compounds, DMMP, we also ran breakthrough tests with C-X, and the C-X:C-B ratio of $M_{b\text{-}10}$ values for DMMP was 2.9 at the same concentration. Assuming that this ratio would be applicable to other vapors, we applied it to the W_e value of m-xylene on C-X at 3.5 mg/m^3 determined by TGA to obtain an estimate of W_e on C-B for m-xylene. This specific concentration was arbitrary. Combining this estimate of We

with the ratios listed above, it was possible to estimate W_e on C-B for the other vapors at the same concentration. Breakthrough tests of n-butanol with C-B showed no retention (i.e., immediate breakthrough), whereas with C-X the n-butanol breakthrough volume (mass) was short but measurable, thereby permitting an estimate of W_e.[A9]

Based on the estimated W_e values and the measured adsorbent masses, we could also estimate the equilibrium uptake mass for each compound on C-B (the adsorbent in the outer bed of µPP). These estimates of W_e and uptake mass are presented in Table A1 and were used in the modeling discussed further below.

The W_e value of o-xylene on C-X was estimated from that of m-xylene at a similar concentration via the plot in Figure A9 by assuming that its W_e value is proportional to the inverse of vapor pressure, which should be valid for compounds with similar polarities (or, in this case, for an isomer). The W_e value of o-xylene on C-B was then estimated, as described above, using the ratio of W_e values on C-X and CB found for DMMP (i.e., 2.9, see above).

A6. Desorption (transfer) profiles and efficiencies

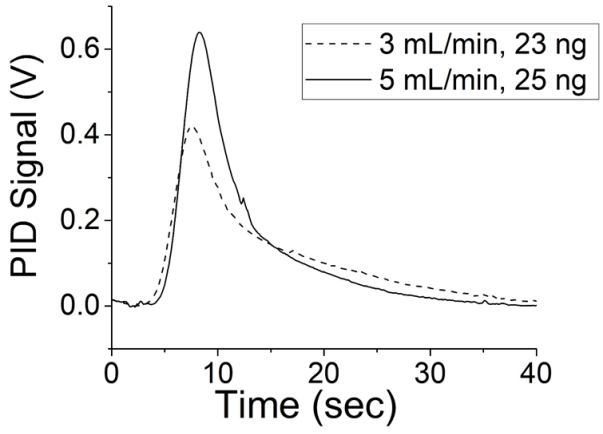

Figure A10. Desorption profiles of o-xylene from the µPP under the two indicated flow rates at 250 °C as measured with an in-line photoionization detector (mini-PID). The indicated masses collected from the test atmosphere were determined. Challenge concentrations were ~ 12 mg/m^3.

To characterize the transfer of o-xylene from the μPP during desorption, we connected a mini-PID between the mini-pump and the outlet of the μPP. Two tests were performed at a similar exposure concentrations and exposure times, but at different desorption flow rates (i.e., 3 mL/min and 5 mL/min). Two consecutive desorption cycles were performed in each case and no desorption peak was observed for the second desorption cycle, confirming that desorption was efficient. The collected masses were similar between two tests as expected. As shown in Figure A10, the profile showed significant tailing but the responses returned to baseline within about 30 sec. The full width at half maximum (FWHM) was 5.7 and 4.7 sec at 3 and 5 mL/min, respectively.

Table A2. The sampling rates and desorption efficiencies (DE) of μPP at 250 °C for DMMP with different transfer conditions (transfer flow rate and transfer time).[a]

S_e (mL/min)	Transfer flow rate (mL/min)	Transfer time (sec)	DE (%)
0.44	10	240	100
0.44	10	120	98
0.43	10	60	97
0.44	5	60	99

[a] *Exposures ranged from 24-30 mg/m^3 for 15 min resulting in mass uptakes of 160-200 ng*

Tables A2 and A3 show the results of desorption tests with DMMP and DEMP, respectively. The *DE* values for DMMP were > 97% under all conditions. For DEMP, the *DE* at 250 °C was 85% (data not shown). Increasing T_{max} to 275 °C improved the *DE* to 94%.At this T_{max}, reducing the transfer time from 60 to 30 sec, resulted in a decrease in *DE* to 78%. Thus, 60 sec at 275 °C at 5 mL/min seemed to be the best condition for transfer.

Table A3. The sampling rates and desorption efficiencies of μPP at a transfer flow rate of 5 mL/min and transfer temperature of 275 °C for DEMP with different transfer time.

S_e (mL/min)	Transfer time (sec)	DE (%)
0.26	60	94
0.26	50	89
0.25	40	79
0.25	30	78

[a] *Exposures ranged from 54-63 mg/m^3 for 15 min for a total mass load of 210-230 ng.*

Table A4. Results of μPP off-gassing tests for o-xylene, DMMP, and DEMP with 4 min and 60 min purge times after exposure.

Compound	Purge time (min)	Conc. (mg/m^3)	Uptake mass (ng)	S_e (mL/min)	S_e change (%)
o-xylene	4	52	530	0.67	-6.0
	60	59	560	0.63	
DMMP	4	49	320	0.43	-19
	60	47	245	0.35	
DEMP	4	57	210	0.25	0
	60	52	190	0.25	

A7. Modeling changes in S_e values as a function of time and concentration

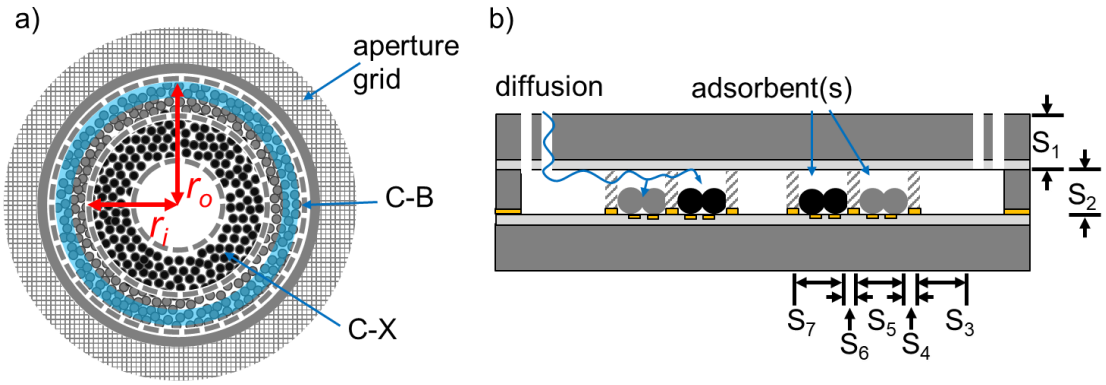

Figure A11. a) Top view of μPP showing radii and adsorbent beds (the blue annulus corresponds to a hypothetical saturated C-B area at a certain time point); b) Enlarged version of Fig. 3.1b showing a side view of formalized segments of the diffusion path and individual sampling rates (S_1-S_7).

As stated in Chapter 3, to model the effective sampling rate for a given vapor, we formally divided the diffusion path into 7 segments as shown in Figure A11. Each segment is defined as follows:

- Segment 1 corresponds to the aperture grid through which vapors diffuse vertically and for which L_1 is the thickness of the top substrate and A_1 is the product of the aperture cross section (47 × 47 μm) and the number of apertures (n = 237).
- Segment 2 corresponds to the space beneath the apertures through which vapors will also diffuse vertically to the floor of the bottom substrate, for which L_2 is the height of the channel (380 μm) and A_2 is defined to include the total area of the aperture grid and the spaces between the apertures. Thus, Segment 2 corresponds roughly to the volume of the annular ring beneath the grid of apertures.
- Segment 3 corresponds to the open space adjacent to (just inside of) Segment 2 through which vapors diffuse laterally (inwardly) toward the first ring of retention pillars. For this segment we assume that L_3 is the distance from the edge of Segment 2 to the pillars, and A_3 is the average cross section of the lateral path but at only at the height of adsorbent granules (237 μm). The formal assumption here is that the headspace has no vapor.
- Segment 4 is the path through the pillars for which L_4 is the diameter of a pillar and A_4 is the sum of the inter-pillar distances multiplied by the height of the adsorbent granules.
- Segment 5 is the outer (C-B) adsorbent bed through which vapors diffuse laterally. In this case diffusion will be some combination of free (i.e., Fickian) diffusion through the interstitial spaces between the particles and pore (i.e., Knudsen) diffusion within the adsorbent particles. Therefore, the D value in this segment is assumed to be lower than that in the preceding segments. L_5 is the radial length of entire C-B adsorbent bed, which is

only reached by vapor after saturation of the entire adsorbent bed. A_5 decreases physically from the outer to inner boundaries of the adsorbent bed. As with the radial length, the effective value of A_5 over the course of a sampling period will depend on the extent of bed saturation. S_5 will decrease over time and, therefore S_e will also decrease over time.

- Segment 6 corresponds to the next set of pillars and its dimensions are defined similarly to that of Segment 4, accounting for the lower number of pillars at this point in the device structure.
- Segment 7 is the inner (C-X) adsorbent bed. As in Segment 5, diffusion will be some combination of free (i.e., Fickian) diffusion through the interstitial spaces between the particles and pore (i.e., Knudsen) diffusion within the adsorbent particles. Therefore, the D value in this segment is also assumed to be lower than that in segments not containing adsorbent. L_7 is the radial length of entire C-X adsorbent bed, which is only reached by vapor after saturation of the entire adsorbent bed. A_7 decreases from the outer to inner boundaries of the adsorbent bed. As with the radial length, the effective value of A_7 over the course of a sampling period will depend on the extent of bed saturation. Since S_7 will decrease over time, it will contribute to a decrease in S_e for vapors penetrating this bed.

As discussed in Chapter 3, the response time can be estimated by first dividing the volume of each segment *S1-S4* its modeled S_i value (i = 1, 2, 3, 4), and then summing the resulting segmental response time values. See Table A5 for the relevant values for o-xylene.

Table A5. Segmental effective sampling rates (S_i) and volumes relevant to the calculation of the response time (i.e., time to steady state) of the μPP for o-xylene.[a]

Segment	S_i (mL/min)	Volume (mm^3)	Response Time (msec)
1	1.3	0.094	4.5
2	2.6	0.86	20
3	13	0.18	0.84
4	3.6	0.27	4.5
		Total	30

[a] *similar calculations for DEMP and DIMP gave values of 60 msec and 77 msec, respectively.*

Next we model the instantaneous sampling rates (S_5 and S_e) as a function of time, and then calculate the net time-averaged S_e values over a specified sampling period. We focus on the effect on S_e of the gradual saturation of the adsorbent in segment 5 (S5) that occurs either over time at a given concentration of vapor or over a range of vapor concentrations at a fixed sample duration. Analogous expressions are used to model S_7. Considering S_5 in isolation, we have the formal expression: $S_5 = D_5A_5/L_5$. However, since the effective values of A_5 and L_5 will vary with time and the degree of saturation, we have designated them as l_s and a_s. It is assumed that D_5 is constant.

To develop the model, we considered the case where the μPP collects a series of samples over several discrete time periods and transfers the collected mass downstream for analysis (as in Figure 3.4 for o-xylene). For each time, t, an injected mass of vapor is measured, $m_{v(t)}$. Assuming that the penetration into the bed proceeds only after saturation is achieved in the adjacent upstream fraction of the bed at a given air concentration, we can estimate the saturated adsorbent mass ($m_{s(t)}$) corresponding to each value of $m_{v(t)}$ by the following:

$$m_{s(t)} = \frac{m_{v(t)}}{W_e} \qquad \text{Eq. A.3}$$

where W_e is the equilibrium adsorption capacity at a given concentration C_0 (see Section S5).

We can also estimate the maximum vapor mass required to saturate the bed, $m_{v\text{-}max}$, at a given C_0 by the product of W_e and the total bed mass, $M_{a\text{-}max}$. We can then determine what fraction of the adsorbent bed, $f_{s(t)}$, is saturated after each time period as

$$f_{s(t)} = \frac{m_{s(t)}}{M_{a-max}} \qquad \text{Eq. A.4}$$

The total bed area, which we call $\Lambda_{a\text{-}max}$ (to differentiate it from the cross sectional area of the diffusion path, A), is obtained from the CAD design layout for the device. Multiplying $f_{s(t)}$ by $\Lambda_{a\text{-}max}$ gives the area of the bed, $\alpha_{s(t)}$, saturated at time t. Assuming $\alpha_{s(t)}$ is evenly distributed around the perimeter of the bed, P, it would consist of an annulus of adsorbent of radial length $l_{s(t)}$. At the point where the adsorbent bed is fully saturated, $l_{s(t)}$ would equal L_5. Since $\Lambda_{a\text{-}max}$ is the sum of the areas of the saturated and unexposed bed, we have:

$$\Lambda_{a-max} = \alpha_{s(t)} + \pi(r_o - l_{s(t)})^2 - \pi {r_i}^2 \qquad \text{Eq. A.5}$$

where r_o and r_i are outer and inner radii of the (outer, C-B) adsorbent bed, respectively. Rearranging this equation, we have the following, which can be used to obtain the value of $l_{s(t)}$ for each $\alpha_{s(t)}$ corresponding to exposure for any discrete time period:

$$l_{s(t)} = r_o - \sqrt{\frac{\Lambda_{a-max} - \alpha_{s(t)} + \pi {r_i}^2}{\pi}} \qquad \text{Eq. A.6}$$

Of course, l_s and α_s change continuously with time, and can be expressed as continuous variables. Within an incremental time interval dt there will be incremental increases in adsorbed vapor mass (dm_v), saturated adsorbent area ($d\alpha_s$), and saturated radial length (dl_s). Furthermore, the following equality should hold:

$$\frac{dm_v}{m_{v-max}} = \frac{d\alpha_s}{\Lambda_{a-max}} \qquad \text{Eq. A.7}$$

and $d\alpha_s$ can be expressed as the product of the perimeter of the unexposed bed (P_u) and dl_s as follows:

$$d\alpha_s = P_u dl_s = \pi(2r_o - 2l_s)dl_s \qquad \text{Eq. A.8}$$

Assuming S_e is constant within this interval, then dm_v can be expressed as follows:

$$dm_v = S_e C_0 dt \qquad \text{Eq. A.9}$$

Limiting this analysis to the first five segments, eq. 3.1 can be expressed as follows:

$$S_e = \frac{1}{\frac{1}{S_1}+\frac{1}{S_2}+\frac{1}{S_3}+\frac{1}{S_4}+\frac{1}{S_5}} = \frac{1}{\frac{L_1}{DA_1}+\frac{L_2}{DA_2}+\frac{L_3}{DA_3}+\frac{L_4}{DA_4}+\frac{l_s}{D_5 a_s}} \qquad \text{Eq. A.10}$$

where D is the Fickian diffusion coefficient (listed in Table 3.1), and D_5 is the diffusion coefficient in S5, which is assumed to be smaller than D by virtue of the contribution of (slower) pore diffusion (see above), and a_s is the cross-sectional area at the inner edge of the saturated region of the bed. The latter is the product of P_u and the height of adsorbent bed (h):

$$a_s = P_u h = \pi(2r_o - 2l_s)h \qquad \text{Eq. A.11}$$

Since S_1-S_4 are constant at steady state, Eq. A.10 can be simplified to:

$$S_e = \frac{1}{\sigma_{1-4}+\frac{l_s}{D_5 h\pi(2r_O-2l_S)}} \qquad \text{Eq. A.12}$$

where $\sigma_{1\text{-}4} = 1/S_1+1/S_2+1/S_3+1/S_4$.

Substituting the expression for S_e in Eq. A.10 into Eq. A.9, and then substituting the expressions for $d\alpha$ and dm_a in Eqs. A.8 and A.9 into Eq. A.7 and rearranging gives:

$$\frac{\Lambda_{a-max}\, C_0}{m_{v-max}\, \pi} dt = \left[(2r_o - 2l_s)\sigma_{1-4} + \frac{l_s}{D_5 h\pi}\right] dl_s \qquad \text{Eq. A.13}$$

Eq. A.13 has only two variables, t and l_s. All the other parameters in the equation are constant (note: D_5 is also a constant, but its value is unknown). Thus, the left-hand side is integrable with respect to t, and the right-hand side is integrable with respect to l_s.

Imposing the boundary condition that $l_s = 0$ when $t = 0$ and integrating both sides of eq. A.13 gives an equation relating l_s to t wherein all the determinant variables are known except for D_5:

$$\frac{\Lambda_{a-max}\, C_0}{m_{v-max}\, \pi} t = 2r_o\sigma_{1-4}l_s + \frac{l_s^2}{2}\left(\frac{1}{D_5 h\pi} - 2\sigma_{1-4}\right) \qquad \text{Eq. A.14}$$

The required value of D_5 must be determined empirically for each vapor. For o-xylene, for example, experimental values of $l_{s(t)}$ were calculated via Eq. A.6 for each of the six cases shown in Figure 3.4 for which $m_{v(t)}$ values were measured at each t. The corresponding modeled values of l_s are expressed in Eq. A.14 as a function of D_5 for each case at the same (known) value of t. Thus, each discrete modeled value $l_{s(t)}$ now depends only on D_5. By iteratively solving Eq. A.14 using D_5 values ranging incrementally from 0 (lower bound) to the Fickian D value (upper bound, i.e., 0.072 cm^2/sec for o-xylene), the optimal value was determined as that providing smallest relative error between modeled l_s values at time t and experimental $l_{s(t)}$ values.

For o-xylene, the resultant value of D_5 was 0.025 cm^2/sec and for DEMP the D_5 value obtained by the same approach was 0.015 cm^2/sec. With these optimized D_5 values and Eq. A.14, we can model l_s for any t assuming the vapor is retained in the C-B bed. By substituting the modeled l_s value into Eq. A.12, we can then obtain the modeled instantaneous S_e value for any t, again, assuming the vapor is retained in the C-B bed.

For comparison with experimental S_e values, we need to determine the time-averaged S_e value over a certain time period. A sufficiently accurate estimate can be obtained by calculating S_e

at each 1-minute interval via eq. A.12, summing, and dividing by the total time. The modeled results for DEMP and o-xylene are presented alongside the experimental S_e values in Figures 3.4 and 3.5, respectively.

An analogous approach would be used to estimate D_7 in the C-X bed for any vapors that penetrate beyond the C-B bed during sampling. In fact, for o-xylene, the model predicts penetration into the C-X bed after ~14 hr at the modeled concentration of 3.5 mg/m^3. Since we did not have the data required to estimate D_7 in the same manner as we estimated D_5, it was assumed that D_7 was equivalent to D_5. For the purpose of modeling the 24-hr Se value presented in Figure 3.5. Given the higher specific surface area and packing density, as well as the different pore-size distribution of C-X (vs. C-B), it is likely that D_7 would be somewhat lower than D_5. Accordingly, the model underestimates S_e for the 24-hr sample of o-xylene.

Thus far, we have only dealt with modeling how the sampling rate changes with time. Using the same approach, it is possible to model the S_e as a function of concentration for a fixed time period. The same optimized D_5 value can be used. For any specified concentration, C_0, we need to calculate the corresponding W_e value from TGA measurements or by the approach described above from breakthrough testing. This, then, will give a new $m_{v\text{-}max}$ value. With C_0 and $m_{v\text{-}max}$ values, we can use eq. A.14 to model l_s at any t, followed by calculation of the instantaneous and time-averaged S_e values via eq. A.12. The results for o-xylene are shown in Fig. 3.3.

Unfortunately, modeling S_e for an untested compound would not be possible because of the need for an optimized D_5 value, which must be derived empirically as we did above. As we discuss in the next section, for o-xylene and DEMP, the ratio of the Fickian D value to the D_5 value was 2.9 and 2.4 respectively (i.e., 0.072/0.025 and 0.036/0.015, respectively). Assuming that the average ratio for these two compounds (i.e., 2.7) could be applied to any other compound, we

could then estimate D_5 for untested vapors for which we have Fickian D values. For the few cases in Table 3.1 for which we had W_e values, we used this approach to model their 0.25-hr S_e values. However, due to the short time period the change in S_e as a function of time was too small to allow an assessment of the reliability of this approach to estimating D_5.

A8. Calculations of Fickian diffusion coefficients (D)

Fickian *D* values were obtained from the literature for six of the compounds listed in Table 1 (i.e., m-xylene, o-xylene, NBZ, DMMP, n-butanol, and DMF).[A10-A12] Since published values could not be found for the remaining nine compounds, they were calculated by one of two methods.[A10,A13-A15] One of these, Fuller's method, has shown the best agreement with experimental values (generally < 10 %, although errors as large as > 60% have been reported).[A10] This method was used to estimate Fickian *D* values for all but two of the compounds for which published *D* values were lacking. The exceptions are the two phosphonates, DEMP and DIMP, for which the requisite atomic diffusion volumes have apparently not been reported. Therefore, an alternative method was used to calculate *D* values for these compounds.[A15]

In Fuller's method, the *D* value (torr cm^2/sec) of vapor A in gaseous matrix B (i.e., D_{AB}) is expressed as follows:[A11]

$$D_{AB} = \frac{1.0868T^{1.75}}{\sqrt{\frac{2m_Am_B}{m_A+m_B}}(\sqrt[3]{V_A}+\sqrt[3]{V_B})^2} \qquad \text{Eq. A.15}$$

where T is temperature (K), V_A and V_B are the so-called molecular diffusion volumes of A and B, and m_A and m_B are their respective molecular weights. B is air in this study. The molecular diffusion volume is the sum of the atomic diffusion volumes of the atoms comprising the molecule, weighted by an adjustment factor related to the structure of the molecule (e.g. branching, aromatic ring, or heterocyclic ring). Values of the atomic diffusion volumes and the structural weighting factors can

be found.[A10,A13,A14] Atmospheric pressure was assumed to be 760 torr when converting D_{AB} values to units of cm^2/sec.

For DEMP and DIMP, an alternative method was used, which expresses D_{AB} as follows:[A14]

$$D_{AB} = \frac{1}{3n\sigma_{AB}m_A}\sqrt{\frac{8kLT}{\pi}\left(\frac{m_A m_B}{m_A+m_B}\right)} \qquad \text{Eq. A.16}$$

where L is the Avogadro constant, n is the concentration of air molecules, σ_{AB} is the effective collision cross section, and k is Boltzman constant. To calculate D_{AB} values for DIMP and DEMP, we need to know the values of parameters on the right-hand size of the equation. All parameters in this equation are available from the literature except for σ_{AB}A[A16] To estimate σ_{AB} value, a molecular modelling package (VEGA ZZ)[A17] was used to obtain the molecular volumes of DEMP and DIMP. Assuming their molecules to be spherical, the molecular diameters can be estimated and a σ_{AB} value for DEMP and DIMP can be obtained.

As a check on the accuracy of eq. A.16, D_{AB} values of DMMP and m-xylene in air were calculated using this equation and compared to those reported in the literature or calculated by use of Fuller's method. Using eq. A.16, the D_{AB} values for DMMP and m-xylene are 0.015 cm^2/s and 0.017 cm^2/s, which are 30% and 25% of the reported D_{AB} values, respectively. Thus, it appears that eq. A.16 significantly underestimates D_{AB}. To account for this, we used 0.3 as an adjustment factor and applied it to to calculate the D_{AB} values of DEMP and DIMP, i.e., we divided the estimated D_{AB} values of DEMP and DIMP based on the eq. A.16 by the 0.3.

Note that if we use our experimental S_e values to back-calculate D_{AB} values for DEMP and DIMP, we obtain values of 0.029 and 0.023 cm^2/sec, respectively, which are probably as accurate and reliable as the those calculated using the approach described above. The lack of published D_{AB}

values for organophosphonates and of a reliable means of calculating them is an unfortunate situation that merits further study and resolution.

A9. Tests with vapor mixtures

Table A6 lists the concentrations, collected masses, exposure times, and observed S_e and DE values for o-xylene and DEMP for the tests involving exposures to mixtures of these two compounds with and without other compounds present. In the case of the 8-compound mixture, data for all 8 compounds are provided in Table A7.

Table A6. Results of exposures to o-xylene and DEMP individually and in various mixtures showing no effect on observed S_e values from the presence of other vapors.

Test Compound		Conc. (mg/m^3)	Collected mass (ng)	Exposure time (min)	S_e (mL/min)	DE (%)
Single cmpd	o-xylene	42	440	15	0.69	99
	DEMP	49	190	15	0.26	91
2-cmpd mixture	o-xylene	370	7,500	30	0.68	99
	DEMP	87	660	30	0.25	87
5-cmpd mixture	o-xylene	110	2,200	30	0.68	99
	DEMP	14	110	30	0.26	88
8-cmpd mixture	o-xylene	6.2	130	30	0.71	99
	DEMP	9.0	68	30	0.25	80

Table A7. Results of exposures to eight compounds individually and as a mixture showing no effect on observed S_e values from the presence of other vapors.

Test	Compound	Conc. (mg/m^3)	Collected mass (ng)	Exposure time (min)	S_e (mL/min)	DE (%)
Single cmpds	m-xylene	44	420	15	0.65	99
	cyclohexanol	42	390	15	0.62	98
	CEES	36	380	15	0.67	97
	cyclohexanone	23	240	15	0.64	96
	DMMP	24	160	15	0.44	98
	DIMP[a]	19	120	15	0.21	90
8-cmpd mixture	m-xylene	6.0	120	30	0.68	99
	cyclohexanol	1.9	37	30	0.62	98
	CEES	2.9	63	30	0.70	99
	cyclohexanone	12	250	30	0.65	99
	DMMP	6.0	76	30	0.42	84
	DIMP	6.6	45	30	0.22	82

[a] *DIMP data were obtained from the 5-compound mixture test.*

A10. References

A1. J. S. Mitchell, G. R. Lahiji and K. Najafi, Reliability and characterization of micro-packages in a wafer level Au-Si eutectice vacuum bonding process Proceedings of International Electronic Packaging Technical Conference and Exhibition (IPACK) '05, July 17-22, 2005, San Francisco, CA, pp. 2041-2045

A2. J. Bryant-Genevier and E. T. Zellers, Toward a microfabricated preconcentrator-focuser for a wearable micro-scale gas chromatograph, *J. Chromatogr. A*, 2015, **1422**, 299-309.

A3. G. O. Wood, Activated carbon adsorption capacities for vapors, *Carbon*, 1992, **30**, 593-599.

A4. F. Rouquerol, J. Rouquerol, K. S. W. Sing, P. Llewellyn and G. Maurin, *Adsorption by powders and porous solids: principles, methodology and applications*, Academic press, New York, 2013.

A5. Y.C. Chuang, P. C. Chiang and E. Chang, Modeling VOCs adsorption onto activated carbon, *Chemosphere*, 2003, **53**, 17-27.

A6. K.-J. Kim, C.-S. Kang, Y.-J. You, M.-C. Chung, M.-W. Woo, W.-J. Jeong, N.-C. Park and H.-G. Ahn, Adsorption–desorption characteristics of VOCs over impregnated activated carbons, *Catalysis Today*, 2006, **111**, 223-228.

A7. F. D. Yu, L. A. Luo and G. Grevillot, Adsorption isotherms of VOCs onto an activated carbon monolith: experimental measurement and correlation with different models, *Journal of Chemical & Engineering Data*, 2002, **47**, 467-473.

A8. F.-Y. Yi, X.-D. Lin, S.-X. Chen and X.-Q. Wei, Adsorption of VOC on modified activated carbon fiber, *Journal of Porous Materials*, 2009, **16**, 521-526.

A9. J. Wang, J. Ma and E. T. Zellers, Room-temperature-ionic-liquid coated graphitized carbons for selective preconcentration of polar vapors, *J. Chromatogr. A.* 1609, 2020, 460486

A10. M. Tang, M. Shiraiwa, U. Pöschl, R. Cox and M. Kalberer, Compilation and evaluation of gas phase diffusion coefficients of reactive trace gases in the atmosphere: Volume 2. Diffusivities of organic compounds, pressure-normalised mean free paths, and average Knudsen numbers for gas uptake calculations, *Atmospheric Chemistry and Physics*, 2015, **15**, 5585-5598.

A11. G. Lugg, Diffusion coefficients of some organic and other vapors in air, *Analytical Chemistry*, 1968, **40**, 1072-1077.

A12. J. T. Hunter and N. L. Abbott, Dynamics of the chemo-optical response of supported films of nematic liquid crystals, *Sensors and Actuators B: Chemical*, 2013, **183**, 71-80.

A13. E. N. Fuller, P. D. Schettler and J. C. Giddings, New method for prediction of binary gas-phase diffusion coefficients, *Industrial & Engineering Chemistry*, 1966, **58**, 18-27.

A14. E. N. Fuller, K. Ensley and J. C. Giddings, Diffusion of halogenated hydrocarbons in helium. The effect of structure on collision cross sections, *The Journal of Physical Chemistry*, 1969, **73**, 3679-3685.

A15. D. A. Trubitsyn and A. V. Vorontsov, Experimental study of dimethyl methylphosphonate decomposition over anatase TiO2, *The Journal of Physical Chemistry B*, 2005, **109**, 21884-21892.

A16. pubChem, https://pubchem.ncbi.nlm.nih.gov/ (accessed December 2019).

A17. VEGA ZZ, https://nova.disfarm.unimi.it/manual/pages/gl_index.htm (accessed December 2019).